Development of quantitative diffraction and imaging based techniques for scanning transmission electron microscopy

Benedikt Haas

Communauté
UNIVERSITÉ Grenoble Alpes

THÈSE

Pour obtenir le grade de

DOCTEUR DE LA COMMUNAUTÉ UNIVERSITÉ GRENOBLE ALPES

Spécialité : Physique de la Matière Condensée et du Rayonnement

Arrêté ministériel : 25 mai 2016

Présentée par

Benedikt HAAS

Thèse dirigée par **Jean luc ROUVIERE**, , CEA

préparée au sein du **Laboratoire Modélisation et Exploration des Matériaux**
dans **l'École Doctorale Physique**

Développement de techniques quantitatives en microscopie électronique à balayage en transmission

Development of Quantitative Diffraction and Imaging Based Techniques for Scanning Transmission Electron Microscopy

Thèse soutenue publiquement le **5 mai 2017**,
devant le jury composé de :

Monsieur QUENTIN RAMASSE
PROFESSEUR, UNIVERSITE DE LEEDS GRANDE BRETAGNE, Rapporteur
Monsieur ANDREAS ROSENAUER
PROFESSEUR, UNIVERSITE DE BREME - ALLEMAGNE, Rapporteur
Monsieur EDGAR RAUCH
DIRECTEUR DE RECHERCHE, CNRS DELEGATION ALPES, Président
Monsieur HOLGER KLEIN
MAITRE DE CONFERENCES, UNIVERSITE GRENOBLE ALPES, Examinateur

So blickt man klar, wie selten nur,
ins inn're Walten der Natur.

-Wilhelm Busch in *Maler Kleksel*

Contents

1 Introduction

With around 100 million photoreceptor cells the human eye is capable of capturing enormous amounts of information [1]. These cells are connected to approximately one million retinal ganglion cells that transfer the pre-processed data with a transfer rate of roughly 9 Mbit/s to the brain [2]. This illustrates an enormous amount of pre-filtering that includes the detection of gradients associated with boundaries and of changes in the visual field that hint at movements.

The visual system is not only able to handle this flood of information but also to further process it unconsciously. The grouping of visual elements into objects, the completion of partly hidden objects and the tracking of those are only a few of the automatisms of the visual system. Thus, vision is arguably the most powerful sense of humans.

Enhancing vision has therefore been one of the most important advancements of mankind. From telescopes to study the cosmos over glasses to correct for defective vision to microscopes that enabled the resolution of details and structures too fine to be perceived by the naked eye.

The extension of the resolving power of vision via optical instruments led to the discovery and understanding of a variety of fundamental phenomena, especially concerning biological systems. Establishing the organization of complex life forms in the form of building blocks called cells or the discovery of microscopic organisms was not only of fundamental interest but had imminent practical consequences for the understanding and thus prevention of or cure for diseases.

In the late 19th century the theory of light microscopes was sufficiently understood and craftsmanship advanced to reach the physically limited resolution, i.e. the Abbe limit, expressed in terms of numerical aperture NA and the wavelength λ as $d_{Abbe} = \frac{\lambda}{2\ NA}$ [3], rather than being limited by the quality of instruments.

In the late 1920s Ernst Ruska started working on an efficient cathode ray oscillograph under the supervision of Max Knoll for which he tried to understand the focusing of the writing spot [4]. He produced the first electron optical images and subsequently he

developed the (transmission) electron microscope (TEM) during his thesis [5]. The first two-stage imaging with a magnification of 14.4 was demonstrated in 1931. Although de Broglie attributed a wavelength of $\lambda = h/p$ to particles of momentum p (with h being the Planck constant) already in 1925 [6], Ruska and Knoll initially did not know about his work and "simply hoped for extremely low dimensions of the electrons" [7]. By the end of his thesis in 1933 Ruska had constructed a TEM with a magnification of 12'000 times, being more powerful than any light microscope.

The resolving power increased over the following decades until it reached around 2 $\mathring{\mathrm{A}}$ which was the limitation imposed by the lens aberrations. In fact, Otto Scherzer already published in 1936 his theorem that rotationally symmetric, static electron lenses that are free of space charge do always exhibit a positive, nonzero spherical aberration coefficient [8]. Interestingly, Denis Gabor developed holography (for which he later received the Nobel prize) initially for TEM to overcome the resolution limit imposed by the lens aberrations [9]. After efforts were made to realize a variety of designs of corrector optics starting in the 1960s, finally shortly before the turn of the millennium functional devices were presented and soon after the resolution limit was pushed to below 1 $\mathring{\mathrm{A}}$ [10].

TEM became an invaluable instrument for solid state physics and materials science even before reaching atomic resolution, due to the fact that it is also capable of producing diffractograms of µm-sized or today even nm-sized areas. Therefore, it was possible to access the local structure of materials and to study crystallinity, polymorphism and defects.

The power of micro-spot electron diffraction is underlined by the discovery of quasicrystals by Dan Shechtman in the early 1980s [11] which led to the redefinition of what a crystal is by the 'International Union of Crystallography' in 1992 and to the Nobel price in chemistry for Shechtman in 2011.

Direct observation of the structure of matter by atomic resolution TEM has proven to be an important asset for condensed matter physics and materials engineering. Even though other types of microscopes that can produce atomic resolution images have been developed starting from the 80s, like the scanning tunneling microscope or the atomic force microscope, the TEM is still the only microscope able to visualize the atomic structure of bulk-like samples. TEM is able to probe the structure of samples of thicknesses up to a few hundred nanometers, while all other types of microscopes do either not possess atomic resolution or their sensitivity is restricted to the very surface of samples which makes them important tools for surface characterization but renders them unable (or at least very problematic) to probe bulk properties or buried interfaces.

Therefore, the TEM is an invaluable tool for the development of novel materials; from catalyst nano-particles to light emitting diodes the advancement of materials is greatly enhanced by TEM characterization.

To aid the improvement and invention of materials, it is important to develop and enhance techniques and to extend the capabilities of the TEM by finding means of measuring new properties. Although more than 80 years have passed since the first TEM was built, powerful new developments are still being made. Recent developments include e.g. the introduction of fast and highly efficient pixelated electron detectors [12] or the extension of resolution beyond the diffraction limit by combining conventional TEM imaging with scanning probe illumination [13]. One example of a rather recent development that already had an impact on materials science is annular bright field (ABF) [14] in scanning TEM (STEM). It allows to better image light elements and has led to the direct visualization of hydrogen atoms in crystals [15].

This manuscript focuses on the development of diffraction and imaging based methods in STEM. The reason for the choice of STEM over conventional TEM is discussed below, while excluding spectroscopy is mostly for the sake of simplicity and coherence. Many different techniques are studied in this manuscript. The reason for this is that to be able to compare and judge competing methods correctly and without bias, it is necessary to understand and master them. And it is of course an advantage to have a series of methods at one's disposal when confronted with a materials science problem.
Three different domains of measurements are addressed, describing the state of the art and presenting the advancements developed during the thesis: the measurement of strain, the quantification of contrasts and the visualization and quantification of electric fields. In each of these three parts, different STEM based methods are described and compared.
Afterwards, the methods are applied to materials science problems to demonstrate their capabilities for the characterization of new materials.

2 | Scanning Transmission Electron Microscopy

STEM is a special mode of TEM in which the beam has a, more or less pronounced, convergence angle that leads to a focused probe, in contrast to the rather parallel plane wave illumination of conventional TEM (CTEM). More importantly, instead of acquiring data in parallel the probe is scanned and the synchronization of scanning and acquisition of a signal allows for the construction of an image in which the data collected at each step is attributed to the respective probe position.
The first scanning TEM was built by von Ardenne in 1938 [16], so only five years after the first TEM. It originally suffered from major drawbacks that were mostly stemming from the low beam current and the lack of digital means of recording. Several important improvements were made by Crewe: the introduction of field emission sources (and the first jump ratio images) in 1966 [17] and the first visualization of individual heavy atoms on a C support film in 1970 [18] for which he used an annular dark field detector. Another important developments on which this work is based was the development of high-angle annular dark field (HAADF) for Z contrast imaging by Howie and his students [19] and the application thereof for high-resolution imaging by Pennycook in 1990 [20]. Finally, the first sub-angstrom STEM images obtained with the help of a C_s corrector were demonstrated by Batson/Nellist in 2002/4 [10, 21].

This chapter begins with a description of the setup of STEM with a focus on the utilized microscopes and modes. A discussion of the different detectors used in conjunction with these modes can be found in the following section. Afterwards, a motivation of the exclusive use of STEM is given in the form of a discussion of STEM versus CTEM performances in different contexts. Afterwards, a description of the simulation of electron scattering for focused probes is given before closing the chapter by addressing resolution, contrast, noise and precision in STEM.

2.1 Experimental Setups

In this section the setup of experiments is explained, restricted to (or at least focused on) the essential parts that build the foundation of the methods used. The setup is explained specifically for the case of the microscopes used: FEI Titan^3 Ultimate and FEI Titan Themis. For more general information and details on the components and working principles of (S)TEM the reader is referred to TEM textbooks [22, 23].

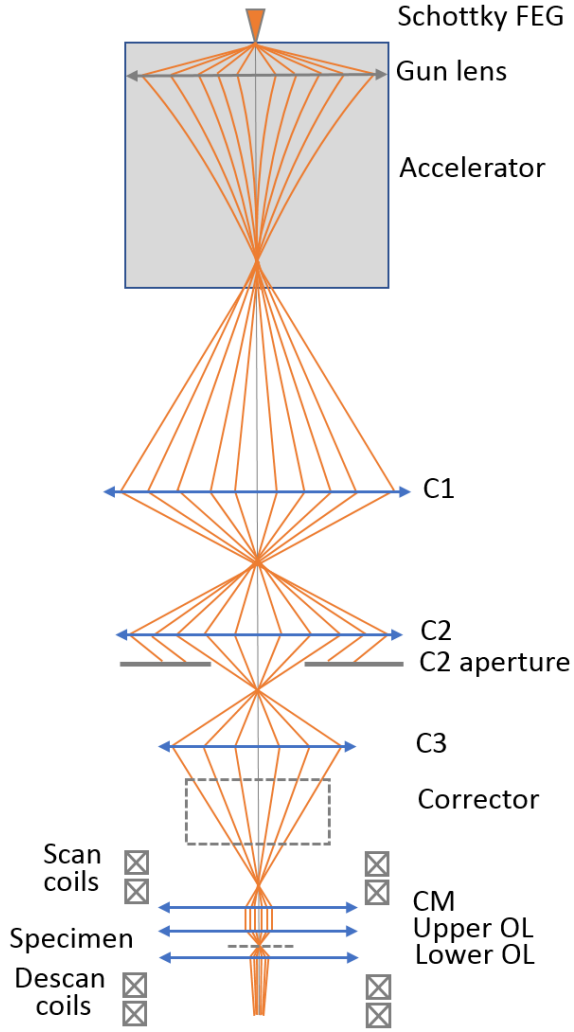

Figure 2.1: Basic setup of STEM for the microscopes used, depicting the principal components. Any deflection coils other than scan and descan are omitted for the sake of simplicity. OL denotes the objective lens and CM the condenser mini-lens.

Although not being dedicated STEMs, both microscopes used were only operated in STEM mode, which is what connects all techniques discussed in this manuscript. STEM means that a focused electron probe is scanned across a field of view and data is acquired

serially and synchronized with the displacement of the beam. For the experiments discussed in this manuscript the detector is either an annular STEM detector or a camera, meaning that for each probe position either a scalar intensity value or a matrix of values is acquired. Although in both cases the detector was placed in the diffraction plane, the integration of scattering intensity into a scalar value for each probe position in the case of an annular detector does not allow for any manipulation of diffraction data a posteriori and is therefore called imaging based because the only output is a real space map from the scanning process. For the case of an intensity matrix acquired for each probe position via a camera, information from the intensity distribution in reciprocal space can be obtained. Techniques relying thereon will be called diffraction based. For these methods it is of course also possible to analyze real space images produced by functions mapping the diffraction space matrix to a scalar value (e.g. a virtual aperture integrating intensities in a defined region). In the case of a segmented annular detector, which is used for DPC, four values are obtained for each probe position and the main information is provided by the difference signal, so DPC is called a diffraction based method. Yet, the sparseness of values greatly limits the ways to extract information and to produce real space images.

The main difference between the modes used is the convergence (semi) angle α and the detector used for acquisition. First, the different values and their influence on the obtainable resolution is discussed. A sketch of the general setup is depicted in Fig. 2.1.

Three-lens condenser systems, present in both TEMs used, allow for a continuous change of the convergence angle in contrast to being limited to the discrete physical sizes of the present condenser apertures. This feature is extensively used to optimize conditions for different experiments. Hexapole-based C_S-correctors from CEOS company are installed in both microscopes. The Titan^3 Ultimate also possesses a C_S-corrector for the objective lens, but as it serves no purpose for the techniques used it is omitted. The monochromator present in the Titan^3 Ultimate was not excited for any of the experiments and is also left out.

Parameter	Value
Beam energy E	200 keV
Energy spread ΔE	0.7 eV
Spherical aberration C_s	$<$ 1 µm
Chromatic aberration C_c	1.2 mm
Brightness β (200 keV)	2*10^{13} $\frac{A}{m^2 sr}$
Beam current I_p	100 pA

Table 2.1: Typical parameters for the microscopes and techniques used.

An important characteristic of the different techniques is the attainable probe size d that can be approximated as the combination of different factors

$$d = d_g^2 + d_d^2 + d_s^2 + d_c^2 \tag{2.1}$$

with the geometrical diameter of the probe d_g, the diffraction disc d_d, the influence of spherical aberration d_s and chromatic aberration d_c. Here, it is assumed that the individual contributions are independent of one another and of Gaussian shape. More detailed information can be found in [23]. The total probe size can be expressed as

$$d = \frac{4I_p}{\pi^2\beta}\frac{1}{\alpha^2} + (0.6\lambda)^2\frac{1}{\alpha^2} + \frac{1}{4}C_s^2\alpha^6 + \left(C_c\frac{\Delta E}{E}\right)^2\alpha^2 , \tag{2.2}$$

where E denotes the beam energy, ΔE the energy spread, α the convergence angle, C_s and C_c the spherical and chromatic aberration, respectively, I_p the beam current and β the gun brightness. This equation is of course incomplete, as it does not take into account any other aberrations than C_s and C_c for the sake of simplicity, but it helps to understand the limiting factors for different types of microscopes and settings. The influence of other aberrations is discussed below. The used microscopes have the same source (XFEG, a special kind of Schottky type field-assisted thermionic gun from FEI company with a high brightness) a probe corrector that pushes C_s to the measurement precision of around 1 µm and they are both mainly operated at 200 kV for the results shown in this manuscript. Typical values for both microscopes and the experiments performed are listed in Tab. 2.1. For the high brightness gun used, the first term is relatively small. The part accounting for C_s is negligible due to the corrector present in both microscopes. What is limiting for the resolution is determined by the convergence angle: for a small value of α the last two terms a negligible leading in our case to a limitation mainly by diffraction (originating from the condenser aperture) which can be calculated as

$$d_d = \frac{0.6\lambda}{\alpha} . \tag{2.3}$$

For the case of a high convergence angle the first two terms become negligible, leading in our case to a limitation by C_c, not mentioned (higher order) aberrations and electronic and mechanical stability of different parts of the microscope that are also not included in Eq. 2.1.

A comparison of the different convergence angle settings used with typical values for these angles and the resulting beam sizes is given in Tab. 2.2. The combination of α setting and detector leads to different operation modes: High-resolution HAADF and

Setting	High-resolution (HR)		Nano-beam (NB)		Low-mag. (LM)
Typical α	24 mrad		2 mrad		0.2 mrad
Typical beam size	0.1 nm		0.8 nm		8 nm
Detector used	Annular	Segmented	Camera	Segmented	Segmented
Mode	HR-HAADF HR-ABF	HR-DPC	NBED	NB-DPC	LM-DPC
Typical detector semi angles	60-180 mrad 12-24 mrad	12-60 mrad	0-40 mrad	1-5 mrad	0.1-0.5 mrad

Table 2.2: Listing of the modes used grouped into three different basic settings of convergence angle.

ABF, high-resolution/nano-beam/low-magnification differential phase contrast (DPC) and nano-beam electron diffraction (NBED). Typical detection angles for the different techniques are sketched in Fig. 2.2. These are of course only the modes and techniques explored and developed in this manuscript and many others are possible. An example of another mode of operation is electron pico-diffraction which combines a high-resolution setting with a pixelated detector and can map electric fields at atomic resolution as demonstrated by Müller et al. [24].

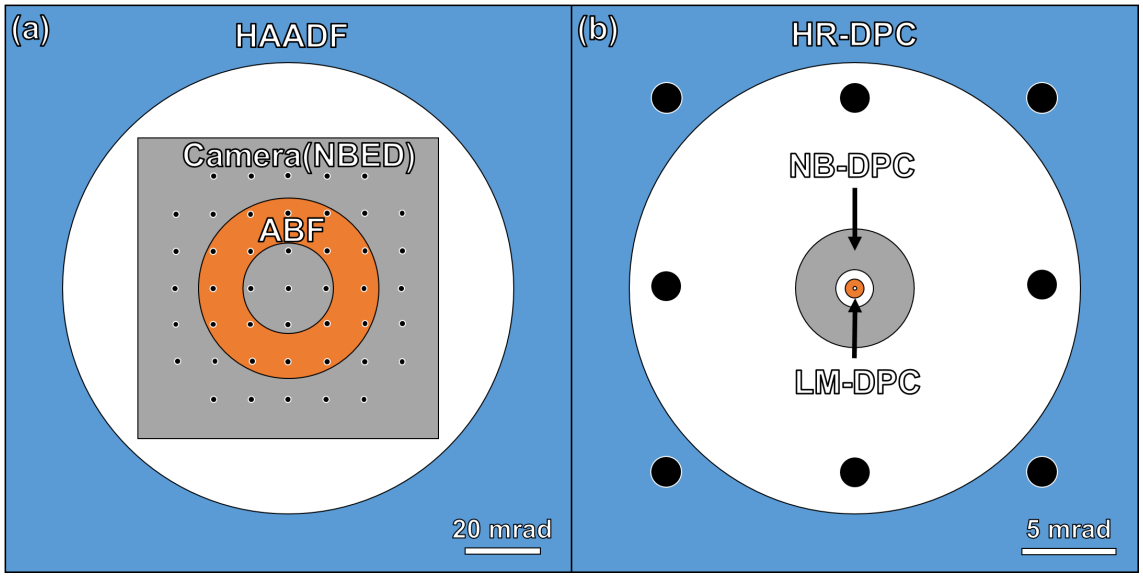

Figure 2.2: Typical detection angles of the different detectors. In (a) the HAADF and ABF detector ranges are sketched together with the camera size for a typical NBED experiment. Image (b) shows the detector angles of HR-/NB-/LM-DPC. The black spots correspond to a diffraction pattern of Si [001] at 300 kV.

For the chosen operation modes either one or two different techniques are used (cf. Tab. 2.3). The techniques consist of a special acquisition mode and a data treatment to measure certain properties. For example strain or chemical information can be obtained with atomic resolution from data acquired in high-resolution HAADF (HR-HAADF) op-

eration mode by atom position determination or intensity quantification. However, they necessitate the control or optimization of different experimental parameters. While the quantification of intensities requires a knowledge of the vacuum offset value of intensity, the determination of atom positions does not necessitate this information but instead it needs to mitigate artifacts from the scan generator. Detailed information for each technique is given in the respective sections in Chap. 3.

Mode	**HR-HAADF**		**HR-ABF**	**HR-/NB-/LM-DPC**	**NBED**
Technique	Int. quant.	Atom pos. det. SMF	Int. quant.	DPC	NPED
Determines	Composition	Strain	Composition	E-field	Strain E-field

Table 2.3: Overview of the used techniques attributed to the different modes of operation and the parameters that are measured. SMF stands for scanning moiré fringes. Intensity quantification is abbreviated as 'int. quant.' and atom position determination as 'atom pos. det.'.

The formation of diffraction patterns during scanning is schematically shown in Fig. 2.3. If the pivot point (PP) of the scan coils lies in the front focal plane (FFP) of the objective lens, a stationary diffraction pattern of discs whose diameter corresponds to the convergence angle is formed during scanning. The descan coils that are drawn in Fig. 2.1 are not necessary in this case. They are only needed for a stationary image plane, like in the case of confocal STEM. As only experiments with a detector in the diffraction plane are demonstrated, the sketch in Fig. 2.3 is sufficient for the understanding. For the setups used here, the lenses following the objective lens only have the task to magnify the diffraction pattern (and to compensate for rotations) and are therefore omitted. The only setup utilized here in which the descan coils play an important role is for nano-beam precession electron diffraction (NPED). Here, the beam is not only scanned but additionally precessed around the optical axis as proposed by Vincent & Midgley [25]. To compensate the additional dynamic tilt, the descan coils are needed to keep the diffraction pattern stationary.

To address the issue of an aberrated probe, especially for the case of a C_s corrected probe forming lens, in more detail, we neglect the influence of the finite source size. The intensity distribution of the probe I_p in the plane perpendicular to the optic axis before interacting with the sample can, according to Kirkland [26], then be expressed as:

$$I_p(\mathbf{R}) = |\Psi_p(\mathbf{R})|^2 = A_p \left| \int_0^{k_{max}} exp\left[-\frac{2\pi i}{\lambda}\chi(\mathbf{k}) - i\mathbf{k}\cdot\mathbf{R} \right] d^2\mathbf{k} \right|^2 . \tag{2.4}$$

This function is also called point spread function. Here, k_{max} denotes the maximum spatial frequency and corresponds to the radius of the probe forming aperture (assumed

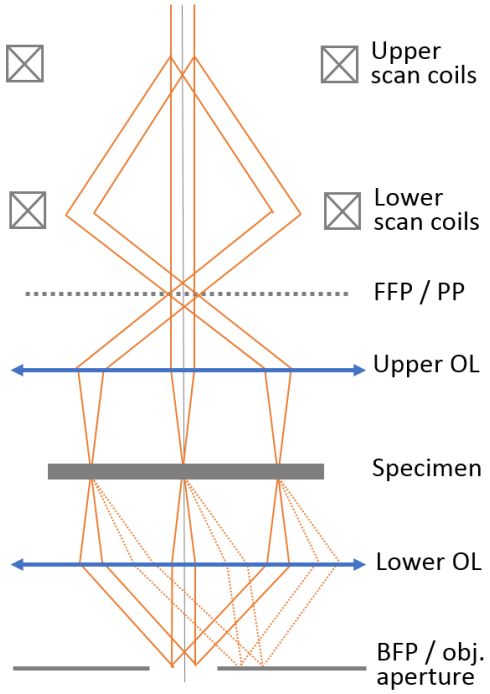

Figure 2.3: Schematic drawing of how different beam positions during the scanning lead to stationary discs of direct and diffracted beams in the back focal (BFP) plane of the objective twin-lens. Descan coils are only necessary for a stationary image plane during scanning and for the case of precession diffraction.

to be circular) and $\mathbf{R}$ is a two-dimensional position vector within the plane perpendicular to the beam direction. The aberration function $\chi(\mathbf{k})$ describes the deviation of the aberrated wavefront from the ideal wavefront by means of phase shifts that depend on the spatial frequencies $\mathbf{k}$ in the plane perpendicular to the optic axis. This function, that describes a two-dimensional surface, is usually expressed in terms of two angles instead: the angle to the optic axis θ and the angle around the optic axis φ. A useful expansion of the aberration function [27] is:

$$\begin{aligned}\chi(\theta,\varphi) = & \, constant + \theta[C_{0,1,a}cos(\varphi) + C_{0,1,b}sin(\varphi)] \\ & + \frac{\theta^2}{2}[C_{1,0} + C_{1,2,a}cos(2\varphi) + C_{1,2,b}sin(2\varphi)] \\ & + \frac{\theta^3}{3}[C_{2,3,a}cos(3\varphi) + C_{2,3,b}sin(3\varphi) + C_{2,1,a}cos(\varphi) + C_{2,1,b}sin(\varphi)] \\ & + \frac{\theta^4}{4}[C_{3,0} + C_{3,4,a}cos(4\varphi) + C_{3,4,b}sin(4\varphi) + C_{3,2,a}cos(2\varphi) + C_{3,2,b}sin(2\varphi)] \\ & + ... \end{aligned} \tag{2.5}$$

The first constant term represents a phase offset. The resulting aberration coefficients $C_{m,n} = C_{m,n,a}cos(n\varphi) + C_{m,n,b}csin(n\varphi)$ for the aberrations that were minimized by tuning the corrector are listed in Tab. 2.4. It should be noted that the correction software optimizes the aberrations to counteract the not correctable aberrations (e.g. C_s is set to a negative value to counteract the native, positive C_5 value of around 5 mm). The values that are given are the deviations (measurement confidence intervals) from the ideal value of the aberrations.

Coefficient	Name	CEOS software	Typical value after tuning
$C_{0,1}$	Image shift	-	-
$C_{1,0}$	Defocus	C_1	1 nm
$C_{1,2}$	Twofold astigmatism	A_1	1 nm
$C_{2,1}$	(Axial) coma	$\frac{1}{3}$ B_2	50 nm
$C_{2,3}$	Threefold astigmatism	A_2	50 nm
$C_{3,0}$	Spherical aberration	C_3	500 nm
$C_{3,2}$	Star aberration	$\frac{1}{4}$ S_3	800 nm
$C_{3,4}$	Fourfold astigmatism	A_3	800 nm
...	...	...	...
$C_{5,0}$	Fifth order spherical aberr.	C_5	5 mm (native)

Table 2.4: List of aberration coefficients, their denotation in the CEOS corrector software and typical values after tuning of the corrector (determined by the measurement precision).

The influence of the finite source size can be added by convolving the beam profile due to aperture size and aberrations from Eq. 2.4 with the demagnified source (e.g. d_g from Eq. 2.1 and Eq. 2.2). In a simple approximation the energy spread of the source as well as fluctuations of the lens current and the accelerating voltage can be accounted for by integrating the transfer function over a range of defoci with a Gaussian distribution. The transfer function of STEM is the inverse Fourier transform of the point spread function (PSF) from Eq. 2.4.
For more information on correctors and aberrations the reader is referred to the literature [26, 27, 28, 29].

2.2 Detectors

As mentioned in the section before, different detectors have been used: annular, segmented (annular) and cameras. Here, the basic setup of the different detectors and their characteristics are discussed in brief, with a stress on the basics of the annular scintillator based detector because it builds the foundation of section 3.2.

The first type, the annular detector used in the experiments, consists of a ring of scintillator material attached to a quartz crystal light pipe. A drawing is depicted in Fig. 2.4

(a). Photons produced from the impinging electrons at the scintillator are guided to a photo-multiplier tube (PMT) via reflection at the borders of the quartz crystal. There, the photons are first converted back into electrons by means of a photo-cathode before being multiplied by a cascade of dynodes and finally collected at the anode (sketched in (b)). The total gain can be controlled by applying different voltages to the dynodes. The applied voltage, evenly split between dynodes by means of resistors, controls the amplification factor of the signal which corresponds to the contrast in the image. The output of the PMT is connected to an amplifier. Here, the brightness can be adjusted by applying a voltage that shifts the dark level. Subsequently, the signal is digitized with a given bit depth (typically 16 or 32 bit).

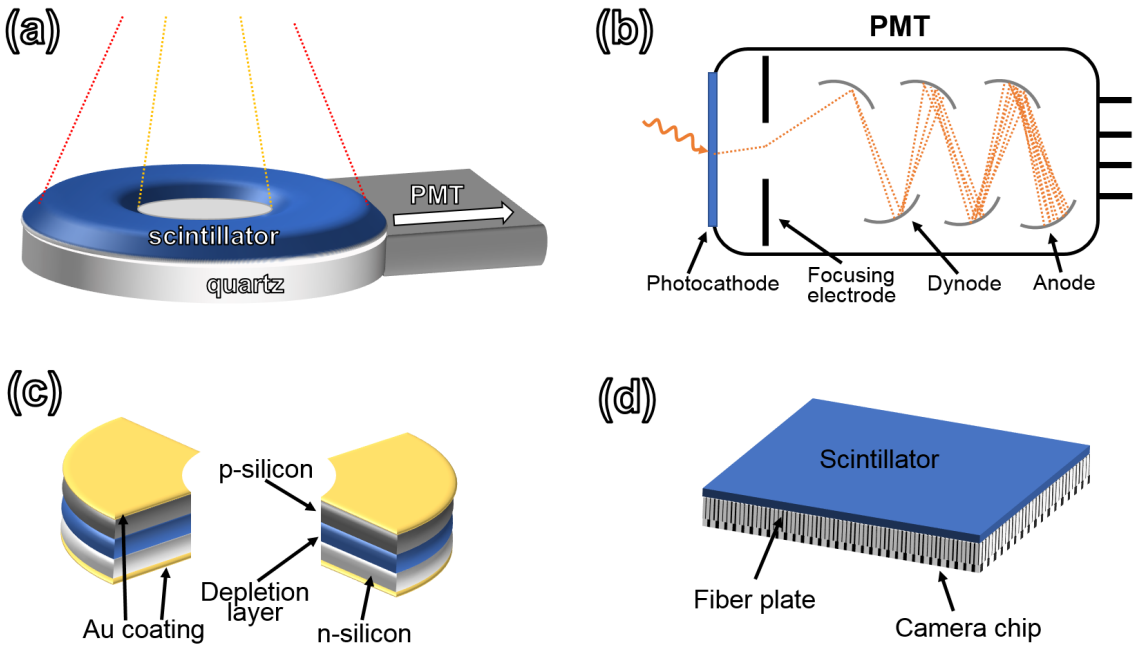

Figure 2.4: Schematic drawings of the utilized detectors: (a) annular scintillator based detector with a sketch of the collected scattering angles, (b) photo multiplier tube used in conjunction with this detector, (c) segmented annular semiconductor detector (showing two of the four segments) and (d) camera coupled to a scintillator by means of a fiber plate.

An important parameter to judge the quality of a detector is the detective quantum efficiency (DQE), defined in terms of the incoming and outputted signal-to-noise ratio (SNR) as

$$DQE = \frac{SNR_{out}^2}{SNR_{in}^2} \,. \tag{2.6}$$

For an electron beam impinging on the detector, the number of electrons over time follows a Poisson distribution with the variance equaling the mean number of electrons

in a given time interval. If the mean number is sufficiently high, the distribution can be well approximated by a normal distribution. A few hundred electrons per interval lead already to a very good approximation. From the definition of the ampere we can estimate typical average numbers of electrons as

$$1\,C = 1\,A \cdot s \approx 6.242 \cdot 10^{18}\,e \implies 1\,pA \cdot 1\,\mu s \approx 6.242\,e\ . \tag{2.7}$$

If an electron beam of 100 pA is directly guided onto the detector (no specimen in between), 624.2 electrons impinge on average during a dwell time of 1 µs. The SNR can be written in terms of the standard deviation σ of the mean number of electrons $\overline{N}$ as

$$SNR = \frac{\overline{N}}{\sqrt{\overline{N}}} = \sqrt{\overline{N}}\ . \tag{2.8}$$

The SNR would in our case be 25.0. If this is the incoming SNR, the outgoing SNR would be diminished by the square root of the DQE:

$$SNR_{out} = SNR_{in}\,\sqrt{DQE}\ . \tag{2.9}$$

Browne et al. have analyzed in detail the multistage process of a scintillator based STEM detector, including a Poisson distributed incoming electron beam, the conversion of the electrons into photons, the loss of photons in between the scintillator and the photo-cathode of the PMT and the conversion of photons back to electrons [30]. Typically, many photons are created by an impinging electron at the scintillator while the generation of electrons at the photo-cathode of the PMT is smaller than unity. Together with the dynodes of the PMT providing virtually noise-free amplification, the outgoing SNR reduces in good approximation to

$$SNR_{out} = \sqrt{\frac{\overline{n}\,\overline{N}}{\overline{n}+1}}\ . \tag{2.10}$$

where $\overline{n}$ denotes the average number of electrons created by the PMT photo-cathode per incoming electron. This expression is derived in detail in App. A. The factor $\overline{n}$ comprises the conversion rate of the scintillator (for typical beam energy and materials several hundred photons are created per electron) diminished by the ratio of photons that make it to the photo-cathode and the conversion factor of photons into electrons (typically around 0.2) [30]. From the definition of the DQE in Eq. 2.6 we can now express it just in terms of $\overline{n}$

$$DQE = \frac{\overline{n}}{\overline{n}+1} \tag{2.11}$$

Any wavelength-dependence of the conversion is not included in this approximation. Annular scintillator-based detectors have a DQE of around 0.9 [22] meaning that the incoming SNR is diminished by only around 5 %. Therefore, HAADF images are predominately limited by shot noise from the Poisson distribution of incoming electrons over time. A disadvantage of the scintillator-based annular detector is the spatial inhomogeneity of the detector response, as depicted in Fig. 2.5 (a) and discussed in more detail in Chap. 3. These fundamentals of the scintillator-based STEM detector are used to correctly describe noise in HAADF images in Sec. 3.1.1 and to determine beam current and DQE in Sec. 3.2.1.

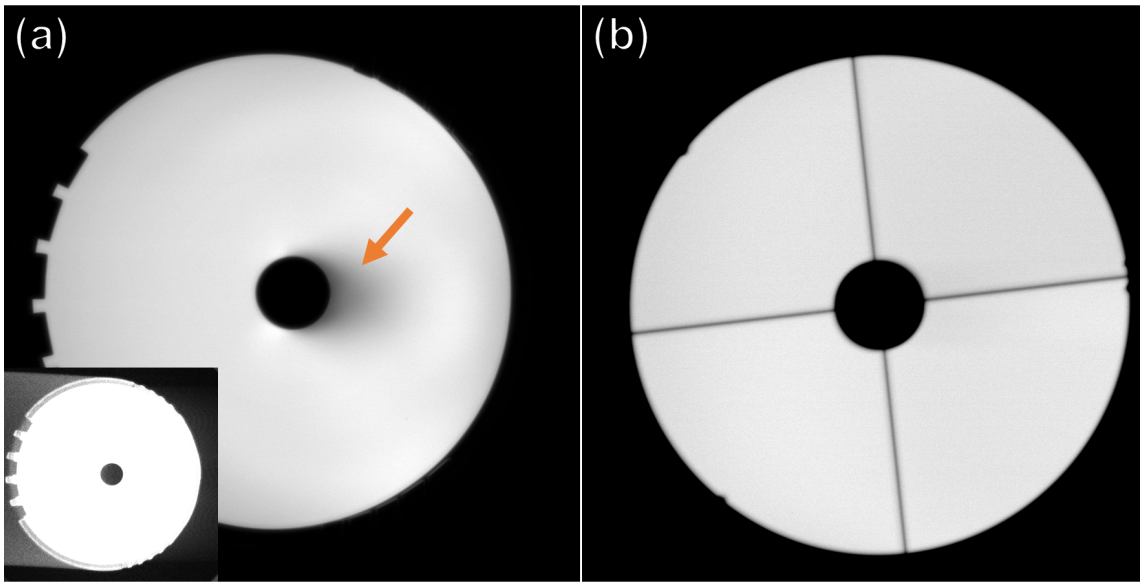

Figure 2.5: Detector scans of (a) annular scintillator detector and (b) segmented semiconductor detectors. The arrow in (a) marks a region of low detector response and the inset (same image with adjusted intensity scale to bring out low values) shows that this region is opposite the light pipe towards the PMT.

The second kind of detector used here is the (fourfold-)segmented annular type. This one is not based on a scintillator and PMT but is instead a semiconductor type as sketched in Fig. 2.4. The main part of a semiconductor detectors is a p-n junction that separates electron-hole pairs that are created by the impinging beam, leading to a current that can be picked up at the contacts. The reason for the use of semiconductor types for segmented detectors is twofold: first, semiconductor detectors do not use a PMT and therefore the integration of several individual segments into the column is much easier.

Secondly, the response of semiconductor detectors is much more homogeneous across their detecting area which is an important characteristic when relying on difference signals between segments. A scan of a segmented semiconductor detector is shown in Fig. 2.5 (b). Drawbacks of the semiconductor detector are its response time that necessitates rather long dwell times to avoid a smearing of signal between pixels, and the large dark current. The segmented semiconductor detector is used with dwell times of typically 64 µs while the annular scintillator detectors are mostly used with dwell times in between 0.2 to 4 µs. The large dark current means that the DQE of the detector is lower, especially for small signals.

The camera detectors that are used in this manuscript consist of a scintillator slab converting the incident beam electrons into photons and a fiber plate that guides the light to the camera itself (cf. Fig. 2.4 (d)). Several different cameras are available at the microscopes that belong either to the charge-coupled device (CCD) or complementary metal-oxide semiconductor (CMOS) family. For the CCD the charge carriers generated in the silicon of the camera from the impinging photons are stored in potential wells and the readout works by sequentially transferring the stored carriers from one pixel to the next until they individually reach the readout line. In the case of a CMOS device individual readout electronics is available for each pixel. The way they work leads to small differences between the two types that are not discussed here, but the general characteristics are dominated by the fiber-coupled scintillator system. Due to electron diffusion in the scintillator and photon scattering afterwards, the signal is not located at a sharp position like the incident electron but spread over several pixels. This PSF in real space means that the DQE is a function of the image frequencies that decreases with increasing frequency. However, even for zero frequency the DQE of a decent scintillator camera is only about 0.4 [31] and declines for higher spatial frequencies. Today there are also pixelated detectors without scintillator that directly detect incoming electrons (direct electron detectors), although none are presently available at CEA-Grenoble. For these detectors, the DQE at zero frequency can be above 0.7 [32]. However, they are somewhat delicate and can normally not cope well with the high dynamic ranges of diffraction patterns, for which cameras are exclusively used in this manuscript. The diffraction related methods for which a camera detector is used are based on the position of features and not on their absolute contrast value. Therefore, the PSF of the camera is not taken into account because it only reduces the precision of the methods without causing systematic errors.

2.3 STEM vs. CTEM

In this section the focus of this manuscript on scanning TEM is motivated in the form of a comparison of STEM with CTEM. Although still being highly used and broadly researched and developed, the following discussion is meant to explain the, in the eyes of the author, mostly superior characteristics of STEM. The advantages and drawbacks of both modes are discussed in different contexts and the focus on STEM shall thereby be explained.

In CTEM the image is acquired in parallel in contrast to STEM where the beam is scanned and the image is therefore serially generated. In terms of sampling, the scanning process of STEM is equivalent to the pixelation of the detector in CTEM. While in CTEM the detector has a finite amount (typically 2048^2) of pixels that are arranged in a regular grid, in STEM the amount, spacing and angle of scanning steps can (at least from a hardware point of view) be arbitrarily chosen. One consequence is that STEM typically allows for more measurement points per image (for the microscopes used 8096^2) and for a free choice of aspect ratio. Another possibility is to chose scanning step sizes and angles in a way to create customizable interference patterns between the scan grid and a crystal lattice (scanning moiré fringes, SMF) that amplify distortions of the structure. The free choice of scanning patterns facilitates an adaptation to different crystals and orientations. This is discussed and investigated in more detail in Sec. 3.1.2.

CTEM is based on plane wave illumination to facilitate parallel acquisition while in STEM a convergent beam probes locally during the scanning process. For CTEM the image is formed by the objective lens, collecting the plane electron wave after passing through the sample region. High-resolution imaging is facilitated in CTEM by the contrast transfer function (CTF) of the objective lens that adds a phase shift depending on the scattering angle to the electron wave, thus leading to an intensity modulation in the image (phase contrast). This contrast mechanism necessitates (partial) coherence to work and the reliance on interference renders it rich in information but also prone to perturbations. STEM readily offers (partially) coherent and incoherent high-resolution imaging, e.g. in the form of BF and HAADF. Especially the incoherent high-resolution imaging proves useful for strain measurements at atomic resolution, as is discussed in section 3.1.1. There, it is also discussed how to reduce image distortions due to serial acquisition that generally are a disadvantage of STEM.

Inelastic scattering is unavoidable for any interaction of the electron wave with matter, leading to distortions of images in CTEM due to chromatic aberration of the imaging

lens. In the case of STEM, the influence of chromatic aberration on the resolution is only the widening of the probe based on the energy spread before interacting with the sample. The image is formed by acquiring diffraction space information and a distortion there has normally no influence on the resolution. In addition, the more energy lost, the more forward centered the scattering generally is, making it easy to separate it in STEM. The different influence of C_c on the resolution for STEM and CTEM becomes even more pronounced for low-voltage electron microscopy. While STEM suffers mainly from the reduced wavelength, for low-voltage CTEM the relative influence of energy losses in the sample becomes more problematic and a chromatic aberration corrector is imperative to achieve decent high-resolution [33]. To improve the already better performance of STEM at low beam energy, the source can be monochromated to obtain a sharper probe, which is significantly easier than correcting for C_c.

To reduce the influence of charging and beam damage (at least radiolysis based degradation) it is generally an advantage to illuminate locally instead of larger areas, because the locally charged, heated or excited material can dissipate accumulated carriers or energy more easily to adjacent regions. For knock-on damage-based degradation the reduction of the beam energy to counteract or avoid the process is much less problematic for STEM than for CTEM, as discussed above.

Another advantage of STEM in terms of dose reduction is the implementation of compressed sensing [34]. In compressed sensing due to assumptions about the observed object a reduced sampling still results in a full retrieval of information. The scanning process allows for an easy and adaptable implementation of controlled undersampling (like in the case of SMF).

The biggest advantage of CTEM is probably the speed of imaging that stems from the parallel acquisition. This advantage mainly plays a role in in-situ experiments. Here, CTEM-based techniques are currently dominating the field [35].

The difference in data acquisition (parallel versus serial) leads to a wider range of detectors available to STEM. Using segmented detectors or cameras in STEM leads to four dimensional datasets that allow for powerful techniques, a few of which are described in Chap. 3. Integrating detectors with no PSF and a very high DQE are ideal to quantify signals, especially when detecting incoherent (quasi-) elastic scattering. Here, the level of understanding of the scattering process and the quality of the detectors allow for a precise quantification of the signal on an absolute scale [36], even at high-resolution [37]. In CTEM, this is virtually impossible. The modulation transfer function of the camera was identified as a mayor contribution [38] to the so called Stobbs factor, which describes the difference between simulated and measured (phase) contrast in high-resolution images. However, the HR-CTEM contrast is sensitive to a plethora of perturbations and to the

author's knowledge no materials science problem has been solved using phase contrast on an absolute scale. The quantification of HAADF contrast is discussed in Sec. 3.2.

2.4 Simulating Electron Scattering of Focused Probes

The goal of this section is to describe how to simulate (dynamical) electron scattering of focused probes by means of different methods. For this, first the Bloch waves method is briefly described and strengths and weaknesses are pointed out before explaining the multislice approach. Afterwards, some remarks on thermal diffuse scattering and how to include it are made before discussing the parameters used in multislice simulations. Finally, a brief description of the channeling theory is given to gain a more intuitive understanding of electron scattering processes. For an introduction to electron scattering theory the reader is referred to the literature [22, 39, 23].

Bloch Waves

The electron wavefunction in a crystal can be expressed as a linear combination of a basis set that satisfies the Schrödinger equation in this periodic potential, i.e. Bloch waves:

$$\Psi(\mathbf{r}) = \sum_j \alpha_j b_j(\mathbf{k}_j, \mathbf{r}) \ . \tag{2.12}$$

Here, $\mathbf{r}$ denotes a real space vector, $b(\mathbf{k}_j, \mathbf{r})$ the individual Bloch waves with the scattering wave vectors $\mathbf{k}_j$ and the coefficients α_j. The Bloch waves have the form:

$$b_i(\mathbf{k}_j, \mathbf{r}) = \sum_{\mathbf{G}} C_{\mathbf{G},j} exp[i(\mathbf{k}_j + \mathbf{G}) \cdot \mathbf{r}] \ . \tag{2.13}$$

Here, the $\mathbf{G}$ are the reciprocal lattice vectors and the $C_{\mathbf{G},j}$ the coefficients of Bloch wave j. Due to the assumption that the specimen is a crystal, any deviations from a periodic structure can pose a problem.
The focused probe at the entrance surface of the sample converts into Bloch waves inside the crystal. Any wave function describing the probe and its first derivative must be continuous at this interface and this condition determines the Bloch waves present in the sample.
The Bloch waves inside the specimen must satisfy the Schrödinger equation

$$\left[-\frac{\hbar^2}{2m}\nabla^2 - eV(\mathbf{r}) \right] b_j(\mathbf{k}_j, \mathbf{r}) = E\, b_j(\mathbf{k}_j, \mathbf{r}) \ , \tag{2.14}$$

with the reduced Planck constant $\hbar = \frac{h}{2\pi}$. Here, the energy is approximated to be constant $E = \frac{h^2}{2m\lambda^2}$ because elastic scattering is assumed. The periodic potential of the specimen is

$$V(\mathbf{r}) = \sum_{\mathbf{G}} \frac{2\pi e a_0}{\Omega} \sum_j f_j(G)\, exp(-i\mathbf{G}\cdot\mathbf{r_j})\, exp(i\mathbf{G}\cdot\mathbf{r}) \tag{2.15}$$

with the scattering factors f_j of the jth atom in the unit cell in the first Born approximation, the Bohr radius a_0 and the volume of the unit cell Ω. In practice, the $V_{\mathbf{G}}$ are calculated up to a maximum G.

To obtain a solvable equation a few approximations in the framework of the so called high-energy approximation [40] are made, using the fact that the wave vector of the incoming electrons is much larger than reciprocal lattice vectors and that it barely changes in magnitude when interacting (elastic interaction). All backscattering is also omitted. With these approximations an equation to determine the eigenvalues and eigenvectors can be obtained

$$2k_0 s_{\mathbf{G}} C_{\mathbf{G},j} + \sum_{\mathbf{H}\neq\mathbf{G}} \frac{2me}{h^2} V_{\mathbf{G}-\mathbf{H}} C_{\mathbf{H},j} = 2\gamma_j k_{0,z} C_{\mathbf{G},j} \ , \tag{2.16}$$

where $s_{\mathbf{G}}$ denotes the excitation error, $k_{0,z}$ is the incoming wave vector component in z direction and γ_j is an additional wave vector component (in beam direction) for each Bloch wave that describes the acceleration from the experienced crystal potential.

When repeated for each $\mathbf{G}$, a matrix can be obtained that allows to calculate the eigenvalues $2\gamma_j k_{0,z}$ and eigenvectors (sets of $C_{\mathbf{G},j}$). For M Bloch waves there will be M $\mathbf{G}$ vectors and M eigenvalues and eigenvectors and consequently M^2 coefficients $C_{\mathbf{G},j}$.

The CPU time for solving this problem scales with $\mathcal{O}(M^3)$, which is generally not favorable. Yet, for small crystals and/or high symmetry it can be fast. It is important to note that for the case of CTEM where the incoming beam is typically just one plane wave only a few Bloch waves are necessary to describe the problem sufficiently. For STEM however, due to the convergent probe, many more Bloch waves are being excited and need to be considered for a correct description. Especially for a very small probe, the Bloch waves that are excited are very different for different positions of the beam within the unit cell. The advantage and limitation of the Bloch wave method is that it relies on the symmetry of the specimen structure.

The next step after the eigenvalues and eigenvectors have been determined is to find

the weighting coefficients α_j of the Bloch waves so that the wave function anywhere in the crystal can be calculated. To facilitate this, the wave function of the beam needs to be matched to the excited Bloch waves considering the boundary conditions (the wave function and its first derivative must be continuous). There are different ways to do that, either by describing the probe as a superposition of plane waves [41, 42, 43] or by means of an overlap integral [44]. However, it has been shown that the outcome of the two approaches is equivalent [45]. After finding the coefficients α_j describing the excitation of the individual Bloch waves, the wave function at the exit surface of the crystal can be calculated. Bloch wave calculations are used in the framework of this thesis via the JEMS software package from Stadelmann [46] to simulate e.g. position averaged convergent beam electron diffraction (PACBED) patterns [47, 48].

The Multislice Method

Another way to describe the propagation of the wave function through the specimen is the multislice concept. It was originally proposed by Cowley and Moodie [49] and benefited greatly from the utilization of the fast Fourier transform by Ishizuka and Uyeda [50].

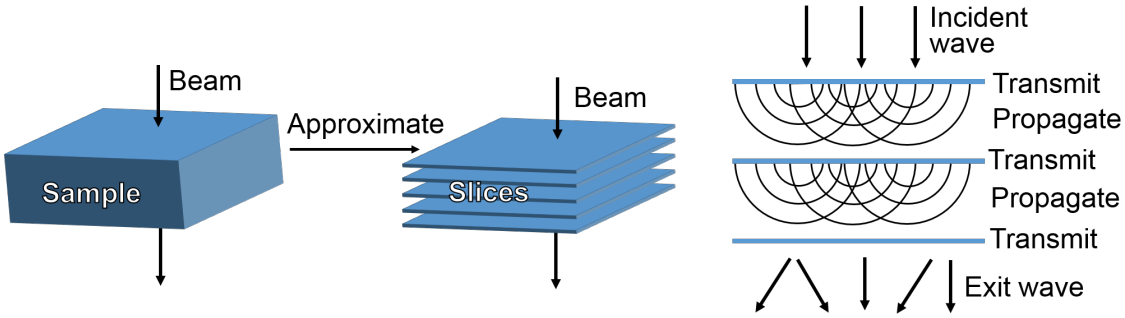

Figure 2.6: Schematic drawing of the multislice method; the sample is approximated as a series of slices that contain the projected potential of their corresponding sub-volume. The incident wave is transmitted through a slice, then propagated through vacuum to the next slice and so on.

The idea is to virtually split the specimen into sub-volumes (typically perpendicular to the beam direction) and project the potential contained in one sub-volume into one plane. These slices can account for different thicknesses, but often they are of equal volume. Propagation of the wave function through a specimen is approximated by transmitting it through the first slice, propagate the outcome through vacuum and repeat for the next slice (cf. Fig. 2.6). Thus, the wave function at the $j+1$th slice is:

$$\Psi(\mathbf{R}, z_{j+1}, \mathbf{R}_0) = [\Psi(\mathbf{R}, z_j, \mathbf{R}_0)\, t(\mathbf{R}, z_j)] \otimes P(\mathbf{R}, \Delta z_j)\ . \tag{2.17}$$

Here, $\mathbf{R}$ denotes a vector in the plane of the slice, $\mathbf{R}_0$ is the position of the probe at the entrance surface of the specimen and z is the coordinate perpendicular to $\mathbf{R}$. For the sake of simplicity the beam direction is considered to be perpendicular to the slices, which is generally not necessary but often the case. The transmission function is:

$$t(\mathbf{R}, z_j) = exp\left\{ \frac{2\pi i m}{h^2 k_0} [V(\mathbf{R}, \mathbf{z_j}) + iV'(\mathbf{R}, z_j)] \right\} . \tag{2.18}$$

The potential is split into a real part and and imaginary part. Role and magnitude thereof are discussed below. The propagator function is defined as:

$$P(\mathbf{R}, \Delta z_j) = \frac{1}{i\lambda \Delta z_j} exp\left(\frac{i\pi R^2}{\lambda \Delta z_j} \right) . \tag{2.19}$$

The multislice method offers a lot of flexibility, allowing for drastic changes in structure and/or composition in between slices. Computationally it is advantageous to make use of the (fast) Fourier transform ((F)FT) by means of the Fourier convolution theorem and calculate:

$$\Psi(\mathbf{R}, z_{j+1}, \mathbf{R}_0) = FT^{-1}\{FT[\Psi(\mathbf{R}, z_j, \mathbf{R}_0)\, t(\mathbf{R}, z_j)]\; FT[P(\mathbf{R}, \Delta z_j)]\} . \tag{2.20}$$

It is possible to account for small specimen tilts by changing the propagator function so that the propagation direction is inclined, but this only holds for tilts of a few mrad [26]. The computation time of the FFT for a problem of size M scales with $\mathcal{O}(Mlog_2 M)$ (the scaling for the normal FT is $\mathcal{O}(M^2)$) making multislice calculations very useful, especially for larger M and offering a better way to handle non-periodicities in the sample. It should be noted that to reproduce high-resolution STEM images the transmission and propagation process needs to be done for every position of the probe. However, the projected potentials (phase-gratings) and the propagator function can be kept and reused.

Thermal Diffuse Scattering

To simulate the scattering correctly, especially for higher angles, it is important to take into account the thermal diffuse scattering from phonons (the so-called TDS). The effect of the TDS is to redistribute scattering intensity away from the Bragg diffraction into a diffuse background. This scattering is strictly speaking inelastic because phonons are either being created or destroyed. As their energy is typically only tens of meV, the scattering is often said to be quasi-elastic. It can be included by the use of Debye-Waller factors that describe the temperature-dependent movement of the atoms around their equilibrium value.

One way to do so is the absorptive potentials method. It introduces a so-called absorption potential that accounts for inelastic scattering. Only a small fraction of intensity is truly absorbed (the name is somewhat misleading), but the method works by excluding inelastically scattered electrons from further elastic scattering. This means that e.g. Kikuchi lines cannot be reproduced by the method. For the inelastically scattered wave (from the portion of the potential that represents the absorptive potential) it is only noted if it is scattered towards the detector (then it counts towards the measured intensity) or if not (then it is simply removed). The absorptive potential method is e.g. implemented in Kirkland's TEMSIM code [26] and it is used for certain multislice calculations presented in this manuscript.

A more correct but also computationally more challenging way to describe TDS is the frozen phonon or frozen lattice approach. The approach is based on the fact that the high-energy electrons are so fast that they traverse the sample in a fraction of the time it takes a phonon to complete one oscillation cycle. Typical phonon frequencies are around 10^{13} Hz [26], meaning that it takes 100 fs to complete one oscillation cycle, while an electron at 200 kV traverses a 100 nm thick specimen in around 0.5 fs. Therefore, the atoms appear to be static from the point of view of the fast electron - it encounters basically a 'frozen' phonon. Thus, the scattering can be described by creating several of these 'snapshots' of the atom movements and calculating the interaction of the electron wave with each of these configurations and the resulting scattering from the sample. When the scattering from a sufficient amount of configurations is incoherently summed it reproduces the experimental data.
The frozen lattice approximation assumes that the displacements of the atoms are uncorrelated and utilizes the Einstein dispersion approximation, stating that all phonon modes have the same energy. Therefore, the displacement of each atom can be assigned from a Gaussian distribution of coordinates whose width is determined only by the Debye-Waller factor and the temperature. Muller et al. [51] have demonstrated that the outcome of correctly modeled frozen phonons and the frozen lattice approach is basically equivalent for the description of STEM images. Thus, simulations are often called frozen phonon calculations when they are in fact frozen lattice calculations (strictly speaking frozen lattice is also somewhat misleading as the simulated object can also be amorphous). The number of configurations to include to obtain a good result depends on several parameters but generally 10 configurations lead to a good description. Nevertheless, as this number multiplies with the amount of beam positions that are simulated, a large amount of individual simulations need to be calculated. The phase-gratings can be reused for every beam position, but the CPU time needed compared to an absorptive potential

calculation is still significantly higher (depending on the number of configurations).

Frozen lattice calculations are performed in the framework of this thesis using the STEMsim software package from Rosenauer et al. [52] which was provided in the framework of a collaboration. This implementation has the advantage to be able to output the angular-resolved scattering, allowing for an easy way to include the detector sensitivity and adding the flexibility to apply different detector geometries even after finishing the simulation. It has been shown that for thin specimens absorptive potential and frozen phonon simulations are practically equivalent while for thicker samples, where multiple phonon scattering and phonon-elastic scattering are non-negligible anymore, the results start to deviate [53, 54].

Simulation Parameters

Besides the parameters that determine the probe wave function (high tension, aperture size, defocus and limiting aberrations), several parameters are critical for the reliability of the simulation output. Periodic boundary conditions facilitate an infinitely extended potential of the slices, which means that intensity leaving one side will enter on the other side. To suppress the associated 'wrap-around error', the specimen size needs to be be large enough. Therefore, instead of having a single unit cell, the potential is augmented to include several unit cells in each direction and the simulation (different probe positions) is only performed on the center part of the potential. This is especially important for defects; instead of taking a single unit cell with e.g. a point defect, a phase-grating of several unit cells in each direction with only one defect in the center reduces the interaction of the electron wave with replica of the defect.
The sampling of the potential is also important and depends on the maximum scattering angle that needs to be simulated [26]. STEMsim already contains a routine to check if the entered sampling is sufficient. The formula is $S_x = \frac{2a_x\theta_{max}}{\lambda}$, thus the amount of pixels S_x needed in x direction is proportional to the maximum scattering angle θ_{max} and the unit cell size a_x in the given direction. It is advisable for frozen phonon calculations to set the maximum scattering angle substantially larger than the outer detector angle (e.g. twice) so that the influence of electrons which are initially scattered in a very high angle and then land on the detector by virtue of a second scattering event is correctly taken into account, which increases the accuracy.
The amount of beam positions that are needed within a unit cell to sample the high-resolution image sufficiently is substantially lower than the potential sampling. As the obtainable information is limited by the beam size, the width of the probe should be

a guide for a useful sampling in terms of scan points. A quarter of the beam width is normally sufficient to obtain a decent image [26] and afterwards a finer result can be obtained by interpolating.
The number of different configurations is also important. Generally, the more the better but this will dramatically increase the calculation time, so it should be adapted to the problem. Depending on the symmetry and the thickness of the crystal and if the scattering will be depicted as a diffraction pattern or just integrated on a detector the amount that is necessary to obtain an accurate result may vary but lies typically in between 5 and 20 configurations.

Channeling Theory

The state of the art of electron scattering simulations of fast electrons is obviously very advanced and precise results can be obtained by means of heavy number crunching. While these calculations are very useful, they are a kind of black box that does not offer an intuitive understanding of the propagation of electron wave functions through crystals. To gain a better understanding of the scattering process, and thus the image formation, the channeling theory shall be described in brief.
Pennycook & Jesson showed that mostly tightly bound Bloch waves contribute to STEM image intensities [41]. This concept was exploited by different groups to obtain simple expressions for image generation and thus to explained the relationship of high-resolution images obtained in zone axis and the projected potential of the structure [55, 43, 56]. The positive potential of the atoms forms a kind of channel for the electrons within which they can scatter dynamically without leaving it. For the high-energy Schrödinger equation, bound states arise from the atom potential. The projected column potential has only very few deep states. In the case of a sufficient column separation only the radial symmetric states, which are comparable to the 1S states of atomic orbitals, play a role. These states are very localized at the column positions. The amplitude of a wave traveling along an atomic column oscillates periodically and the periodicity of this oscillation is proportional to Z and inversely proportional to the distance in between atoms in the column. This is the dynamic extinction distance; intensity is shifted from the direct beam to diffracted beams and back while channeling down the column.
Within this picture it is more intuitively understandable what happens when an atom is e.g. displaced from a column position. The channeling is disturbed, giving rise to increased scattering out of the column and at the same time leading to a reduced intensity in the column after this atom and therefore to a reduced scattering from whatever follows.

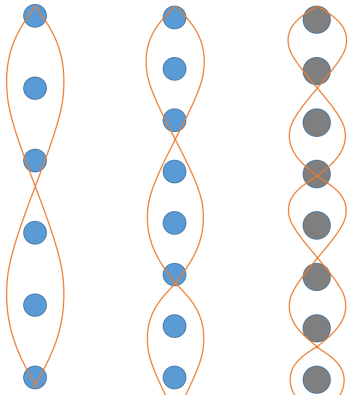

Figure 2.7: Sketch depicting the result of the channeling theory: For a crystal in zone axis with sufficient spacing in between atom columns the wave function is mainly channeled along these columns. While moving through the crystal, its amplitude oscillates and the period of this oscillation is proportional to the atomic number of the atoms and inversely proportional to their distance. Thus, when a fine electron probe is close to an atomic column with sufficient separation to its neighbors, mainly Bloch waves are excited that are strongly localized at the column positions. It should be noted that the amplitude is radially localized on the atom column and the drawn lines only represent the magnitude.

2.5 Resolution, Contrast, Noise and Precision in STEM

Resolution has always been an important characteristic of microscopes and is used to describe their performance. However, most criteria to determine resolution do not take into account noise, although STEM images are shot noise limited. Therefore, a metric that describes the quality of images in terms of noise is established, which is applied to the analyses in this manuscript. The discussion focuses on incoherent imaging at high-resolution, especially the case of HR-HAADF, as it is the mode for which it is the most relevant here.

The resolution that a microscope is theoretically capable of in a given setting can be derived from the transfer function of this setup. However, the real resolution depends on many factors, some of which are virtually impossible to predict and still difficult to measure, like current fluctuations in lenses or mechanical vibrations. And the resolution depends of course on the object that is being imaged and the quality of the detector. For incoherent imaging the lack of nodes in the transfer function implies that all frequencies that are transfered contribute to the resolution. Therefore, the resolution in an image is often defined by the visibility of spots in the FT of an acquired image of a crystalline specimen that correspond to resolved frequency components of the crystal periodicity.

Yet, visibility is not a good criterion because it is subjective and in the age of computers an unnecessary limitation to organ performance. A better criterion would be to define a threshold of intensity that can be measured. However, assuming one is not limited by the tool to measure the intensities, infinite resolution could be reached in the absence of noise because the transfer function approaches zero for higher frequencies but never reaches it (this is not true for coherent imaging due to the crossings of the abscissa which cancel out higher frequencies at a given point if lens current fluctuations are taken into account). The fact that information below the resolution limit can be obtained due to the incoherent nature of HAADF imaging was already pointed out by Pennycook et al. [20]. However, noise is always present and especially STEM images are severely limited by shot noise due to its relatively low beam current and serial image acquisition.
Thus, a definition of resolution needs to take into account noise, which is not the case for many criteria used in optics to define it. A criterion that includes noise is the Rose inequality [57] that was initially developed for television tubes, but can be adapted to determine noise-limited resolution in electron microscopy (see Spence [58]). It states that the resolution is inversely proportional to the dose per area that is applied to the sample. The higher number of electrons means that the SNR increases and image features can be better distinguished. Therefore, the quality of an image increases with the dose that is applied to the sample and this implies that better information can be extracted from the image with increasing dose. The factor how well the quality of an image scales with the applied dose depends on the microscope and mode (the transfer function). Phase contrast based imaging is for example very efficient in creating contrast and therefore signal at a given dose, however it is prone to perturbations. The precision with which an image feature can be determined should therefore depend on the SNR and this is investigated in Sec. 3.1.1. This does not imply that image intensities directly correspond to the position of atom columns in the sample and electron scattering simulations are necessary to clarify the situation (a case in which a stark discrepancy arises is discussed in Sec. 3.1.1). Nevertheless, the precision of pinpointing features is information about the sample, even if it needs simulations to render it comprehensible.
This is a concept similar to 'super-localization' that was used in fluorescence microscopy by Nobel laureate W. E. Moerner who found that the precision of determining the position of a fluorescing molecule augments linearly with the SNR [59].

It can be concluded that the quality of an image is determined by the SNR (at a given sampling). In Sec. 3.1.1 a method to determine the SNR in an image is established and the relationship between SNR and the precision of pinpointing image features is investigated.

From this discussion it becomes clear that obtaining a small as possible probe size (optimizing the transfer function) is actually very important. Not (only) because features can be 'resolved' but because it increases the SNR and therefore augments the information that can be extracted for a given dose. The current density of a probe and therefore the HAADF signal of an isolated atomic column increases with the inverse square of the beam size. Thus, striving for the best resolution at a given beam current means reducing the measurement time and the applied dose to obtain a certain SNR, therefore reducing beam damage, drift and other time- or dose-dependent quantities.

3 | Methods

In this chapter, the developments of different STEM based techniques that have been studied in the course of this thesis are presented. At the beginning of each section the state of the art is briefly described before reporting on the advancements and developments that were made in the framework of this thesis. The methods are grouped in three categories; first three techniques to measure strain are discussed before changing to the quantification of contrast and finally to the ways to image and measure electric (and magnetic) fields.

3.1 Strain Measurements in STEM

Three different methods to measure strain, or more generally, the local lattice distance, are presented in this section. They are ordered from highest to lowest spatial resolution. First, the measurement of atom (column) positions from HAADF-STEM is discussed, which offers atomic resolution. The second method is based on moiré fringes that are created from the interference of the scanning pattern and the crystal potential. This technique is limited to lower than atomic resolution because it undersamples the crystal periodicity. On the other hand it offers a higher strain precision. The last method is based on nano-beam precession diffraction and offers the ultimate strain resolution ($2{\cdot}10^{-4}$) while being limited to around 1 nm spatial resolution. Thus, these techniques serve different purposes depending on the spatial resolution, field of view (FOV) or strain precision that are required. Basics of linear elasticity theory for strain measurements in (S)TEM are summarized in App. B.

3.1.1 Strain from High-Resolution STEM

Incoherent imaging in the form of HAADF-STEM can be used to obtain meaningful atom positions from the analysis of intensities in the acquired images. As discussed in the framework of the channeling theory, the scattering is very localized at the atom column positions and the incoherent nature of HAADF means that interference effects

are negligible and therefore disturbances e.g. from contamination do not lead to drastic changes in contrast (cf. Fig. 3.1).

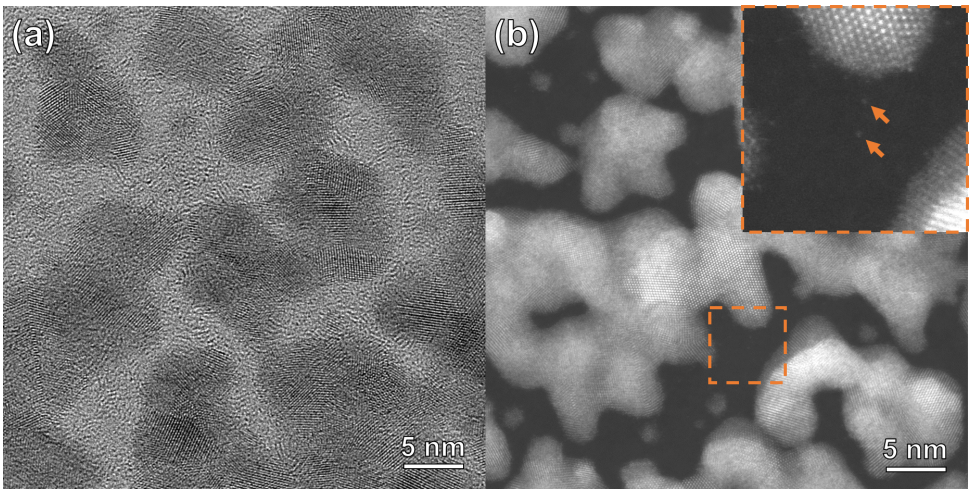

Figure 3.1: Comparison of coherent imaging in the form of HR-CTEM (a) and incoherent imaging by HAADF-STEM of Au nano-particles (NPs) on C support film, both C_s-corrected (objective and condenser, respectively) and at 200 kV. While the amorphous carbon leads to a strong and varying background contrast for CTEM, the Z contrast image exhibits only a low, homogeneous contrast from the film that even allows to see individual Au atoms (three atoms are marked by arrows).

Another important point is that contrasts in coherent imaging can change drastically and even invert with changing defocus. This means that in coherent imaging sloped surfaces can lead to a gradual contrast inversion within the image while for HAADF-STEM the main result is a blurring of the features, corresponding to a convolution with a Gaussian kernel. Although this blurring is detrimental to the precision it does not lead to a shift of the intensity maxima in the image.

Although being tempting due to the better visibility of light atoms in the presence of heavier elements in ABF-STEM [60], no quantification of atom positions is attempted for this imaging mode because of its partly coherent image generation. The changes in HR-ABF contrast due to small changes in experimental conditions that are also pointed out in Sec. 3.2.2 and Sec. 4.6 imply that no meaningful quantitative structure determination from ABF can be performed, at least without extensive image simulations.

Differences between intensity maxima in HAADF images and atom positions in the sample can only arise if columns are too close. From the channeling theory we know that the assumption that 1s states dominate the image formation does only hold for a sufficient separation of columns, otherwise other states will contribute. It has been shown by Hovden et al. [61] that in the case of very small column separation the difference between real and measured spacing might deviate. Nevertheless, the error is only large

for very thin samples, rather large beams and low beam energy. For the Si [211] dumbbell with 78 pm separation imaged at 300 kV with 25 mrad convergence angle the deviation they found is at maximum 3 pm for sample thicknesses up to 40 nm and below 1.5 pm for thicknesses above 60 nm [61]. Thus, for the high tensions used in the following (200 kV or 300 kV), the sample thicknesses of at least 25 nm (most results are from 50-100 nm FIB lamellae) and typically 24 mrad convergence angle the error should only be a few pm, even for very closely spaced columns. However, a few pm can already be a considerable error and therefore this effect is taken into account in the analyses that are performed in this manuscript.

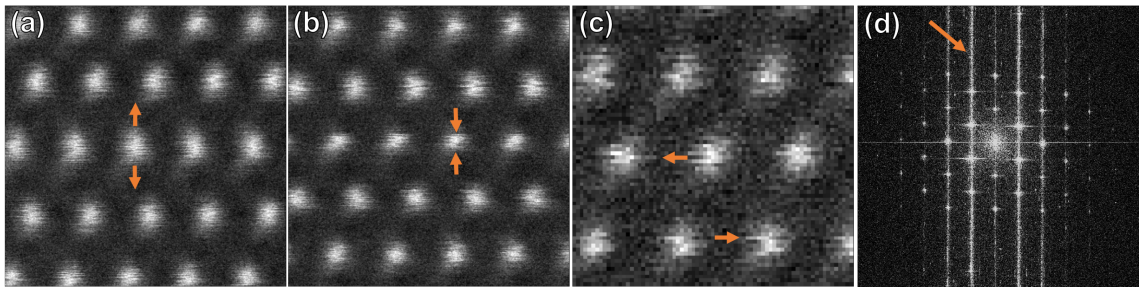

Figure 3.2: Artifacts in STEM images that can arise from the scanning process: Errors in the beam position along the slow scan axis (skips) that lead to an extension (a) or truncation (b) of the image and position errors along the fast scan axis (flags) that lead to a 'trailing' of intensities parallel or antiparallel to the fast scan axis (c). Skips are not very common and rather small while flags are ubiquitous in STEM images. Image (d) shows streaks (arrow) in the FT of a typical STEM image that originate from these scan artifacts.

A general problem of STEM that complicates quantitative image analysis are artifacts that arise from the serial imaging process. STEM is more sensitive to stray fields that deflect the beam during acquisition and therefore needs a better stability of the microscope to perform well. The influence of drift is also more complicated than in the case of CTEM because any time-dependent drift leads to a deformation of different parts of the image relative to each other. An important effect, even in the absence of stray fields and drift, are artifacts that arise from the scan generator itself as shown in Fig. 3.2. Due to hysteresis the probe may not return to the ideal position when 'flying back' at the end of each line to the beginning of the next line. This error can be augmented by choosing very short fly-back times. These errors are sometimes classified as 'flags' and 'skips': the flags are position errors in the direction of the fast scan axis leading to a 'trailing' of the intensities of a whole row and the skips are position errors in the slow scan direction that lead to a sudden truncation or extension of the image in this direction. The flags are much more pronounced than the skips because of the large jumps from the end of one line to the beginning of the next compared to the small change in position in the

slow scan direction.

Different ways have been proposed to correct scanning artifacts [62, 63, 64], yet the sample drift poses a problem. A way to cope with both is to register series of images that have been obtained from the same location. This can be facilitated in a simple manner by correlating adjacent images of a series and shifting them to correct for systematic drift between frames, which reduces all random (non-systematic) artifacts. This is called a rigid registration of images. A more sophisticated way to do so is by means of non-rigid registration that allows not only for translations in between frames but also for deformations within each image. This was e.g. done by Yankovich et al. by use of a variational approach [65]. Running the code on different binnings of the frames from high to low was necessary to avoid local minima. The authors claim 0.86 pm and 0.72 pm standard deviation of the peak positions in x and y coordinate, respectively, while rigid registration, which was used in comparison, led to errors of 5.3 pm and 4.0 pm. Another implementation of non-rigid registration is the Smart Align code from Jones et al. [66]. The correction of sample drift by rotating the scan direction incrementally in between individual frames of an image series, so called revolving STEM, was demonstrated by Sang & LeBeau [67].

The image registration software used in this manuscript is Zorro, a novel rigid-registration code that was developed by Robert A. McLeod [68, 69]. The basics of the Python based software are explained here, but the reader is referred to the original papers for detailed information concerning the code. The reason for using a rigid-registration code is threefold. First, it is much faster and as such can be routinely applied to image stacks and can also cope with many large images. A stack of several dozen 2048^2 pixel images takes only a few minutes on a decent desktop computer. This offers the possibility to use finer sampling in the images, which leads to a smoother statistical distribution of random image artifacts. Secondly, it is easier to control the registration process in the rigid case because it is only applying shifts to images and not (local) distortions. For non-rigid registration it is more difficult to validate the proper registration of images for a given situation. Last but not least, the results in terms of precision that are obtained using Zorro are comparable to what has been published for non-rigid registration, especially when coupling it with template-matching for atom position determination, while being very robust. Sub-picometer precision using Zorro and template-matching is demonstrated in this section.
Zorro is based on the masked intensity-normalized cross-correlation, as introduced by Padfield [70]. The intensity-normalization deconvolves correlated noise and the masking

reduces artifacts from the Fourier transformation. Each image can be correlated with each other and a figure of merit based on the statistical significance is attributed. This results in a triangular matrix where the elements close to the diagonal typically have the highest figure of merit and it decreases towards the corner. In (routine) application only a certain number of neighboring images are correlated because the correlations further away are either less good (e.g. sample evolving under the beam) or for stable conditions because a few correlations are already sufficient and the cost in computing time without additional benefit can be avoided. The figure of merit is used to attribute a weight by means of a logistic function to each equation in the minimization of the global error. This minimization is done in Zorro by utilizing the basin-hopping algorithm which can effectively escape global minima [71]. The code allows to change parameters like padding sizes, the number of neighboring cross-correlations, sub-pixel accuracy of the registration and many more. But they are mostly to set a general framework for the field of application (e.g. aligning HR-STEM images of crystalline specimens) or to modify the accuracy (thus changing the computing time) and do not drastically alter the outcome. An accuracy of 1/16th of a pixel and either five or seven neighboring cross-correlations were chosen for all registrations shown in this manuscript. Stacks of in between 12-60 images of 2048^2 pixels have been used with a sampling of typically 3-10 pm for atom position determination. Utilizing such a high sampling has the advantage that an atom column is described by many pixels, reducing the effect that individual scan errors have and thus contributing to a better definition of features.
An example of Zorro for aligning a PtCo nano-particle (NP) is shown in Fig. 3.3. A single frame from the series is depicted in (a), and (b) shows the result of the alignment procedure. The cross-correlation matrix can be seen in (c) with a color code that indicates the relative score. The axes correspond to the template and the base image; going from a pixel to the right shows the correlation score with the previous image and towards the top with the following frame. The sudden change in color means that something happened in the series and images (e) and (f) show that the particle rotated suddenly a bit (in (f) it is still in ZA, in (e) slightly off), leading to a lower correlation score.

After the image registration to reduce the influence of scan errors and drift is performed, a way to retrieve the atom positions is needed. HAADF images of atom columns are dominated by the PSF of the probe and can in good approximation be described as a convolution of the beam profile and the scattering potential. This profile can again be decently approximated by a 2D Gaussian function if asymmetric aberrations are sufficiently small. Although Verbeeck et al. have shown that the probe has in fact Lorentzian tails, these start rather far out and especially for fine probes their influence is small

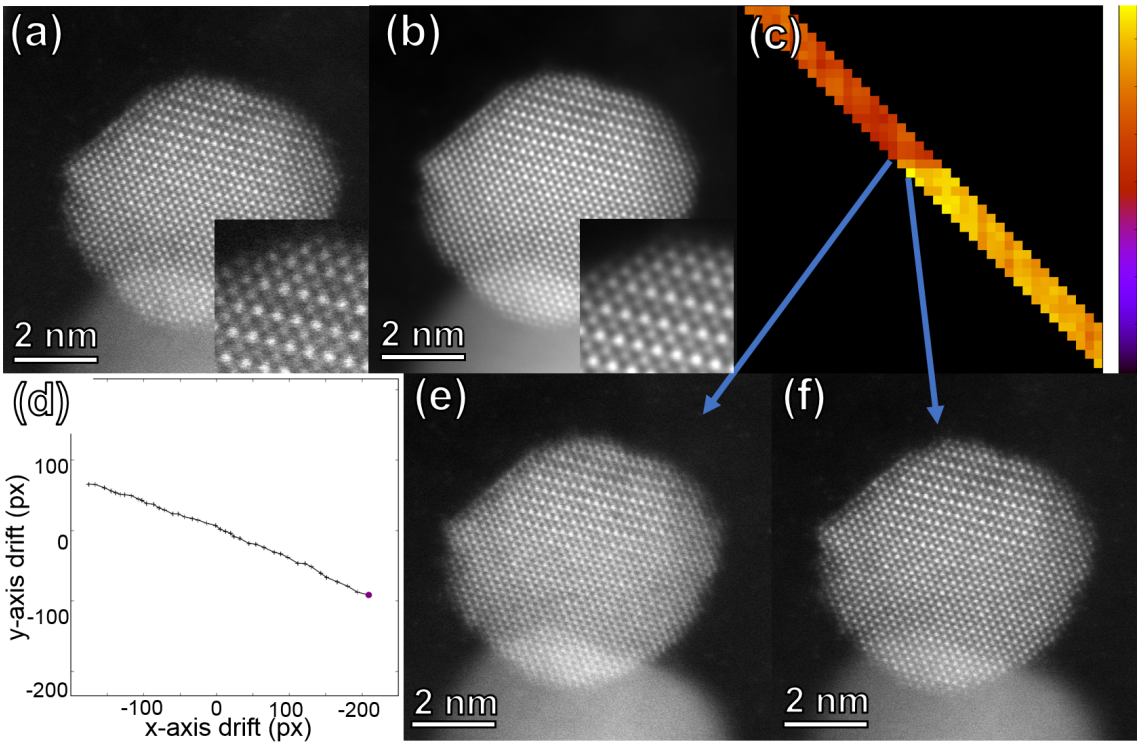

Figure 3.3: Image registration of a PtCo NP with Zorro: the initial image of the acquired series is shown in (a) and the final result in (b). The correlation matrix depicting the cross-correlation score is shown in (c) and the drift of each frame in (d). Images (e) and (f) show that the particle suddenly rotated a bit, effecting the change in correlation score seen in (c).

[72]. Therefore, atom positions are often determined by fitting 2D Gaussian functions to the image intensities, which generally works well. Yet, a faster and at the same time more precise method is used here: template-matching, implemented in the form of Zuo's template-matching analysis (TeMA) algorithm [64]. TeMA is a real-space based method, scripted in DigitalMicrograph and calling functions written in C to perform the calculations.

The template-matching analysis works by correlating an image S with a template T, which is typically a sub-region of the image (e.g. an atom column). To determine the degree of similarity between T and a region of S (of the same size as T) located at the position (x,y) in S, the so-called correlation coefficient function C_C is calculated

$$C_C(x,y) = \frac{\sum_{i,j}[S(x+i,y+j) - \overline{S}(x,y)][T(i,j) - \overline{T}]}{\sqrt{\sum_{i,j}[S(x+i,y+j) - \overline{S}(x,y)]^2 \sqrt{m\sigma_T^2}}} \,. \tag{3.1}$$

Here, m denotes the number of pixels in T,

$$\overline{S}(x,y) = \frac{1}{m}\sum_{i,j} S(x+i, y+j) \quad , \quad \overline{T} = \frac{1}{m}\sum_{i,j} T(i,j) \tag{3.2}$$

and

$$\sigma_T^2 = \frac{1}{m}\sum_{i,j} [T(i,j) - \overline{T}]^2 \ . \tag{3.3}$$

The correlation coefficient function is more robust than the cross-correlation function due to subtraction of the local averaged intensity, which is demonstrated in Zuo's original paper that gives more detailed information about TeMA [64].

The map produced by the correlation coefficient function points out positions where regions resemble the template image. This information can be used to average all the regions where the correlation function is above a given threshold value and thus obtain a template image with reduced noise. Assuming uncorrelated noise, the SNR of the template should increase by the square-root of the number of images averaged (if the images are identical). An example of this usage is given in Fig. 3.4 where the SNR of a very noisy image region (due to the low atomic number and a thick amorphous layer engulfing the whole specimen) is improved by template-matching and averaging the image regions that are similar. Image (a) depicts an AlN layer (blue box) in between the Si substrate and a GaN nano-wire (NW) grown on top. A region of the blue box is chosen as the template as shown in (b) and then correlated with the region of the blue box. The resulting thresholded correlation map is shown in (c) and the averaged template in (d). The method can (and was in this case) iteratively used by repeating the process and using the averaged template as the new starting template. The difference between the averaged template and the original region is striking and allows in this case for an unambiguous determination of the crystal polarity, i.e. the position of the N columns relative to Al.

The outcome is especially striking when the input image that is used in TeMA is already created from a registered stack. Then the SNR of an averaged template relative to a region in one of the images of the stack should be better by the square root of the number of images in the stack times the amount of positions averaged in TeMA (as will be demonstrated in Fig. 3.6). This allows to obtain virtually noise-free images (SNR well above 100 for pixel sizes of a few pm), which is used here to reliably measure the SNR in an image and this method is demonstrated in Fig. 3.5. Subtracting an averaged template from the original, not-averaged template leaves only the noise of this image, which can subsequently be analyzed. The averaged template is also useful to accurately determine the signal in the image, which can be difficult in noisy images.

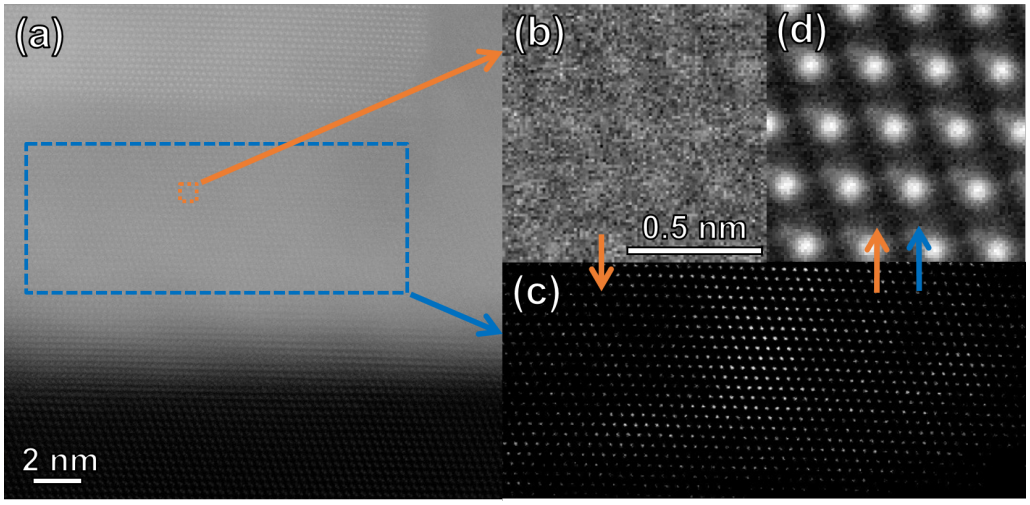

Figure 3.4: Demonstration of the averaging capabilities of TeMA: to enhance the image of an AlN pedestal (blue box) in (a) between a GaN NW (top) and the Si substrate (bottom) a template is cut from the original image (orange box, (b)) and compared to the region in the blue box. The resulting correlation coefficient map is given in (c) and using the peaks to average the template an image with improved SNR can be obtained (d) that clearly shows the polarity of the cubic AlN region.

A HR-STEM image of $Hg_{0.3}Cd_{0.7}Te$ obtained from a registered stack is given in (a) with a region cut from the image shown in (b) and the averaged template in (c). A small difference in dumbbell intensity can be seen, which is due to the average atomic numbers of the two columns according to the approximate composition given above (57.6 versus 52). The difference image between (b) and (c) is shown in (d) with the same intensity scale as in (b), and in (e) with enhanced contrast to better investigate the residual, which shows no structure. The SNR for the dumbbell intensity versus the background intensity around it is 13.3 and for the column intensities versus the dip in the dumbbell is 2.6. By splitting image (a) into two areas and creating an averaged template for each one, the templates themselves can be analyzed by subtracting them. The difference of the two templates on the same intensity scale as the template (c) before is shown in (f) and with enhanced intensity scale in (g). Interestingly, image (g) exhibits again structure. This contrast stems from a small difference in thickness of the two regions and is only visible because the noise is extremely low. With this method we can calculate the SNR of the averaged template. The values when defining the signal as peak-to-background and peak-to-dip are 238.7 and 47.4, respectively.

A more detailed analysis is given in Fig. 3.6 where the noise that is left after subtracting a 328 times averaged template from templates that were created from 1, 4, 10 and 64 averaged regions of a GaN [0001] crystal. For the off-column positions the experimental values (orange diamonds) agree well with the a square-root dependence starting from

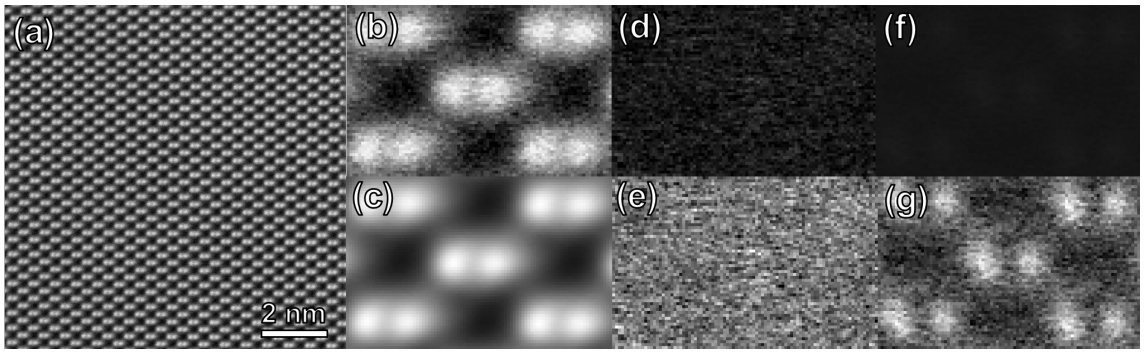

Figure 3.5: An HR-HAADF image of $Hg_{0.3}Cd_{0.7}Te$ from a registered stack (a), a template taken from this image (b) and the averaged template (c). The difference between (b) and (c) is displayed in (d) on the same intensity scale and enhanced in (e). The difference between two averaged templates is shown in (f) and (g) for same scale as before and enhanced, respectively.

the value for the un-averaged template (orange line). If the whole template area is taken into account, the fit is less good for higher numbers of averaged templates (blue data). The reason being that the assumption that all columns in the image are identical does not hold anymore and e.g. small differences in local thickness lead to slightly different column intensities while leaving the background mostly unchanged (cp. to Fig. 3.5 (g)). If the number of averaged templates gets close to the amount that has been used to create the 'noise-free' template which is subtracted, then the assumption that it is noise-free also does not hold anymore. In the case that both have been created by the same amount of images (but not the same images!) then the noise should be increased by $\sqrt{2}$, an overestimation of the noise by over 40 %, which is why the maximum number of averaged images was kept well below that of the template. This analysis demonstrated that the SNR in STEM images increases with the square-root of the number of averaged images. It should be noted that this is true for the case of images where scan artifacts are negligible.

The number of electrons in the incoming beam varies due to the shot noise and is therefore described by a Poisson distribution. As only a fraction P of the incoming beam is collected by a detector after it interacted with a sample, a Binomial distribution of the Poisson distribution needs to be calculated. The outcome of which is again a Poisson distribution with mean $\overline{PN}$ and standard deviation $\sqrt{\overline{PN}}$. More information can be found in App. A.

When operating within the linear response regime of the detector and subtracting the vacuum noise level from the images, the absolute ratio of intensities can be determined (more information is given in Sec. 3.2). The square-root of this ratio should correspond

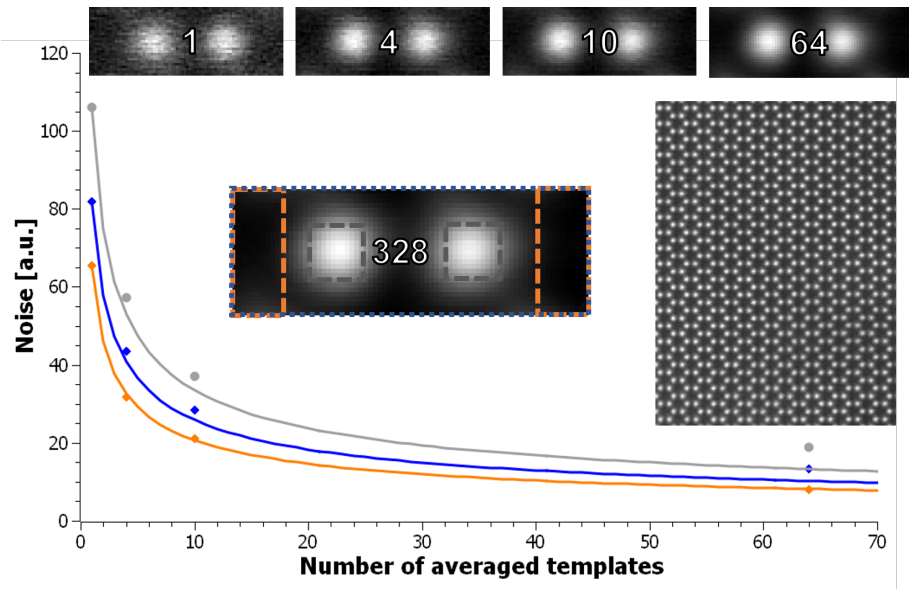

Figure 3.6: To evaluate the behavior of the noise level (standard deviation) different numbers of templates from the given image are averaged. Each time the reference template (created from 328 templates, assumed to be noise-free) was subtracted and the noise in different regions of the image analyzed. For the background (marked orange) the noise agrees well with a square-root dependence (solid orange line), for the total area and column positions a deviation can be seen that is explained in the text.

to the ratio of noise of these two regions. It is easier to evaluate the noise utilizing low-resolution images that have a constant intensity. Measuring standard deviation and intensity of regions of different thickness of a homogeneous sample and comparing the ratio of noise levels with the square-root of the ratio of intensities agrees reasonably well and therefore the noise is assumed to be Poisson distributed (the influence of the DQE of the detector is discussed in Sec. 3.2.1).

Fig. 3.7 shows the behavior of the precision of position determination in dependence of the SNR. A computer generated image depicting a 20x20 array of two-dimensional Gaussian functions with peak to background ratio of 2 and 50 px pitch in horizontal and vertical direction is utilized to evaluate TeMA. By changing the total intensity of the image (dividing the image by a given factor) and subsequently adding Poisson noise to every pixel according to its intensity (facilitated by a MATLAB script), different SNR images were created. The positions are determined for each image and compared to the positions of the regular grid. The resulting standard deviation is plotted against the SNR. The 1/SNR graph (gray line) is in good agreement with the data points (orange diamonds). The data point at the right is a bit too low because the precision is approaching the sub-pixel accuracy limit of TeMA. As the grid is generated in a way that the center of the columns are at integer pixel values, this results in an overestimation of

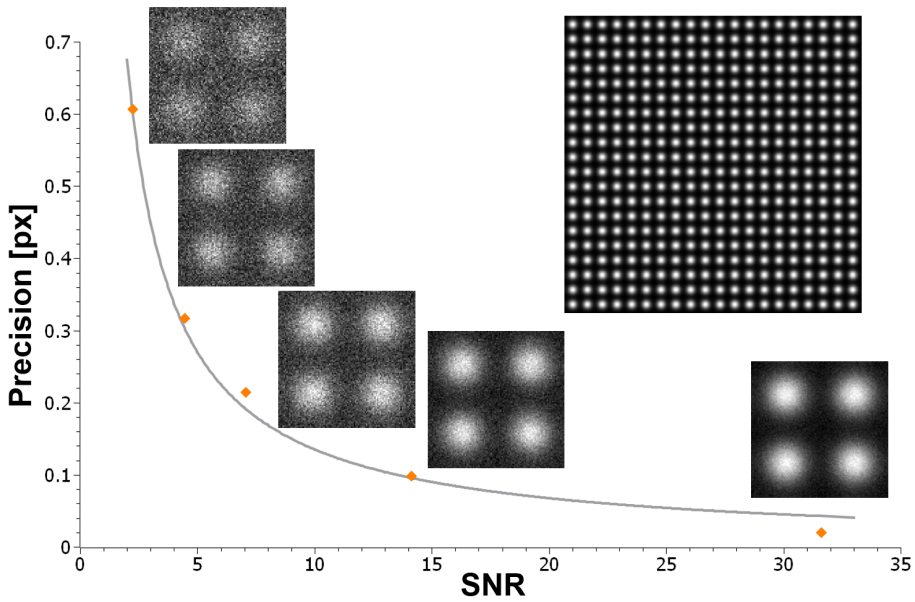

Figure 3.7: Relationship between the precision of atom position determination via TeMA and the SNR of the images, evaluated by means of computer generated images. The noise-free 20x20 column lattice is shown and zooms for the different SNR values that were evaluated are displayed next to the graph. The orange diamonds represent the data points and the gray curve corresponds to 1/SNR.

the precision. Nevertheless, a 1/SNR dependence of the position determination seems to be a good approximation.

In Fig. 3.8 the performance of atom position determination by TeMA of image series registered with Zorro is demonstrated. Image (a) is composed of 61 2048^2 px images with 8.15 pm/px sampling. They were obtained at 200 kV with 24 mrad convergence angle, 118 pA beam current and 0.2 µs dwell time. The SNR of the registered stack is 20.4 using the average noise of the whole template and defining the signal as the difference between peaks and the surrounding of the dumbbells, because the whole dumbbell is fitted in this example (and not the two columns separately). To measure the precision, the lattice of the crystal is determined via TeMA. TeMA can fit a lattice to the found peaks by minimizing the deviation between the found column positions and the lattice. This residual differences between lattice positions and determined positions yields the error of the position determination if the imaged crystal is regular. The histogram of the errors that were determined is depicted in (b) and the precision in the horizontal and vertical direction is 1.26 pm and 1.46 pm, respectively. A second example is shown in (b). Here, 27 2048^2 px images with 2.47 pm/px sampling are aligned and the microscope parameters were 300 kV high tension, 24 mrad convergence angle, 70 pA beam current and 0.8µs dwell time. The resulting SNR is 17.7 and the resulting errors (shown in (d)) account for a precision of 1.36 pm horizontally and 0.95 pm vertically (the image is

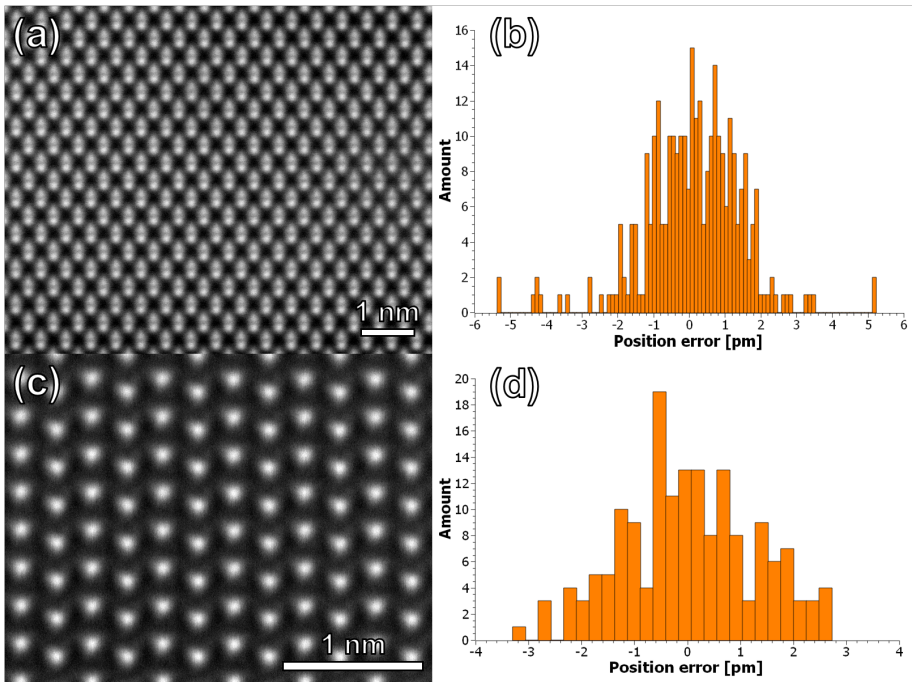

Figure 3.8: The precision of atom position determination from TeMA for two examples: (a) depicts a registered series of HgCdTe in [110] ZA where the dumbbell as a whole was used as template and (c) of GaN in [11$\bar{2}$0] ZA using a aingle Ga column as template. The respective histograms of position errors are shown in (b) and (d). The error in (a) is 1.26 pm and 1.46 pm and in (b) 1.36 pm and 0.95 pm for the horizontal and vertical axis, respectively.

rotated, the fast scan axis was originally horizontal). Thus, a precision not far from what has been published using non-rigid registration is achieved here for decent experimental data and the combination of TeMA and rigid registration with Zorro. When comparing TeMA and the fitting of two-dimensional Gaussian functions to the same data, fitting yielded 74 % larger errors. This was only evaluated for one example and no systematic study depending on the SNR was performed, but it demonstrates the better performance of TeMA.

However, care needs to be taken when using TeMA. An example of artificial strain from incorrect usage is shown in Fig. 3.9. In this case a ZnTe/CdSe superlattice in [110] ZA is investigated, depicted in (a), and a strain map of the component perpendicular to the interfaces produced from atom positions that are determined in TeMA by using a whole dumbbell as template is shown in (b). The interface on the left-hand side exhibits a lattice contraction of more than 10 % relative to the ZnTe while the interface on the right-hand side exhibits a positive strain. In Sec. 4.1 it is demonstrated that the strain is around -7 % for both interfaces. As the template is static but the dumbbell width in the image changes slightly and is accompanied by a contrast inversion within the dumbbell

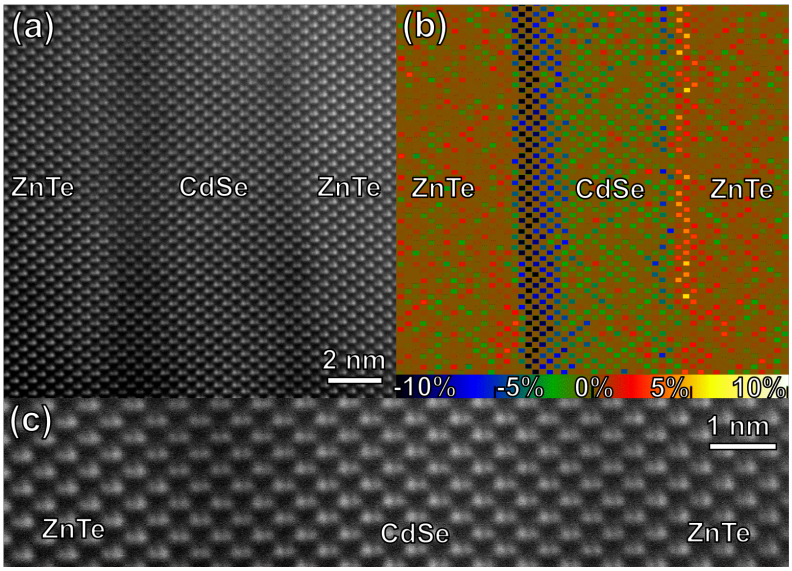

Figure 3.9: Demonstration of artifacts in strain measurements from TeMA when done incorrectly: a ZnTe/CdSe superlattice in [110] ZA (a) and a corresponding strain map (component perpendicular to the interfaces) from TeMA atom positions when using the whole dumbbell as template. Due to the changing dumbbell spacing and the contrast inversion within the dumbbell when going from ZnTe to CdSe (better visible in (c)) the regions where the contrast changes show artificial strains. In reality the two interfaces exhibit similar strain (demonstrated in Sec. 4.1). It should be noted that for the homogeneous regions the result is correct.

(cf. (c)), the best match between template and image is obtained for small shifts relative to the correct positions. These shifts have a different sign at the two interfaces because of the contrast inversion within the dumbbell. It should be noted that this is only a problem for the interfaces; the layers themselves exhibit the correct strain values. Thus, the usage of a dumbbell as template is only valid to compare two regions but not for strong strain gradients in between.

In the beginning of this section it is argued that inferring atom positions from intensity peaks in HAADF images is reliable and, at least for the microscope parameters used in this manuscript, deviations from the real structure are small. One phenomenon for which this does not hold anymore was encounter while investigating inversion domain (ID) boundaries (IDBs) in GaN (an in-depth investigation is presented in Sec. 4.6). For the case that atom columns do not run through the whole crystal, substantial deviations between image intensity peaks and the atom structure occur. This is shown in Fig. 3.10 where HAADF images for a model of a kinking GaN inversion domain boundary in $[11\bar{2}0]$ ZA and a test structure are simulated and subsequently analyzed. Multislice absorptive potential calculations of 12.8 nm thick samples for 300 kV, 24 mrad convergence angle and 72-260 mrad detection angle are performed for each structure. In the first case the

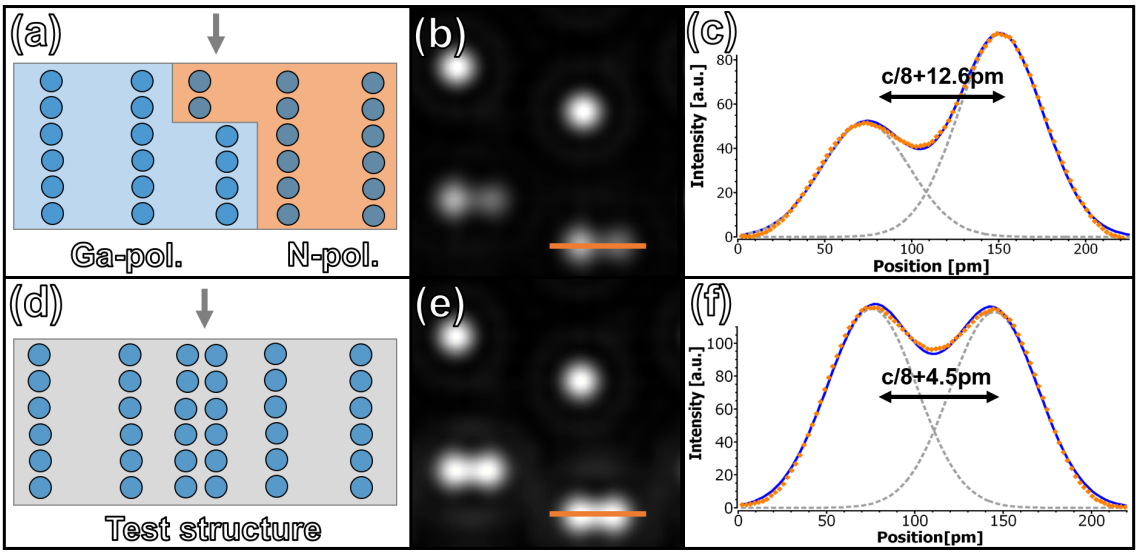

Figure 3.10: Influence of interrupted atom columns on intensity maxima in HAADF images: a schematic drawing of a kinking inversion domain boundary in GaN in $[11\bar{2}0]$ ZA is shown in (a) with corresponding multislice simulation (b) and fitted line profile in (c) using two Gaussian functions. The profile is depicted in orange and the fit in blue. A hypothetical test structure with uninterrupted Ga columns is depicted in (d) with simulation result in (e) and fitted line profile in (f). While the test structure exhibits a deviation between intensity maximum and and atom position of 4.5 pm, the first structure yields an error of 12.6 pm.

Ga column of the N-polar region is interrupted after 1/4 of the sample thickness and an adjacent Ga column from the Ga-polar region starts (cf. (a)). The corresponding simulation result is shown in (b), where the upper part is the pure Ga-polar crystal and the bottom half shows the superposition. The distance of the dumbbell in the crystal model is, according to the GaN structure, c/8 = 64.8 pm. A line profile across the dumbbell is fitted with two Gaussian functions in (c). The visible separation of the two columns is 12.6 pm larger than c/8. For the test structure shown in (d), where both dumbbell columns run through the whole crystal the deviation is only 4.5 pm as depicted in the fitted line profile (f) of the simulation output (e). To compare with the results of Hovden et al. [61] that are already mentioned at the beginning of this section, they found around 3 pm difference for a 78 pm separated Si dumbbell for 300 kV and 25 mrad convergence angle at 10 nm specimen thickness in their simulations. Therefore, the influence of truncated columns within the crystal can produce a much more significant error than just closely spaced continuous columns. This effect is also experimentally observed and the results can be found in Sec. 4.6.

3.1.2 Strain from Scanning Moiré Fringes

A phenomenon that can sometimes be observed when changing the magnification in HR-STEM to a slight undersampling is the arising of a fringe pattern (cf. Fig. 3.12). These fringes are a moiré that originates from the interference between the periodicity of the crystal potential and the scan grid. Su and Zhu explained the theory of these patterns and proposed to use them to study crystal structure properties at medium magnification [73]. A few years later, Kim et al. published their results for (one-dimensional) strain measurements in semiconductor devices by using the scanning moiré fringes to have a larger FOV and enhance the change in lattice distances [74, 75, 76]. Recently, Hÿtch et al. presented results showing two-dimensional strain mapping via SMF (using two separate images) and making use of geometric phase analysis (GPA) to do so [77].
The usage of GPA for the analysis of patterns was independently applied during this thesis, but in addition several new improvements have been made concerning the acquisition process that lead to better, customizable and fine-tunable patterns. This is explained in detail in this section and later on applied to a semiconductor device for strain mapping in Sec. 4.2.

The moiré patterns emerging from HR-STEM images where the scan step size is slightly larger/smaller than the periodicity of the crystal potential (cf. 3.12) are a form of aliasing, arising from the sub-sampling. According to the Nyquist-Shannon theorem the frequency of the scanning beam must have at least twice the frequency of the crystal potential to sample it unambiguously. The scanning moiré fringe technique is a form of compressed sensing in which we use our prior knowledge about the (unstrained) lattice to extract the needed information from the moiré although the Nyquist-Shannon criterion is not fulfilled.

For a reciprocal lattice vector $\mathbf{g_l}$ and a vector in reciprocal space describing the scanning frequency of the probe $\mathbf{g_s}$ the vector describing the moiré fringes, $\mathbf{g_m}$, is described by the moiré formula [22]

$$\mathbf{g_m} = \mathbf{g_l} - \mathbf{g_s} \ . \tag{3.4}$$

When having parallel vectors $\mathbf{g_l}$ and $\mathbf{g_s}$ the spacing of the fringes in real space d_m is given by

$$d_m = \frac{1}{g_m} = \frac{1}{g_l - g_s} = \frac{d_l d_s}{d_s - d_l} \tag{3.5}$$

where d_l and d_s describe the to g_l and g_s respectively corresponding real space distances. We now introduce a rotation between $\mathbf{g_l}$ and $\mathbf{g_s}$. Without loss of generality we describe the scan vector as aligned with the x-direction of our Cartesian coordinate system and the lattice vector as rotated relative to that by the angle α_l and split Eq. 3.4 into its x- and y-components:

$$\begin{aligned} g_{m,x} &= g_l\, cos(\alpha_l) - g_s\ , \\ g_{m,y} &= g_l\, sin(\alpha_l)\ . \end{aligned} \tag{3.6}$$

The frequency of moiré fringes is therefore

$$g_m = \sqrt{g_l^2 + g_s^2 - 2\, g_l\, g_s\, cos(\alpha_l)}\ . \tag{3.7}$$

The period of the moiré fringes in real space can be expressed as

$$d_m = \frac{1}{\sqrt{g_l^2 + g_s^2 - 2\, g_l\, g_s\, cos(\alpha_l)}} = \frac{d_l\, d_s}{\sqrt{d_l^2 + d_s^2 - 2\, d_l\, d_s\, cos(\alpha_l)}}\ . \tag{3.8}$$

The rotation angle of the fringes α_m relative to the unrotated case can be calculated as

$$\alpha_m = arccos(\frac{g_{m,x}}{g_m})\ . \tag{3.9}$$

Scanning moiré patterns can be adjusted by changing the number of pixels in the image. The acquisition softwares normally attribute a given FOV size to a magnification and changing the number of pixels leads to a different sampling of this area. Yet, this is only true for keeping the number of pixels in both directions equal. If different numbers of pixels are chosen, the aspect ratio is normally changed to keep the pixels square.

Scanning moiré patterns can be used to fine-tune the scanning process. Typically, STEMs allow for an adjustment of the scanning pattern by means of a provided software. Tuning the scan pattern is normally necessary after tuning the pivot points. In the case of the microscopes that were used, the program acquires images of a waffle grid test specimen and determines the vectors that describe the grid by means of cross-correlation. The scanning pattern is iteratively adjusted until the vectors have the same length and are perpendicular. By comparing alignment files before and after running the program, the values that control the scanning pattern can be found. Creating a two-dimensional moiré pattern of a reference crystal in a square ZA allows for a precise adjustment of the scanning because the moiré amplifies any deviations and a crystal potential is a better reference than most mesoscopic test specimens.

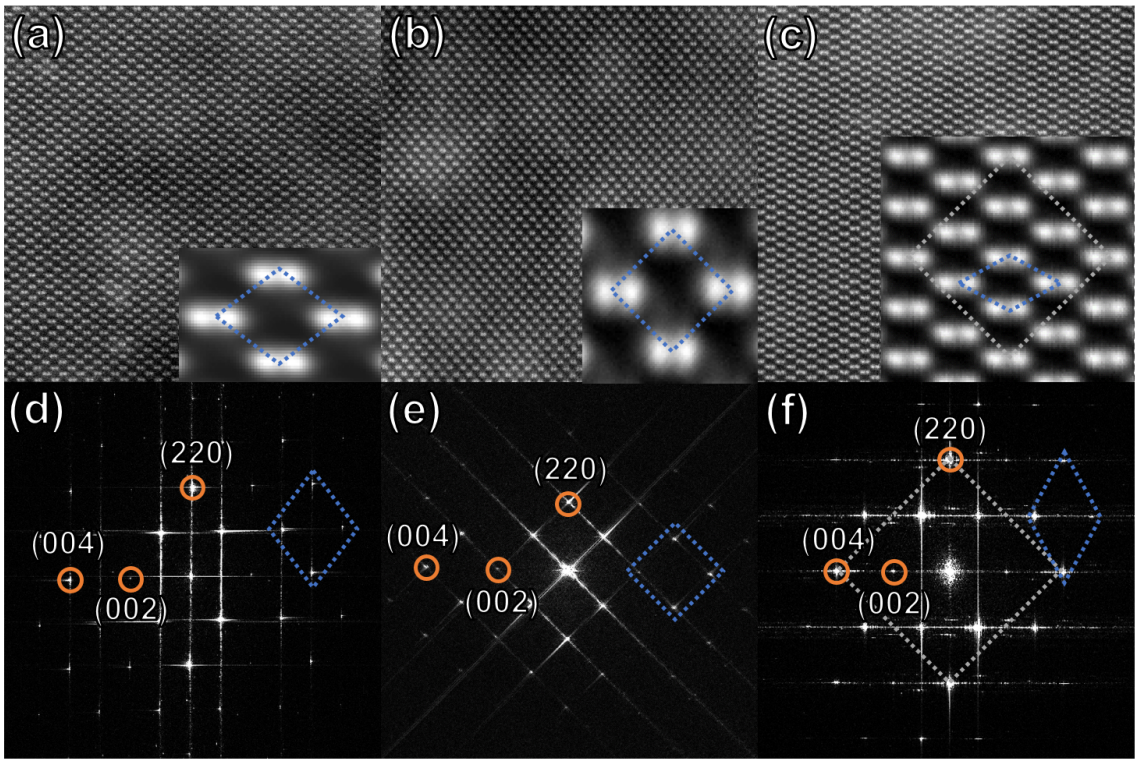

Figure 3.11: A Si crystal imaged in [110] ZA with different settings of the scan distortion: a square scan pattern producing a typical image (a) and two rectangular scan patterns that produce a square grid for either (002) and (220) planes (b) or (004) and (220) planes (c). The corresponding FTs are depicted below each image.

The requirement of Eq. 3.4 generally only allows for two-dimensional moiré patterns in cases where a square symmetry of the crystal ZA is given. The access to the scan pattern adjustment offers the possibility to deform the grid intentionally to make a non-square crystal ZA look square. This is demonstrated in Fig. 3.11. A typical HR-HAADF image of Si in [110] ZA is shown in (a) with the corresponding FT in (d). The ratio between the (220) and (002) spots is $\sqrt{2}$. In (b) an image after tweaking the scanning is shown and the resulting FT in (e). Changing the scan pattern to a $\frac{1}{\sqrt{2}}$ aspect ratio results in the same spacing of (220) and (002) planes. For (c) the aspect ratio was changed to $\sqrt{2}$:1 which leads to the same spacing of (220) and (004) planes. Therefore, the tweaking allows to create two-dimensional moiré patterns for basically every crystal and ZA (within the limits of the scan adjustment).

This is exploited in Fig. 3.12 to obtain two-dimensional scanning moiré patterns of a SiGe/Si device imaged in [110] ZA. In (a) d_s is slightly smaller than d_l of (220) and (002) planes, giving rise to a moiré with large spacing that exhibits a smaller periodicity in the SiGe regions, where d_l is larger. The scanning step size is changed to be slightly larger than d_l in (b). This leads to a larger moiré in the SiGe region compared to Si. A

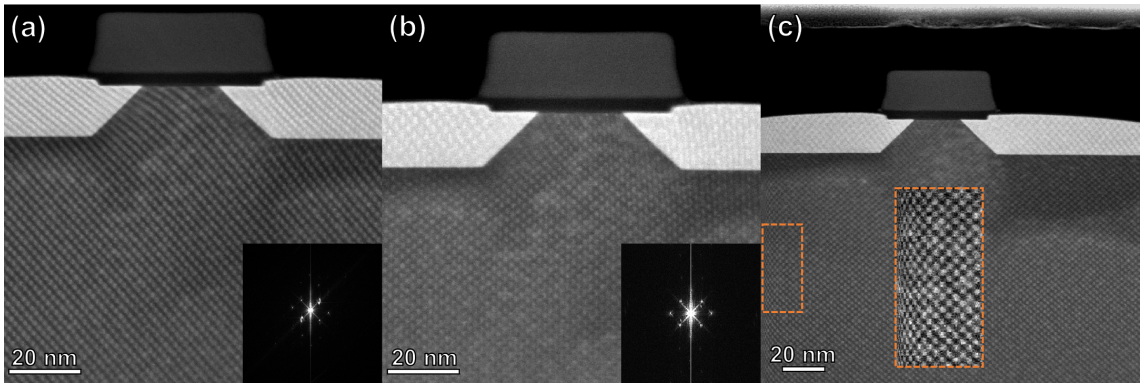

Figure 3.12: Two-dimensional scanning moiré patterns of a SiGe/Si transistor in [110] ZA. In image (a) the scan step size is smaller than the lattice distance giving rise to a smaller moiré spacing in the SiGe region where the lattice is larger. The reverse case, where d_s is larger than d_l is depicted in (b), yielding a larger d_m in the SiGe region. The effect that the scan step size is slightly larger at the beginning of each line can be seen in (c), therefore the leftmost part of all images is normally cropped.

common artifact of scan generators can be observed very well in (c): the moire pattern ($d_s > d_l$) is much smaller at the leftmost border of the image, indicating that the scan step size is larger at the very beginning of each line. Therefore, images are cropped for strain analysis (this has also been done for every image analyzed in Sec. 3.1.1).

To determine strain from a moiré pattern d_m and α_m are measured and the (local) lattice spacing d_l and angle α_l need to be deduced. The spacing d_l can be calculated as

$$d_l = \frac{d_m\, d_s}{\sqrt{d_m^2 + d_s^2 \pm 2\, d_m\, d_s cos\,(\alpha_m)}} \tag{3.10}$$

and the rotation α as

$$\alpha_l = sign(\alpha_m)\, arccos\left(\frac{d_s}{2d_l} + \frac{d_l}{2d_s} - \frac{d_l d_s}{2d_m^2}\right) . \tag{3.11}$$

It is inherently not known if $d_s > d_l$ or $d_s < d_l$ as the moiré relies on the fact that the sampling is lower than the Nyquist frequency and because only $|d_m|$ is measured and therefore Eq. 3.10 contains a variable sign accounting for the two cases.

To calculate the strain (cf. App. B) the distortion along the axis of the initial Euclidean coordinate system can be determined as

$$\underline{\mathbf{D}} = \begin{bmatrix} cos(\alpha)\, d_{l,1} & sin(\alpha)\, d_{l,2} \\ sin(\alpha)\, d_{l,1} & cos(\alpha)\, d_{l,2} \end{bmatrix}^{-1} \begin{bmatrix} d_{l,1,ref} & 0 \\ 0 & d_{l,2,ref} \end{bmatrix} - \mathbb{1} . \tag{3.12}$$

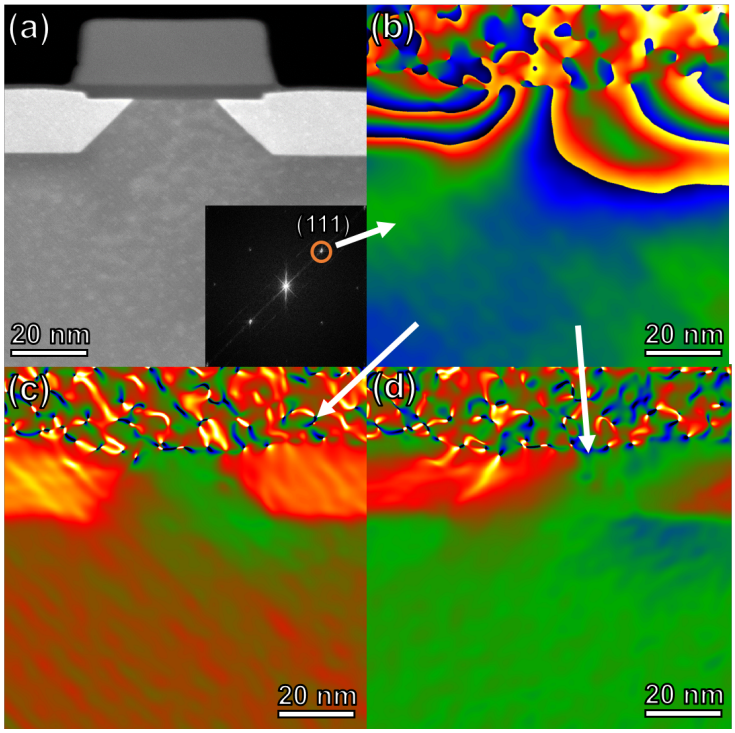

Figure 3.13: Analysis of a scanning moiré pattern using GPA: the pattern is shown in (a) with the corresponding FT as an inset. Here, a spot corresponding to a (111) moiré is chosen with a Gaussian mask and the geometric phase is depicted in (b). From this phase, maps of the moiré period d_m and angle β are determined and depicted in (c) and (d), respectively. This is done just exemplary; for a full, quantitative analysis see Sec. 3.1.2.

Generally, d_s can be set to unity and d_m expressed in pixels because strain is relative. In the case of two-dimensional moirés, any asymmetry of the scanning directions can be taken into account by measuring the moiré periods for a reference region and using the ratio of lattice spacings that is known in this region. Setting $d_{s,1} = 1$ and using Eq. 3.10 allows to calculate $d_{l,1,ref}$ in units of $d_{s,1}$. The known ratio $d_{l,1,ref}/d_{l,2,ref}$ then makes it possible to determine $d_{s,2}$ using

$$d_s = \frac{\pm d_m d_l^2 cos(\alpha_m) + \sqrt{d_m^2 d_l^4 cos^2(\alpha_m) + d_l^2 d_m^2 (d_m^2 - d_l^2)}}{d_m^2 - d_l^2} \,. \tag{3.13}$$

An example of using GPA to extract information from a two-dimensional scanning moiré pattern is given in Fig. 3.13. Geometric phase analysis is a powerful, yet common, tool to measure strain in lattices and the reader is referred to the literature for more details on the method [78, 79, 80]. The small moiré spacing of only a few pixels is normally more useful than what is shown in Fig. 3.12 because the spatial resolution can be much better and analyzing high spatial frequencies is no obstacle for GPA. The geometric phase map of the (111) moiré from (a) is shown in (b) and the d_m and β maps are depicted in

(c) and (d), respectively. A detailed, full analysis of a two-dimensional scanning moiré pattern is demonstrated in Sec. 3.1.2.

Recently, it was pointed out by Peters et al. [81] that GPA can produce artificial strains at interfaces. The authors established that to avoid a geometric phase originating from sub-lattice contrast and not from strain, the following condition has to be met:

$$\mathbf{G} \cdot \mathbf{r}_{subl} = \nu \tag{3.14}$$

Where $\mathbf{G}$ denotes the chosen reciprocal lattice vector, $\mathbf{r}_{subl}$ the real space vector defining the displacement between the sublattices and ν is an integer. For the case of a zincblende structure in [110] zone axis $\nu = \frac{1}{4}$ and therefore the (004) planes are suitable for GPA analysis while the commonly used (002) planes are not. Therefore, the setting of Fig. 3.11 (c) is utilized for the analysis in Sec. 3.1.2, rather than (b).

3.1.3 Strain from Nano-Beam Precession Diffraction

Scanning nano-beam diffration is a powerful method that has been used to map crystal phases and orientations in different materials. A review of the technique and its applications can be found e.g. in Rauch et al. [82]. For beam-sensitive materials the combination of a small scanning probe and the use of diffraction allows to extract invaluable information from samples that would otherwise be difficult to obtain. This was demonstrated by the author in a work prior to this thesis for the case of van-der-Waals bonded organic semiconductors where morphology and structure could be linked with this method [83]. The technique is especially powerful when combined with precessing the beam. Precession diffraction has been proposed by Vincent & Midgley [25] and the effect of rocking the beam around a ZA is a diffraction pattern with more diffracted beams and intensities being more kinematical due to the summation of the off-axis tilts. The utilization of nano-beam diffraction to measure strain was demonstrated in 2005 by Usuda et al. [84]. However, only a line profile of a few points was presented. More recently, with the advances in acquisition and processing NBED allowed to produce large strain maps [85]. The setup for deformation mapping is normally slightly different in that the convergence angle is higher compared to the almost parallel probe for phase and orientation mapping, leading to discs in the diffraction plane but also to a smaller probe size. Here, precession is also very useful because it averages contrasts in the discs out, which leads to a better detection of the disc positions.
The strain measurements that are demonstrated here are done using an alpha version of the FEI Epsilon software for acquisition of the data and a DigitalMicrograph based

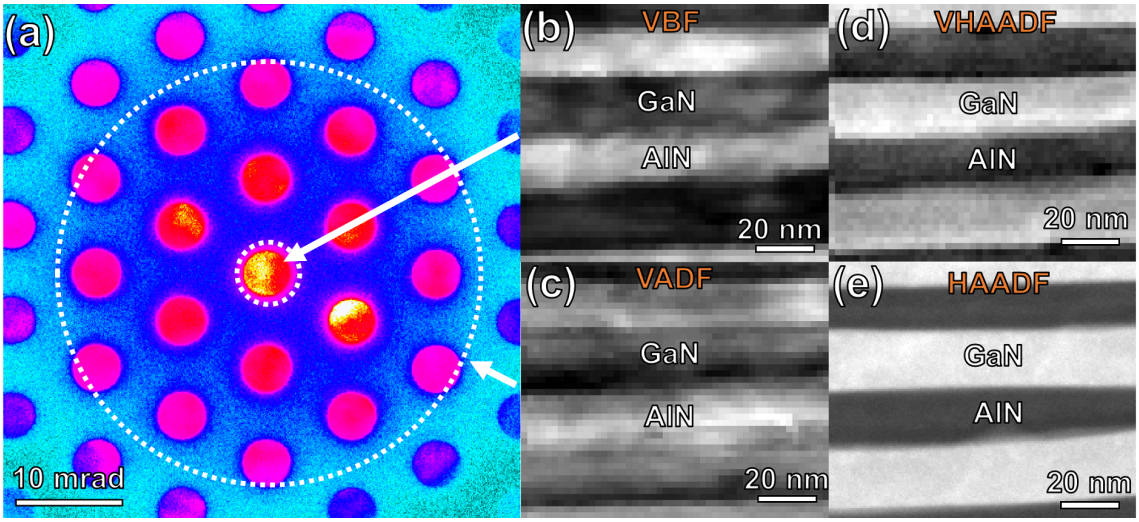

Figure 3.14: Comparison of virtual images obtained from placing digital apertures in a series of diffraction patterns with conventional HAADF. (a) is a diffraction pattern on logarithmic color scale of a series of NPED diffractograms of an AlN/GaN sample in [0001] ZA. Virtual bright field (b) (intensity within small white circle), virtual annular dark field (c) (intensity outside large white circle) and virtual high-angle annular dark field (d) can be calculated from the data. The VHAADF agrees well with the conventional HAADF data (e) (not from the same area).

script, written by Jean-Luc Rouvière for processing. The Epsilon software was available in the framework of the 'common lab' project between CEA Grenoble and FEI company. It facilitates the precession, scanning and synchronized acquisition on the FEI Ceta camera (CMOS). It also allows to tune the precession and de-rocking of the beam to obtain a stationary, small beam and a focused diffraction pattern at the same time. Typical parameters for the acquisition of data are 2-3 mrad convergence angle, 0.3 degree precession (semi) angle, 100 Hz precession frequency and 100 ms exposure time on a two-times binned quarter readout of the camera (512^2 px instead of the full 4096^2). The size of the diffraction limited beam (FWHM) for a convergence angle of 2 mrad (3 mrad) at 200 kV is, according to Eq. 2.3, 0.5 nm (0.75 nm). If the precession is well tuned it adds only about 0.1 nm to the beam width. This is before interacting with the sample and not to be confused with the resolution of the experiment.

An important step besides the acquisition is the automated and precise analysis of the diffractograms. Here, a homemade script is used that was written by Jean-Luc Rouvière and is based on auto-correlation. The periodic nature of diffractograms from crystals leads to a sharply peaked correlation function at the center positions of each diffraction disc, which facilitates the measurement of the disc spacings in different crystallographic directions. These distances are inversely proportional to the spacing of the respective lattice planes and measuring the change of distances in directions that are linearly in-

dependent allows not only for the calculation of the strains in these two directions, but also the shear and rotation (within the plane perpendicular to the beam).

A common way to define the spatial resolution of the NPED measurement is to image the probe after traversing the sample [86, 85]. But this measures the beam size after widening from the whole thickness of the sample, which can be considered an upper boundary of the size. A method to assess the probe size more correctly is proposed here; virtual images of interfaces can be compared to HR-HAADF data. The HR-HAADF images yield the real interface width due to the small size of the probe, and thus the beam width of the NPED experiment can be measured by comparison.
Virtual images can be calculated from the diffraction data by placing a digital aperture in each diffraction pattern and integrating the intensity from that given data. Displaying this value, as e.g. grayscale, for each diffraction pattern yields a virtual image of the sample.

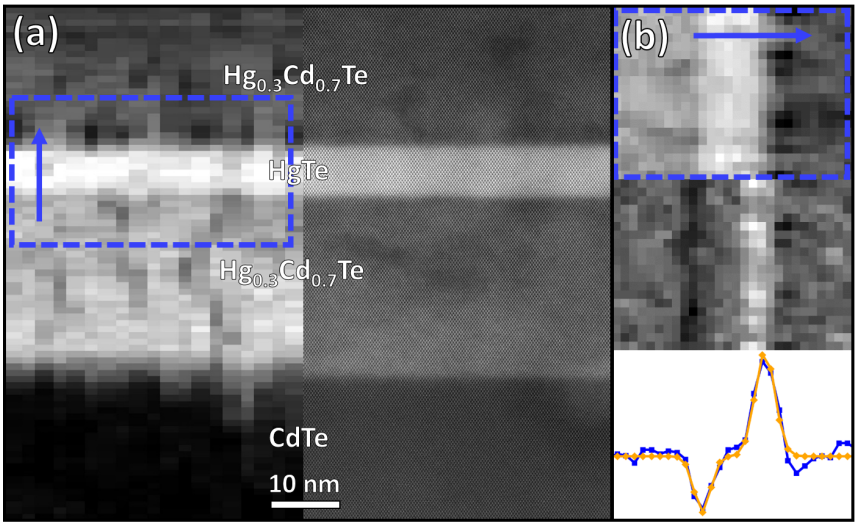

Figure 3.15: Example of how to determine the spatial resolution of an NPED series of HgTe/HgCdTe: a comparison of VHAADF and conventional HR-HAADF image of a similar region is shown in (a) on the left-hand and right-hand side, respectively. A zoom of the VHAADF (rotated to the right) with numerical derivative in growth direction below and line profile (blue) with Gaussian fits (orange) at the bottom is depicted in (b). A full analysis of the material system is presented in Sec. 4.3.

The drawback of virtual images is that the diffraction patterns are by definition from the part of reciprocal space which is dominated by coherent effects (namely diffraction). This is very different from HAADF imaging where the incoherent high-angle scattering is detected, thus creating incoherent images that are dominated by chemical contrast and not by strain or other coherence related artifacts. HAADF and different virtual images

are compared in Fig. 3.14. Image (a) shows one NPED pattern from a series of 50x50 images of an AlN/GaN sample in [0001] ZA. A virtual bright field (VBF) integrating all intensity within the direct beam is shown in (b) and a virtual dark field (VDF) integrating the intensity outside the big white circle is given in (b). Compared to a conventional HAADF of a similar region, depicted in (g), the virtual images look less 'clean'.

A different kind of virtual image will be called virtual high-angle annular dark field (VHAADF) and is shown in (d). Due to a patent being filed, the method of obtaining it cannot be discussed. This image is much more like a conventional HAADF and it is useful to determine the spatial resolution of the NPED series.

To facilitate robust and comparable measurements of interface widths, the following description of the change of intensity across interfaces is used: The function describing the intensity depending on the position perpendicular to the interfaces, I(x), is assumed to be a convolution between a Heaviside step function H(x), representing a perfectly sharp interface, and a function G(x) (the broadening) with a scaling factor for the intensity C_0 and an intensity offset A_0:

$$I(x) = C_0\, H(x) \otimes G(x) + A_0 \tag{3.15}$$

Therefore, calculating the derivative of Eq. 3.15 yields

$$I'(x) = \frac{d}{dx}(C_0 H(x) \otimes G(x)) = C_0 \frac{dH(x)}{dx} \otimes G(x) = C_0 \delta(x) \otimes G(x) = C_0 G(x) \tag{3.16}$$

where $\delta(x)$ denotes the Dirac delta distribution. Thus, when calculating the derivative of the intensity function it gives G(x) multiplied with the scaling factor C_0. When determining the standard deviation σ of I'(x) the result is therefore the same as σ of G(x).

G(x) is assumed to be a Gaussian function (which fits the experimental data of the case investigated in Sec. 4.3 quite well). For the sake of simplicity the interface width shall be defined as the FWHM of G(x) (2.35σ for a Gaussian function), which is also a common definition of beam size.

Fig. 3.15 (a) depicts a comparison of a VHAADF and a conventional HR-HAADF of the topological insulator HgTe/HgCdTe on CdTe substrate in [110] ZA. A zoom to the HgTe/HgCdTe interfaces rotated to the right is depicted in (b). Below, the numerical derivative perpendicular to the interfaces is shown and a comparison of the experimental data (blue) with a Gaussian fit (orange) is given. Subtracting the interface width from

HR-HAADF images from the width of the interfaces obtained from NPED via this method yields the spatial resolution of the NPED data.
In this example a beam width of about 1.8 nm is found, while measuring the beam size after traversing the whole sample should overestimate the width of the beam. Although this difference should be rather small, it can become important when not only the value of strain but also the sharpness of gradients is crucial. A full analysis of a material system where this is critical for the performance is given in Sec. 4.3.

3.2 Quantification of Contrast in STEM

In this chapter, the quantification of contrasts in STEM images is discussed. First, the case of incoherent imaging in the form of HAADF-STEM is investigated. Here, the important steps to facilitate the quantification of intensities that have been described in the literature by different groups are summarized. Afterwards, a method to measure the DQE of a scintillator based ADF detector and a way to determine the beam current without any special knowledge of it is demonstrated. In the second part the quantification of intensities in ABF is discussed, determining limitations and possibilities of quantifying these partly coherent STEM images.

3.2.1 Quantitative High-Angle Annular Dark Field

Obtaining chemical information from high-angle scattering has several limitations, but also advantages. Due to the one-dimensionality of the signal compared to spectroscopy, the analysis is restricted to specific systems where only one composition may change (or two that are linked). It is generally not possible to distinguish between an unexpected element being present and a variation in the expected element(s). In addition, the thickness plays a critical role, and therefore uneven regions can pose a problem. The strong points are the relatively low dose needed compared to spectroscopy (due to the fact that inelastic events are rare), and the obtainable compositional and spatial resolution. Although atomic resolution spectroscopy is widespread nowadays, it is significantly easier to produce high-resolution composition maps from HAADF. This is due to the fact that the HAADF signal stems from very localized scattering (cf. Sec. 2.4) in contrast to inelastic scattering, for which the delocalization of the interaction can pose a problem. The quantification procedure explained in this chapter is mainly based on the articles from LeBeau & Stemmer [87, 88] and Rosenauer et al. [36]. Generally, the procedure is not very complicated, but it is necessary to execute every step carefully and not to change any parameters in between measuring them and performing the experiment. The necessary steps are:

1) Determining all relevant experimental parameters
2) Setting up correct brightness/contrast settings and acquiring a detector scan
3) Simulation of electron scattering using frozen phonons
4) Performing the measurement
5) Quantification of experimental data by comparison with simulation

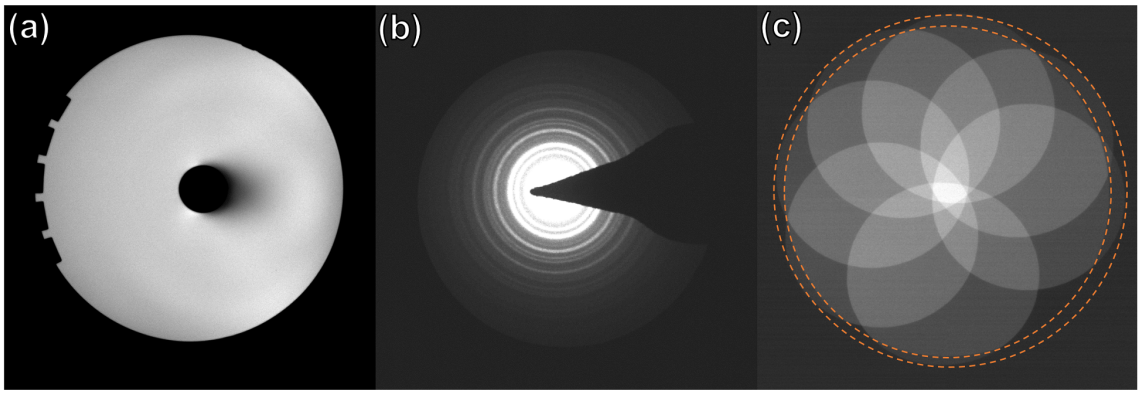

Figure 3.16: (a) Detector scan showing the physical size of the scintillator. To calibrate the inner detector angle the shadow has to be calibrated, e.g. with a known diffraction pattern (b) and the offset between shadow and detecting area has to be taken into account. This is demonstrated in (c) where the inner circle describes the shadow of the detector and the outer circle the beginning of the detecting area.

To quantify a scattering signal by comparing it to simulations, it is useful to normalize the signal to express it in fractions of the incoming intensity. Here, the experimental HAADF intensity I_{exp} is corrected for the vacuum offset I_{off} and normalized to the interval [0,1] by dividing it by the incoming beam intensity I_0 (also offset corrected):

$$I_{rel} = \frac{I_{exp} - I_{off}}{I_0 - I_{off}} \ . \tag{3.17}$$

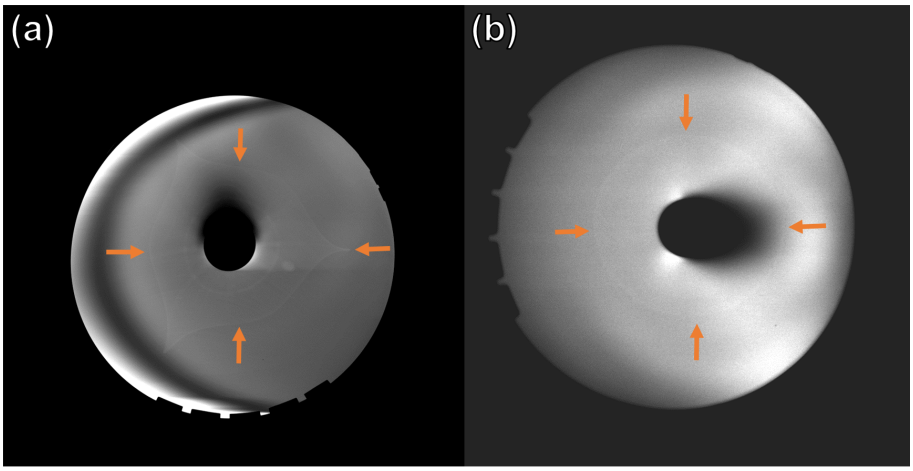

Figure 3.17: After leaving an intense probe scatter from a sample onto the detector for several minutes, a long-lasting afterglow of the beam is visible in the detector scans. The difference between an objective lens corrected microscope (a) and one without image corrector (b) is striking.

First, all important parameters have to be determined. The convergence angle can be inferred by comparing the size of the beam in diffraction space to a diffraction pattern

of a known material (making the beam parallel by changing the excitation of the last condenser lens yields a sharp diffraction pattern in just a few seconds). The detector can be imaged by scanning the probe across it in image mode, and an example of the result is shown in Fig. 3.16 (a). To determine what angle the inner edge of the detector corresponds to, the shadow it casts in diffraction space can be compared to a known diffraction pattern, as shown in (b) (or to the calibrated beam). This is not equivalent to the inner detector angle, as the detecting area is smaller than the physical size of the detector. To determine the offset between the physical edge and the onset of the scintillator, the beam can be shifted in the diffraction plane until the signal of the STEM detector increases. Acquiring images of the (partly shadowed) beam for different shift directions yields the sensitive edge of the detector (outer edges of the beams) and the physical edge of the detector (cut-off of the beams). A summation of the different beam positions with detector inserted and retracted each time is depicted in (c) and the shadow and sensitive areas are determined (orange circles). The offset was measured for different detectors in between 8 % and 15 % and the two circles are not (necessarily) centrosymmetric, which is attributed to a tilt of the detector plane relative to the optic axis. This means that centering the beam inside the shadow does not imply that the beam is centered inside the detecting area. It is imperative to deactivate descan during the detector scan, as descan's role is exactly to keep the beam stationary in the image plane while scanning, thus rendering any effort to image the detector futile.

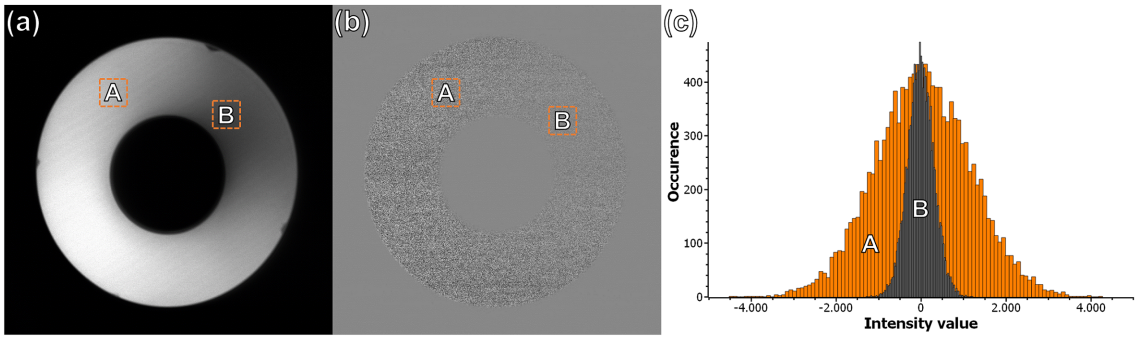

Figure 3.18: Detector scan (a) and the result of subtracting two detector scans (b). Histograms for the areas marked 'A' and 'B' in (b) are shown in (c). The relationship between signal and noise allows for the determination of the DQE and the beam current.

The next crucial parameter is the outer detection angle. For most HAADF detectors the ratio of outer to inner detector angle, as measured from a detector scan, is relatively large (>5) leading to outer detector angles of several hundred mrad when the inner angle is chosen for HAADF conditions. However, the detector is in reality not fully illuminated as the beam angle is at least limited by the acceptance angle of the objective lens (it might be more limited by other parts, like differential pumping apertures). This

acceptance angle is typically on the order of 10 degrees (175 mrad). To determine the cut-off angle, a probe with high beam current is kept stationary on a strongly scattering sample for some minutes. The intense illumination leads to a slight change in sensitivity of the detector (enhanced conversion rate) and a subsequent detector scan reveals the scattered beam, as shown in Fig. 3.17. The result for the utilized Titan^3 Ultimate with probe and image corrector and the Titan Themis with only a probe corrector is depicted in (a) and (b), respectively. A striking difference between the round cut-off of the Themis (at 191 mrad for the used camera length) and the complicated shape for the Ultimate is observed. This effect from the image corrector is discussed in detail by Krause et al. [89].

To compare the experimental and simulated results, the angular-dependent detector sensitivity has to be taken into account. To do so, a detector scan for the beam current and dwell time used in the experiment is performed with contrast and brightness set as not to clip any intensity and remain in the linear regime of detector response. Krause et al. [89] propose a better way to this scan by tilting the beam in diffraction mode instead of scanning it in imaging mode and therefore accounting for all distortions that originate from the image corrector. Here, instead of doing so for the double corrected Ultimate, the only probe corrected Themis is used for intensity quantification with 'classical' detector scans.

The next step is the simulation of the scattering signal depending on sample thickness and composition. Details concerning the different ways to simulate electron scattering are given in Sec. 2.4. The method used here are multislice frozen phonon simulations by means of Rosenauer's STEMsim software [52], kindly provided in the framework of a collaboration. Absorptive potential simulations, that are computationally less demanding, generally show already larger discrepancies compared to frozen phonons after a few ten nanometers [54, 53] and are therefore unsuitable. STEMsim can output the angular-resolved scattering for each scan point and thickness value which allows for a convenient application of detector sensitivity.

After performing the experiment with the determined parameters, the intensity is normalized according to Eq. 3.17 and compared to the scattering intensities from the simulation after taking into account the detector scan. The quantity I_0 is the average intensity of the detector scan to which it is also normalized before applying it to the simulation. For high-resolution images the exact intensity distribution is difficult to determine [37], but using a Voronoi tessellation in which all intensities that are closest to a given column are attributed to it and averaging this intensity leads to a robust evaluation method of HR-STEM data [90].

An example of the quantification of HAADF intensities to obtain composition maps is given in Sec. 4.4.

In Sec. 2.2 it is claimed that the scintillator type ADF detector has a DQE of > 0.9 and subsequently a perfect transmission of the incoming SNR is approximated. To validate this assumption a method is established to determine the DQE. Fig. 3.18 (a) depicts a detector scan with typical drop in intensity opposite the light pipe. The experimentally measured intensity I in a given pixel can be described in terms of the amount of incoming electrons N as

$$I = N\,\overline{n}\,\zeta\ . \tag{3.18}$$

where $\overline{n}$ is the quantity introduced in Sec. 2.2 and ζ comprises the following conversion into a digital signal. To repeat what is stated in Sec. 2.2, $\overline{n}$ accounts for the conversion rate of electrons to photons at the scintillator, the probability of a generated photon to make it to the PMT and the conversion rate of the photocathode. Thus, ζ comprises for the amplification factor of photoelectrons in the PMT and the conversion into a digital value, or expressed in a different manner how many gray levels one photoelectron causes. For a detector scan $\overline{N}$ is constant and N fluctuates only due to shot noise. The factor ζ is also constant as long as the contrast and brightness settings of the detector are not changed (and it is assumed not to fluctuate, cf. Sec. 2.2). Only n is changing with position due to the different probability of generated photons to reach the PMT (mainly for geometric reasons).

Fig. 3.18 (b) is the result of subtracting a second detector scan from (a) with identical settings. When two detector scans are subtracted, only the noise remains. Obviously, not only the intensity varies in (a) but also the noise in (b). From the SNRs in different areas it is possible to determine the DQE. The signal can be obtained by averaging over a region in (a) as it is shown for two areas, called 'A' and 'B'. From the same areas in (b) the noise can be extracted as the standard deviation of the image regions. Histograms of the two regions in (b) are shown in (c). Qualitatively, the noise levels seem to corresponds to the intensity values but the quantitative relationship is determined by the DQE. To evaluate the SNRs correctly, it is necessary to account for the increase in noise from subtracting the two areas. For uncorrelated noise that follows a normal distribution, the noise level (the standard deviation) increases from subtracting (or adding) images with noise levels σ_a and σ_b as:

$$\sigma_{a-b} = \sqrt{\sigma_a^2 + \sigma_b^2}\ . \tag{3.19}$$

Therefore, the noise level σ_{a-b} in the resulting image (b) is larger by a factor of $\sqrt{2}$ compared to σ_a or σ_b. The SNR_{in} is identical for both areas and is just the square root of the average number of incoming electrons. The resulting SNR is different, because the DQE is not equal due to the fact that $\overline{n}$ is not the same for the two areas. To repeat what is stated in Sec. 2.2, $\overline{n}$ comprises the conversion rate of electrons to photons at the scintillator, the probability of a generated photon to make it to the PMT and the conversion rate of the photocathode. The main difference in $\overline{n}$ for the two areas, $\overline{n}_A$ and $\overline{n}_B$, should be the probability of generated photons to arrive at the photocathode, due to the different geometry (cf. dark area opposite to the light pipe). From combining Eq. 2.9, Eq. 2.11 and Eq. 2.8 we obtain for area A

$$SNR_{out,A} = \sqrt{DQE_A}\, SNR_{in} = \sqrt{\frac{\overline{n}_A}{\overline{n}_A + 1}}\, \sqrt{\overline{N}}\ . \tag{3.20}$$

The value for $SNR_{out,A}$ can be well determined by dividing the offset-corrected average intensity of region A in the detector scan (a) by the standard deviation of region A in the difference image (b), divided by $\sqrt{2}$. Dividing the measured SNRs of the two regions A and B we obtain

$$\frac{SNR_{out,A}}{SNR_{out,B}} = \frac{\sqrt{\frac{\overline{n}_A}{\overline{n}_A+1}}}{\sqrt{\frac{\overline{n}_B}{\overline{n}_B+1}}}\ , \tag{3.21}$$

which we can transform into

$$\overline{n}_A = \frac{\frac{\overline{n}_A}{\overline{n}_B} - \frac{SNR^2_{out,A}}{SNR^2_{out,B}}}{\frac{SNR^2_{out,A}}{SNR^2_{out,B}} - 1}\ . \tag{3.22}$$

The ratio $\frac{\overline{n}_A}{\overline{n}_B}$ is just the ratio of background corrected intensities $\frac{I_A}{I_B}$ because the detector settings are fixed and only $\overline{n}$, which is proportional to the output signal, is changing. The measured parameters are $I_A = 48307$, $I_B = 20523$, $\sigma_A = 1127$ and $\sigma_B = 499$. Here, the $\sqrt{2}$ factor is already taken into account. From the SNRs of 42.68 and 41.13 it is already obvious that the DQE is rather high because they are very similar despite the large difference in intensity. Plucking these values into Eq. 3.22 we obtain $\overline{n}_A = 14.8$ and $\overline{n}_B = 6.3$, and therefore $DQE_A = 0.94$ and $DQE_B = 0.86$. The knowledge of the DQE allows for the determination of the incoming SNR and therefore the beam current. 1938 electrons impinged on average during the 4 µs dwell time, yielding a beam current of 77.6 pA. This value is in decent agreement with the 70 pA screen reading (which is not very trustworthy). A more reliable comparison with a Faraday cup holder should

be performed. From the average intensity of the detector scan of 44149 the average conversion rate can be calculated to 13.5. Thus, the (average) DQE of the detector is 0.93 which means that the detector reduces the incoming SNR by less than 4 %. From the knowledge of $\overline{n}$, ζ can be calculated according to Eq. 3.18 to around 1.69. This method is based on a few approximations and it suffers from the amplification of experimental errors due to the form of Eq. 3.22, but it demonstrates that the DQE of a scintillator-based ADF detector is in fact so high that the deterioration of the SNR by the detector can typically be neglected.

3.2.2 Quantitative Annular Bright Field

Annular bright field (ABF) has first been suggested by Rose as a useful imaging mode [91] and was later demonstrated by Okunishi et al. [92] and Findlay et al. [93]. It uses an annular detector situated within the direct beam, where the outer angle typically corresponds to the convergence angle and the inner angle to about half of that. ABF is therefore equivalent to hollow-cone CTEM by means of the reciprocity theorem of electron microscopy. The advantage of ABF when compared to HAADF is that the contrast depends more linearly on the atomic number Z, which facilitates the visualization of light elements, especially in the presence of heavier atoms. The capability of ABF was impressively demonstrated by Findlay et al. [15] and Ishikawa et al. [94] by visualizing hydrogen atoms in VH_2 and YH_2, respectively.

In contrast to HAADF, ABF is not completely incoherent. The transfer function and therefore the contrast depends on the specific inner and outer detection angle but not very critically. Even for outer detection angles being twice the convergence angle, and therefore strictly speaking not (annular) bright field anymore, the contrast is still what is qualitatively expected from ABF [15]. TDS plays, especially for lighter atoms, only a minor role for the image contrast [60].
It is advantageous to acquire ABF and HAADF in parallel, because the HAADF image allows for an easier determination of the correct focus. Although the image contrast in ABF is more stable with defocus compared to BF-STEM or CTEM, it can reverse with defocus and it is easier to adjust the focus using the HAADF image. Generally, ABF is much more sensitive to tilts away from the zone axis and obtaining high quality ABF images means to fine tune the specimen orientation.

One goal of this thesis was to perform quantitative ABF experiments to obtain information about the Li distribution in Li_2MnO_3 layered oxide battery electrode material during

different phases of charging/discharging cycles. The material stores the Li in sheets that are sandwiched in between oxygen layers and which can be continuously depleted (although not completely) and refilled. For more general information on rechargeable Li batteries [95, 96] and more details on Li_2MnO_3 [97, 98, 99], the reader is referred to the literature.
Understanding the kinetics of the Li insertion and removal has the potential to improve these batteries. Especially the influence of stacking faults (SFs), which are ubiquitous in this material [100], on the Li mobility is not known. The advantage of ABF is that it requires only a fraction of the dose that is necessary for spectroscopy experiments. Due to the pronounced sensitivity to electron irradiation of the material, spectroscopy experiments are problematic.
This work was performed with Adrien Boulineau from CEA-LITEN Grenoble who supervised the project and helped to synthesize, cycle and prepare the samples for microscopy. The material is sensitive to oxygen and humidity and it is therefore never exposed to air. This is facilitated by utilizing a glove box for the preparation process and a Gatan vacuum transfer holder to keep the specimen constantly shielded from environmental conditions from inside the glove box to within the microscope column.

Fig. 3.19 shows experimental data and simulation results for Li_2MnO_3 in two different zone axes. The convergence angle is 21 mrad, the high tension 200 kV and the detection angle is from 9 mrad to 23 mrad. Images (a) and (e) show the layered oxide crystal imaged in [010] and [100] ZA, respectively. For both directions the layers run vertically, alternating between layers of Li (green), O (blue) and a layer that consists of Mn (purple) and Li columns. In (a) they are separated, in (e) the purple columns consist of 2/3 Mn and 1/3 Li. Averages from TeMA are displayed in (b) and (f) and corresponding simulations in (c) and (g). While all columns are visible and a qualitative agreement is obtained, the quantification meets some serious obstacles. Thickness dependent intensity values for the two zone axes are shown in (d) and (h), respectively. The color of the graphs corresponds to the atoms in the columns and the dots indicate peak intensity values while the squares represent the average intensity within a box around the peak.
For the first tens of nanometers the signal oscillates, demonstrating the partly coherence of the ABF signal. The oscillation period is shorter for heavier elements, as expected from channeling theory. A monotonous behavior of the intensity is only given until around 10 nm. For thickness values above 50 nm the signal oscillations have more or less disappeared, but the slope is very small, which makes it difficult to detect differences in Li column occupation. This finding is consistent with simulations of ABF signals for other materials (BN, TiO_2, $SrTiO_3$) [60], which showed a similar behavior.

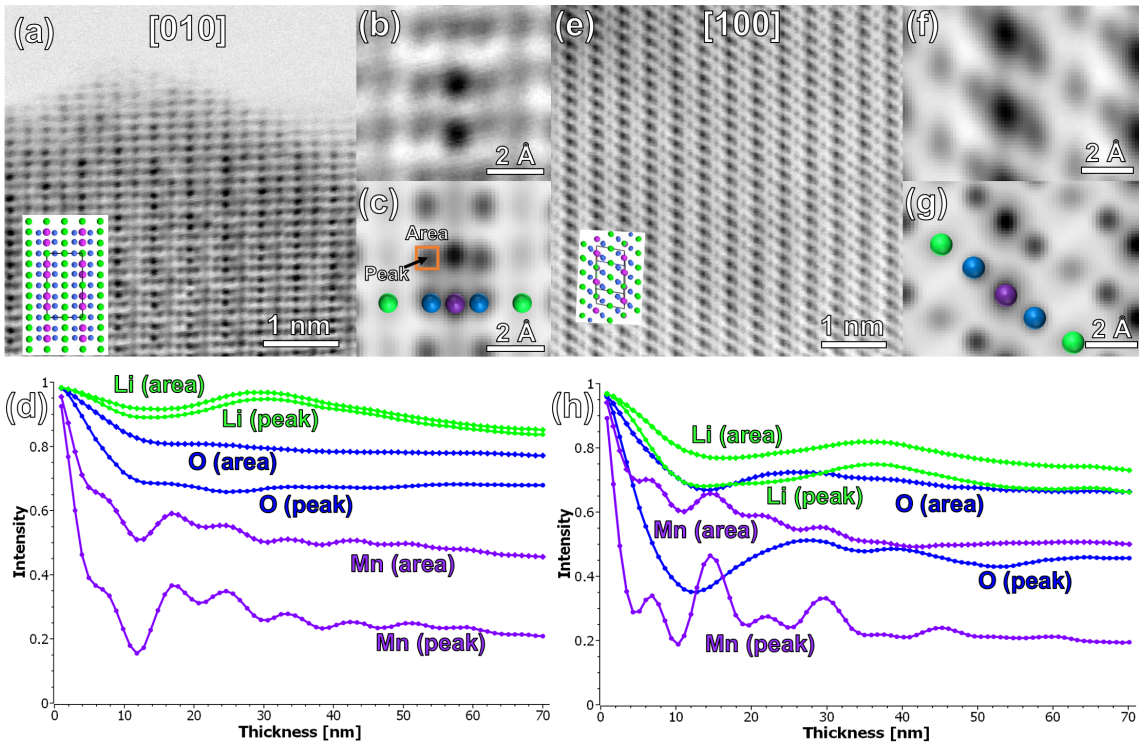

Figure 3.19: Experimental ABF images of Li_2MnO_3 in [010] ZA (a) and [100] ZA (e). The visualization of Mn (purple), O (blue) and Li (green) columns is qualitatively in agreement between the experiments in (b) and (f) and corresponding simulations (c) and (g). However, the variation of intensity with increasing thickness shown in (d) and (h) renders a quantification problematic. Green indicates Li, blue O and purple Mn. The peak values from simulation are compared to area averages as indicated in (c).

Unfortunately, typical Li_2MnO_3 particles used in batteries are on the order of 50 nm in size (with rather stark variations). The fragility of the particles and the resulting care that needs to be taken when handling them renders it rather impossible to thin them without significantly altering the material. Another problem is that a few percent of Mn atoms are disordered, already initially and more so after cycling, and some are located at the Li column positions (cf. dark contrast at Li positions in the thin regions of (a) and the overall too high contrast of the Li columns). Therefore, a quantification of the ABF signal for this complex material seems not practical.

Nevertheless, the contrast between the columns never reverses, meaning that the heavier element always shows the darker contrast and can thereby be identified. This result is also in agreement with simulations for other materials (BN, TiO_2, $SrTiO_3$) [60]. For higher thicknesses, the contrast barely depends on the thickness, rendering it even more robust. Therefore, ABF can be very useful to determine complex structures containing light elements. An experimental result that also shows the stability of the relative contrast for GaN is depicted in Fig. 3.20. Here, a thin GaN crystal in [11$\bar{2}$0] ZA with strongly varying

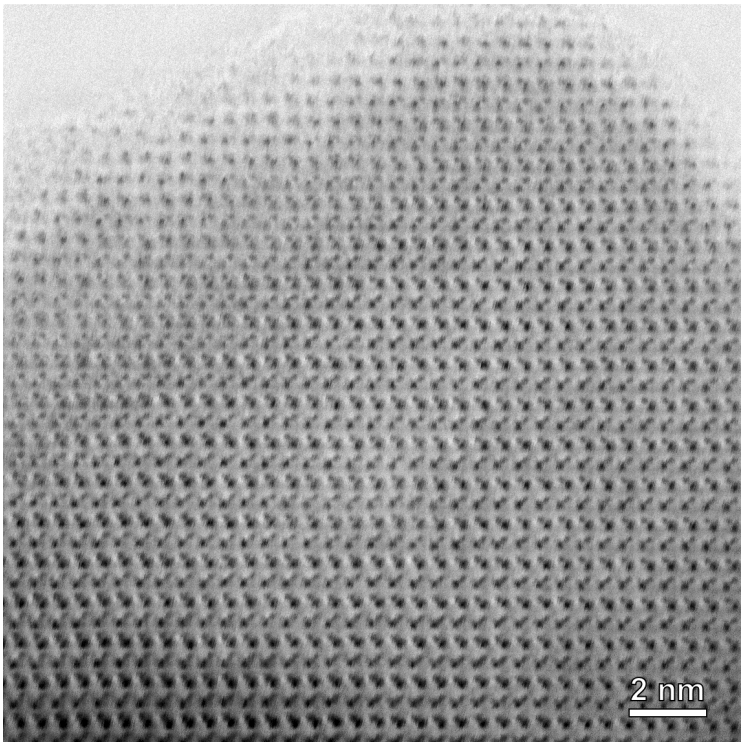

Figure 3.20: HR-ABF image of GaN crystal in [11$\bar{2}$0] ZA. Although the thickness varies strongly in the image, the relative contrast of Ga columns (dark) and N columns (lighter) does not reverse.

thickness over the FOV is imaged. Although the intensities of the atom columns changes drastically with thickness, the contrast never reverses, despite the partly coherent ABF. Especially for larger thicknesses, the attribution of elements to contrasts is unambiguous and this is used in Sec. 4.6, where the structure of core-shell inversion domains in GaN NWs is established with the help of ABF experiments and simulations. Generally, for systems in which the occupation of crystallographic sites with different elements needs to be determined (and no voids are to be expected), quantitative ABF seems promising.

3.3 Measuring Electric Fields in STEM

In this section the measurement of electric (and magnetic) fields by means of STEM is explained. To better understand the particularities of the scanning based methods presented here, first plane-wave based field measurements in the form of electron holography are elucidated. Afterwards, two techniques based on scanning focused probes are explained. The first section deals with differential phase contrast and shows its capabilities and limitations. Here, electron holography is also used experimentally as a well established reference method to compare it directly to DPC. In the second section, field mapping based on precession electron diffraction is introduced as a new method and its superior characteristics are demonstrated and explained.

Electric and magnetic fields have been observed in TEM by means of electron holography for more than twenty years (see e.g. review articles from Lichte et al. [101] and McCartney et al. [102]). Electron holography uses plane wave illumination on the sample and detects relative phase shifts of the wave from interference. There are many different ways to do so, but it has no influence on the following discussion and thus will be omitted for the sake of generality. A sketch for the case of off-axis electron holography is shown in 3.21 (a).

The changes in phase of the electron wave due to electromagnetic interaction can be written as

$$\phi(\mathbf{R}) = \frac{e}{\hbar v}\int_{-\infty}^{+\infty} V(\mathbf{R}+z\mathbf{e}_z)\,dz - \frac{e}{\hbar}\int_{-\infty}^{+\infty} \mathbf{A}(\mathbf{R}+z\mathbf{e}_z)\cdot\mathbf{e}_z\,dz \tag{3.23}$$

where $\mathbf{e}_z$ is the propagation direction of the beam, $\mathbf{R}$ is a position vector perpendicular to it, $V(\mathbf{R})$ is the electrostatic potential, $\mathbf{A}(\mathbf{R})$ the vector potential, v is the relativistic electron velocity and e the elementary charge [103].

Obviously, the first term describes the electrostatic part of the phase shift, while the second term is due to magnetic interaction. The electrostatic phase shift is proportional to the (projected) electrostatic potential in beam direction and the magnetic phase shift is proportional to the (projected) component of the vector potential in beam direction.

To obtain the E-field or B-field from the measured potentials, a differentiation is needed in both cases:

$$\mathbf{E}(\mathbf{r}) = -\nabla V(\mathbf{r})\ , \tag{3.24}$$

$$\mathbf{B}(\mathbf{r}) = -\nabla \times \mathbf{A}(\mathbf{r}) \ . \tag{3.25}$$

It can be concluded that the measured signal from electromagnetic interaction is proportional to the potentials (electrostatic and vector potential). E-fields and B-fields can be determined only indirectly by means of numerical differentiation of the experimental data.

A way to measure fields in the electron microscope by means of a scanning probe is differential phase contrast (DPC). It is also a rather old technique [104] that has recently gained substantial momentum [105, 106, 107, 108].
DPC is different in that it is performed using a convergent beam on the sample and detecting for each probe position a shift of the direct beam disk in reciprocal space. The basic idea is that with a segmented STEM detector in the diffraction plane it is possible to distinguish between a change of intensity on the whole detector and a shift of the beam (that manifests in a difference signal between the segments). Thus, not only amplitude modulation but also phase shifts can be visualized. The setup of DPC is sketched in 3.21 (b).

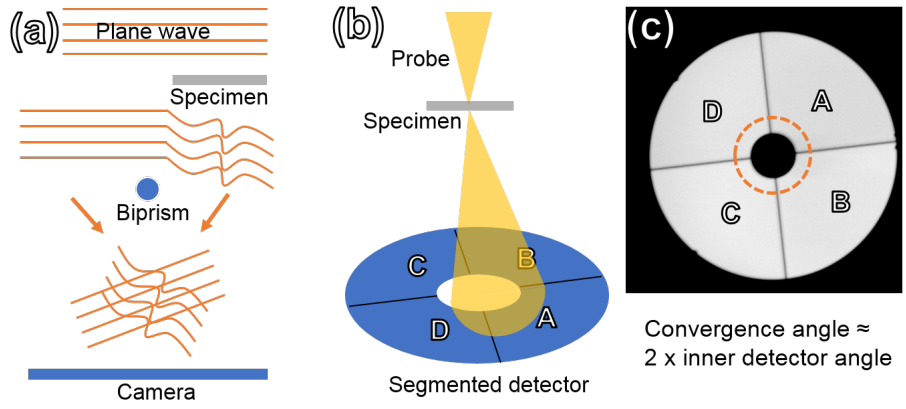

Figure 3.21: Experimental setup of (a) holography (here: off-axis holography) where the interference between a reference wave and the phase-shifted object wave is recorded and (b) DPC that determines the deflection of the beam in the sample by means of a segmented detector. The typical size of the convergence angle relative to the detector that is used in this chapter is sketched in (c).

In a simple, semi-classical model the beam is deflected by electric or magnetic fields (components perpendicular to the beam). This change of angle of the beam in real space is equivalent to a shift of the beam disc in reciprocal space. Thus, detecting beam shifts at the detector plane from difference signals of the detector segments yields information about the E-field or B-field components perpendicular to the beam integrated over the beam path.

Müller et al. [24] have shown for small probes and very thin specimens that the center of mass of the intensity distribution in the diffraction plane corresponds to the expectation value of the momentum operator perpendicular to the beam direction. The resulting ronchigram in the presence of a field is far from a homogeneous disc that is shifted. Nevertheless, in the following section large probes (no high-resolution) and relatively thick specimens (around 100-300 nm) are investigated. Therefore, the shift of the diffraction disc is explained in a simple model. There are of course problems related to diffraction, which are elucidated in the first part of this chapter. In the second part a method is proposed that greatly reduces them.
Grieb et al. demonstrated that also the sample geometry can cause a differential phase signal if the surfaces are not planar [109]. This artifact needs to be considered in experiments.

The influence of electric and magnetic fields on the beam is explained in a semi-classical model and no scattering or energy loss of the beam is assumed as it would be the case for a beam deflected by a field in vacuum [23].
For the case of an electric field, the force acting perpendicularly on the electron beam is proportional to the field component perpendicular to the beam and the electron charge $-e$ and is therefore

$$\mathbf{F}_\perp(\mathbf{r}) = -e\,\mathbf{E}_\perp(\mathbf{r})\ . \tag{3.26}$$

In the framework of Newton's second law of motion this force $\mathbf{F}_\perp(\mathbf{r})$ can also be expressed in terms of an acceleration perpendicular to the beam direction $\mathbf{a}_\perp(\mathbf{r})$ and the relativistic mass of the electron m_e^* as

$$\mathbf{F}_\perp(\mathbf{r}) = \mathbf{a}_\perp(\mathbf{r})\,m_e^*\ . \tag{3.27}$$

The beam needs a time τ to traverse the field containing region of distance t (e.g. the sample thickness), which is given by the initial electron velocity v as

$$\tau = \frac{t}{v_0}\ . \tag{3.28}$$

Because the beam is only sensitive to the perpendicular field component projected along the beam direction over t, solely the average field strength can be determined. Therefore, no integrals will be used and instead the average values are used.
While traversing the distance t the electron picks up a velocity component $v_\perp$ perpendicular to v_0 that can be expressed as

$$v_\perp = -\frac{E_\perp \, e \, t}{m_e^* \, v_0} \ . \tag{3.29}$$

The deflection angle γ (the measured quantity) can be described in terms of the velocities as

$$\gamma = arctan(\frac{v_\perp}{v_0}) \approx \frac{v_\perp}{v_0} \ . \tag{3.30}$$

The last expression corresponds to the small angle approximation which holds very well for the deflections that normally stay (well) below 1 mrad for typical field strengths, sample thicknesses and electron energies.
Therefore, the magnitude of the electric field component perpendicular to the beam can be expressed as:

$$E_\perp = -\frac{\gamma \, m_e^* \, v_0^2}{e \, t} \tag{3.31}$$

For a given beam energy all the parameters are known, except for t (typically the thickness of the sample in which the field is confined) and γ (the beam deflection measured during the experiment). In the case of 200 kV beam energy (the one used for all field measurements described in this manuscript) Eq. 3.31 simplifies to

$$E_\perp = -\frac{\gamma}{t} \cdot 3.438 \cdot 10^5 V \ . \tag{3.32}$$

An expression for the B-field can be derived in a similar manner. As this thesis is focused on E-fields, the derivation is omitted and the reader referred to the literature [23]. The B-field can be expressed as

$$B_\perp = \frac{\gamma \, m_e^* \, v_0}{q \, t} \ . \tag{3.33}$$

For the same case of 200 kV beam energy Eq. 3.33 simplifies to:

$$E_\perp = -\frac{\gamma}{t} \cdot 1.649 \cdot 10^{-3} T \tag{3.34}$$

It should be noted that as vectors $\mathbf{E}_\perp$ is of course parallel to γ caused by an E-field and $\mathbf{B}_\perp$ is perpendicular to γ from a B-field. For an experiment it is important to first determine which direction in the diffraction plane corresponds to a given vector in the sample plane, due to the rotations caused by the electron lenses.
In conclusion, while plane wave based electron holography yields phase shifts (from interference) proportional to the projected potentials (electrostatic or vector), the convergent

beam based techniques measure the deflection of the beam for individual probe positions, which is proportional to the fields. Thus, the two are generally linked by a derivation operation, which will be demonstrated and discussed in the following.

3.3.1 Electric Fields from Differential Phase Contrast

In this section, DPC is discussed in terms of different convergence angles and their consequence for sensitivity and spatial resolution. A direct comparison of DPC and off-axis holography elucidates the relationship of the two techniques and allows for a quantitative analysis of their sensitivities. After comparing the two techniques, a way to obtain quantitative DPC results is explained.
The electron holography experiments were performed together with David Cooper from CEA-LETI Grenoble who actually did the main work and also provided the samples and set up the in-situ biased p-n junction.

Mode	HR-DPC	NB-DPC	LM-DPC
Convergence angle	24 mrad	2 mrad	0.2 mrad
Spatial resolution	< 0.1 nm	0.7 nm	7 nm
Camera length	0.11 m	1 m	12 m

Table 3.1: Settings and resulting spatial resolution for the DPC modes termed HR-DPC, NB-DPC and LM-DPC.

As described in the section above, DPC is based on the difference signal of a segmented STEM detector that is meant to yield the deflection angle of the beam. Recent publications concerning DPC can be roughly grouped into the three categories: high-resolution DPC (HR-DPC), low-mag DPC (LM-DPC) and nano-beam DPC (NB-DPC). For the high-resolution DPC the convergence angle allows for atomic resolution (typically around 20 mrad). An example is the article from Shibata et al. [106] where the authors demonstrate that the signal they obtain is a superposition of the microscopic fields from the positively charged atomic nuclei and any mesoscopic fields present in the sample. A second setting is LM-DPC where the convergence angle is very small. It can be realized in the low-magnification setting of a microscope, where the objective lens is (almost) switched off and therefore (almost) no field is present in the vicinity of the sample. This LM-DPC mode is therefore also useful to study magnetic materials. An example of this mode is the article from Shibata et al. [107] where the authors measure the field of a p-n junction using a convergence anle of 0.133 mrad. The third mode is called NB-DPC and is an intermediate setting, where convergence angle, resolution, camera length (and

therefore sensitivity, as is demonstrated below) are in between HR-DPC and LM-DPC. The paper from Lohr et al. [108] is an example for this setting, which is used to determine mesoscopic piezo-electric fields in InGaN quantum wells (QWs) in between GaN layers. A summary of the three modes with the settings used in this manuscript is given in Tab. 3.1.

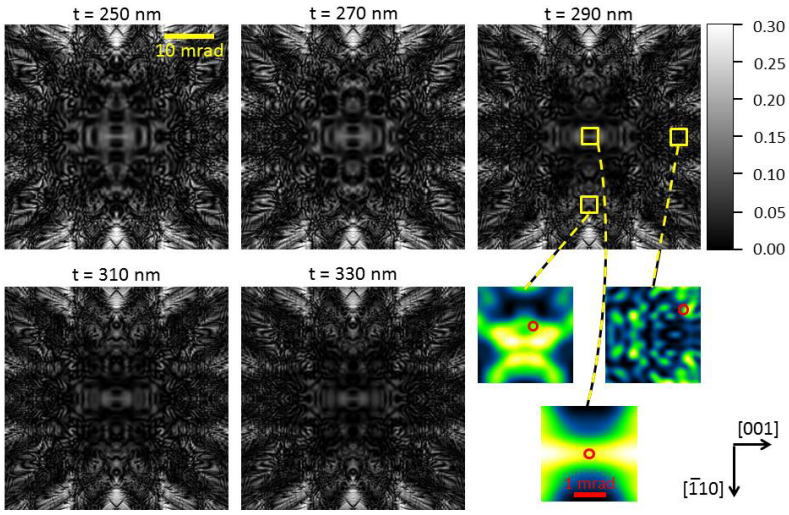

Figure 3.22: Channeling maps taken from [107] (suppl. information): Intensity for different thicknesses of a GaAs crystal in [110] ZA for an incident plane wave and a point detector depending on the tilt angle of the incident wave. The red circle denotes their convergence angle of 0.133 mrad. By tilting the specimen and using a small enough convergence angle, homogeneous disc intensity can be achieved.

For all settings a ratio of the convergence angle relative to the inner detector angle of around two is maintained (cf. Fig. 3.21 (c)), and therefore the camera length is changed according to the convergence angle setting. A smaller convergence angle would of course lead to a better contrast for a given shift. However, the reason to use a larger ratio is that the change in signal of the different segments depending on the deflection angle is more linear, especially when considering that the detector is not perfectly round and the beam not always ideally centered.
In this section mainly HR-DPC and LM-DPC are compared, being the two extremes. Nevertheless, NB-DPC is applied to a material in Chap. 4.

For the HR-DPC setting the diffracted discs are strongly overlapping with the direct beam disc. The influence of a local tilt of the crystal under investigation is the redistribution of intensities within the diffraction pattern, and therefore a contrast in the DPC. Thus, HR-DPC only works well when the whole sample region has the exact same orientation. In LM-DPC setting the convergence angle is so small that the diffraction discs are well outside the detector area. Nevertheless, artificial contrasts can arise through dynamic

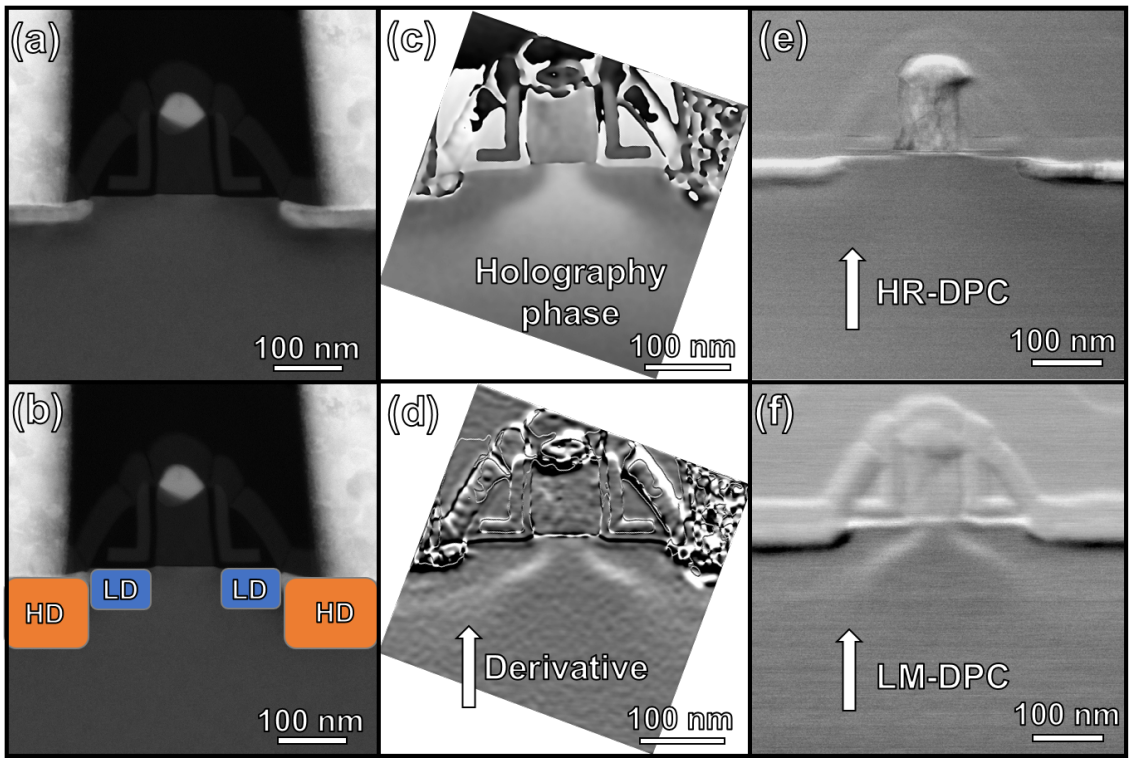

Figure 3.23: HAADF image of an 85 nm gate Si transistor (a) and sketch of the As dopant concentrations (HD: $2{\cdot}10^{20}$/cm^3, LD: $5{\cdot}10^{19}$/cm^3) in (b). An off-axis holography phase map is depicted in (c) which shows the different doping. DPC maps showing the vertical field component (indicated by an arrow) are given for the HR setting in (e) and the LM mode in (f). The vertical derivative of the holography data yields a similar result as the LM-DPC while the HR-DPC is not sensitive enough.

diffraction contours within the direct beam disc. An excellent investigation of this effect for the case of a GaAs crystal in [110] ZA was performed by Shibata et al. in the supplementary information of their article about DPC on a p-n junction [107] and their results are shown in Fig. 3.22. The channeling maps display intensity values depending on the sample tilt away from the ZA assuming an incoming plane wave and an on-axis point detector. For a small enough convergence angle (the red circle corresponds to their 0.133 mrad aperture) regions exist that exhibit homogeneous contrast. Therefore, by choosing a small convergence angle and tilting the sample a bit away from the ZA a homogeneous disc intensity and resulting clean DPC contrast can be achieved. This is in fact very similar to off-axis holography where the sample is tilted slightly away from ZA to reduce diffraction contrast (and the convergence angle of both techniques is similarly small). This condition can be obtained by tilting the sample while observing the DPC and visually reducing diffraction contrast. By doing so, one finds the flat areas from the channeling and this is used for all LM-DPC data shown here. The DPC images are acquired as 1024^2 px images with a frame time of 80s (dwell time around 64 µs) and a

beam current of 95 pA. The holograms are 2048^2 px images using 150 V biprism voltage and 8s exposure time.

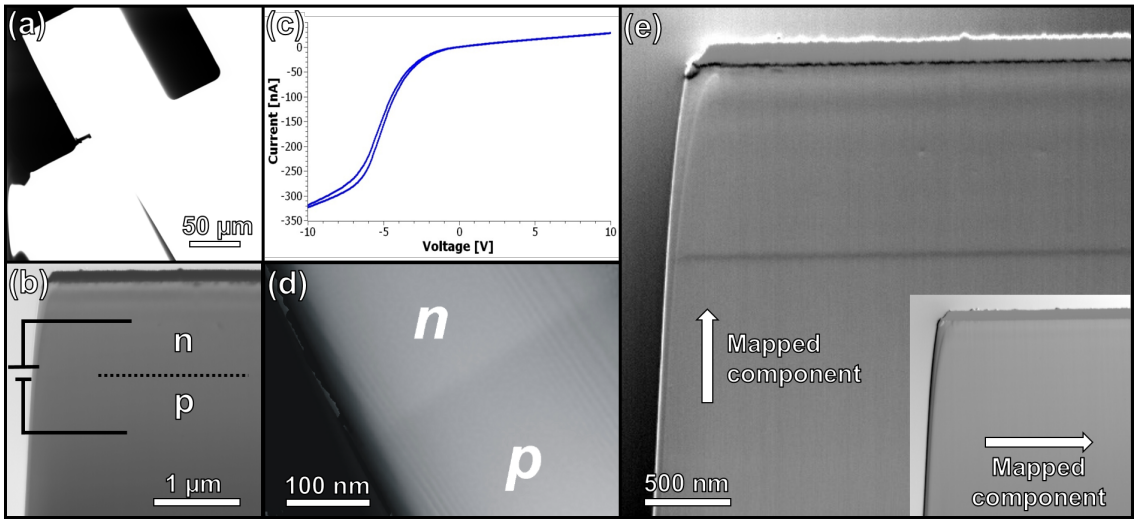

Figure 3.24: Setup of the in-situ biasing of a p-n junction (a) with the manipulator approaching the FIB lamella, imaged in CTEM. A schematic drawing of the applied bias overlaid to a STEM image of the junction is shown in (b). The Si is doped with $5{\cdot}10^{19}/\mathrm{cm}^3$ P and B atoms for the n and p regions, respectively. The I-V curve of the device is given in (c), exhibiting clear diode characteristics. A holography phase map for 0 V bias is shown in (d) and LM-DPC data for the field component perpendicular to the junction in (e) and parallel in the inset.

To illustrate the relationship between holography and DPC, they are both performed on the same Si transistor, shown in Fig. 3.23 (a), which exhibits a dopant profile sketched in (b). More information about the device can be found in Cooper et al. [110]. The corresponding off-axis holography phase map is shown in (c). Dopant distributions can be well observed from the change in potential of the sample. The HR-DPC map (vertical field component) given in (e) shows no contrast while the LM-DPC map depicted in (f) exhibits clear contours. When calculating the derivative of the holography phase, the same contours as for the LM-DPC are observed, as can be seen in (c). This makes sense as the electric field is, according to Eq. 3.24, proportional to the gradient of the potential and the DPC signal should be directly proportional to the beam deflection an therefore to the electric field itself according to Eq. 3.32. The HR-DPC is obviously not sensitive enough to detect the field. It should be noted that the numerical derivative amplifies the noise of the phase map, which can be well observed when comparing (c) and (d).

To directly compare the performance of holography and the two DPC modes for a tunable potential difference, a p-n junction is FIB prepared and in-situ biased utilizing a

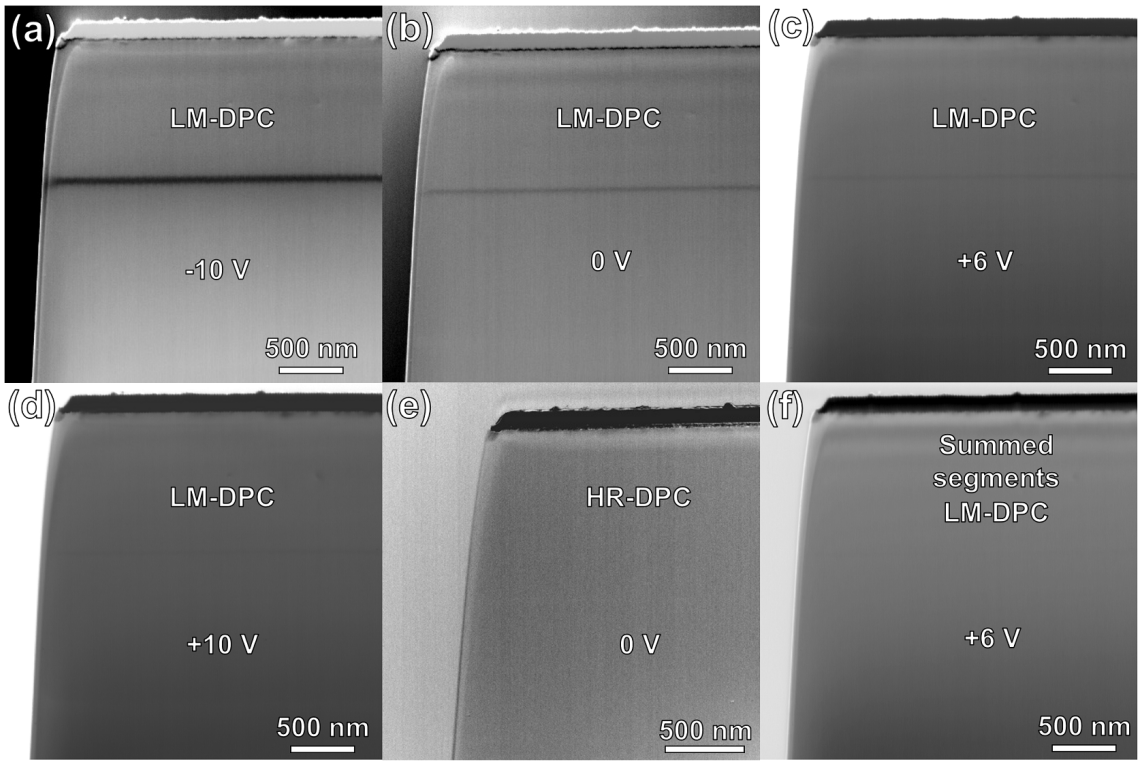

Figure 3.25: DPC on p-n junction for different bias voltages: LM-DPC data for 10 V reverse bias (a), without bias voltage (b), with 6 V forward bias (c) and 10 V forward bias (d). The HR-DPC setting is not sensitive enough to produce a visible contrast for 0 V bias (e). The sum of all segments for LM-DPC at +6 V is shown in (f). N.B.: Not only the strength of the field but also the width of the depletion layer varies with bias voltage, in qualitative agreement with theory.

Nanofactory holder. The experiment is depicted in Fig. 3.24. In the CTEM image (a) the manipulator needle can be seen approaching the lamella that is attached to a Cu grid. An overview STEM image is shown in (b) with a sketch of the n and p regions and the expected boundary. In (c) the I-V curve of the device measured in-situ is depicted, exhibiting a clear diode behavior with only a small leakage current in reverse bias direction and a sharp increase in current at the threshold voltage in forward bias direction. This test is vital to verify that the sample preparation procedure did not disturb the functionality of the device (e.g. short-circuiting). In (d) the potential map obtained from off-axis holography without applied bias is depicted. The vertical component of the electric field measured from LM-DPC is displayed in (e) and the horizontal component in the inset. It is obvious that the electric field perpendicular to the junction corresponds again (at least qualitatively) to the derivative of the phase map. The fact that no field is observed parallel to the junction underlines the proper behavior of DPC, at least for this case of a very homogeneous crystal. It should be noted that summing all four seg-

ments of the detector gives rise to an image that corresponds to a kind of ABF/ADF image from a non-segmented detector and the absence of contrast at the investigated region is generally also a good way to check for artifacts (demonstrated in Fig. 3.25 (f)).

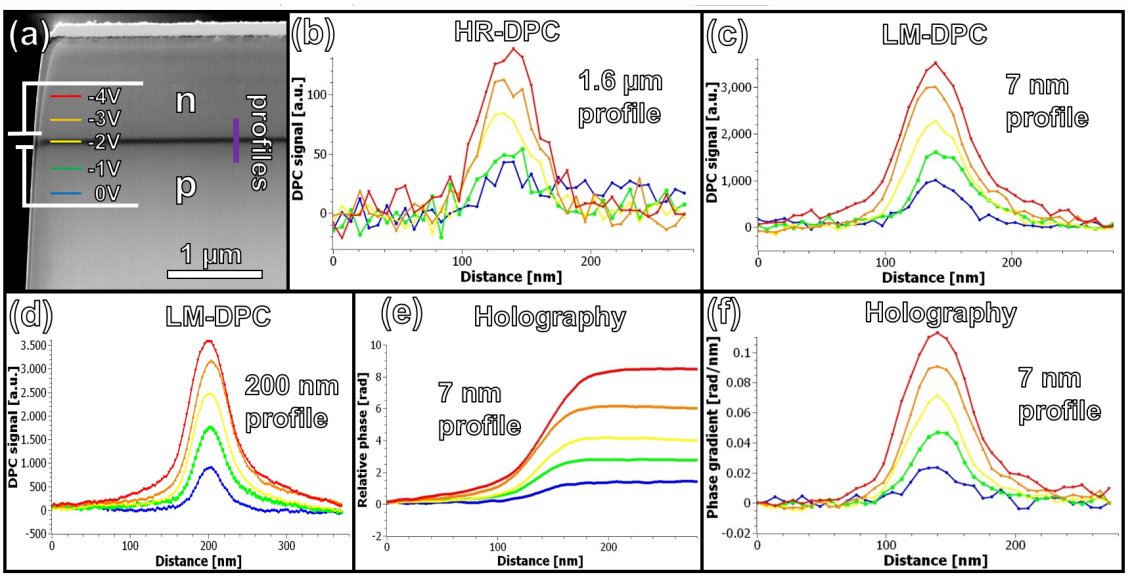

Figure 3.26: Line profiles for different reverse bias voltages applied to the junction as shown in (a): 1.6 µm wide profile for the HR-DPC setting (b), 7 nm wide profile for LM-DPC (c) and 200 nm wide profile for LM-DPC (d). The 7 nm wide profile of the holography phase is shown in (e) and the field obtained from numerical derivative is given in (f). Corresponding SNR values are summarized in Tab 3.2.

A visual comparison of the DPC signal (component perpendicular to the junction) for HR and LM settings is shown in Fig. 3.25. While for LM-DPC a clear contrast is observed even without biasing as depicted in (b), the HR-DPC in (e) does not exhibit a visible contrast (a very faint line can be seen if one knows where to look for, note the slightly different scale). The contrast for LM-DPC is greatly increased for a reverse bias of 10 V as shown in (a). More surprisingly, at 6 V and even 10 V forward bias a field at the junction is still visible although the threshold voltage has been passed (cf. Fig. 3.24 (c)) as depicted in (c) and (d), respectively. To exclude an artifact, the sum of all segments for (c) is depicted in (f): the junction is not visible. This underlines the sensitivity of LM-DPC. It should also be noted that not only the intensity of the field at the junction but also the width is visibly changing. At least for the case of reverse biasing, this is expected.

For a quantitative comparison of the methods, line profiles across the junction are displayed in Fig. 3.26 for different reverse biases. In (a) the setup is sketched with the applied voltages linked to the color of the graphs. The case of HR-DPC is shown in

Technique	**HR-DPC**	**LM-DPC**	**OA-Holography**
Resolution	< 0.1 nm	7 nm	7 nm
FOV	2.5x2.5 μm^2	2.9x2.9 μm^2	0.7x0.7 μm^2
SNR (-4 V bias, 7 nm profile)	0.6	45 (145 for equal FOV)	55 (470 for phase)
Frame time	80 s	80 s	8 s

Table 3.2: Comparison of HR-DPC and LM-DPC vs. off-axis holography for the performed experiments.

(b) with a profile width of 1.6 µm. It is necessary to average so much to obtain any signal discernible from the noise level. In (c) the LM-DPC signal is displayed for a 7 nm wide profile and in (d) for a 200 nm wide profile. The holography phase is displayed in (e) for a 7 nm wide profile, which corresponds to the spatial resolution defined by the aperture size of the reconstruction. Before calculating the derivative, the holography data is binned down to the same sampling as the DPC to make it more comparable. The resulting field profile from holography is given in (f).

A comparison of the three techniques including the SNR obtained from this analysis is displayed in Tab. 3.2. The SNR of LM-DPC and OA-Holography are comparable, but when taking the same FOV for the analysis (averaging over the same fraction of the image) LM-DPC is better. This is only true when determining electric fields, due to the reduced SNR of holography from the derivative. When investigating the holography phase maps a very high SNR is observed. It should also be taken into account that the exposure time of the holograms is only one tenth of the frame time used for DPC here. An advantage of DPC is that it irradiates the sample only locally with a beam current that is much lower than what is applied (although spread out) for holography. Therefore, it can be be assumed that DPC generally leads to less charging of the sample, which can be a problem in some cases for holography.

For cases where mesoscopic fields of narrow layer structures are to be measured, NB-DPC can be a good compromise between spatial resolution and sensitivity. An example for an $In_{0.15}Ga_{0.85}N$/GaN structure with 2.5 nm InGaN layers and 10 nm GaN barriers is shown in Fig. 3.27. The HAADF image in (a) depicts the layer stack and (b) shows the DPC signal perpendicular to the layers of an NB-DPC experiment with convergence angle of 2.2 mrad.

Although the tilt is optimized to reduce effects from dynamic scattering, strong contrasts can be observed on both sides of the layer stack from bending that is present due to the lattice mismatch of InGaN and strain relaxation from sample preparation. Even worse, when comparing a profile of (b) show in (d) with a field profile from off-axis holography

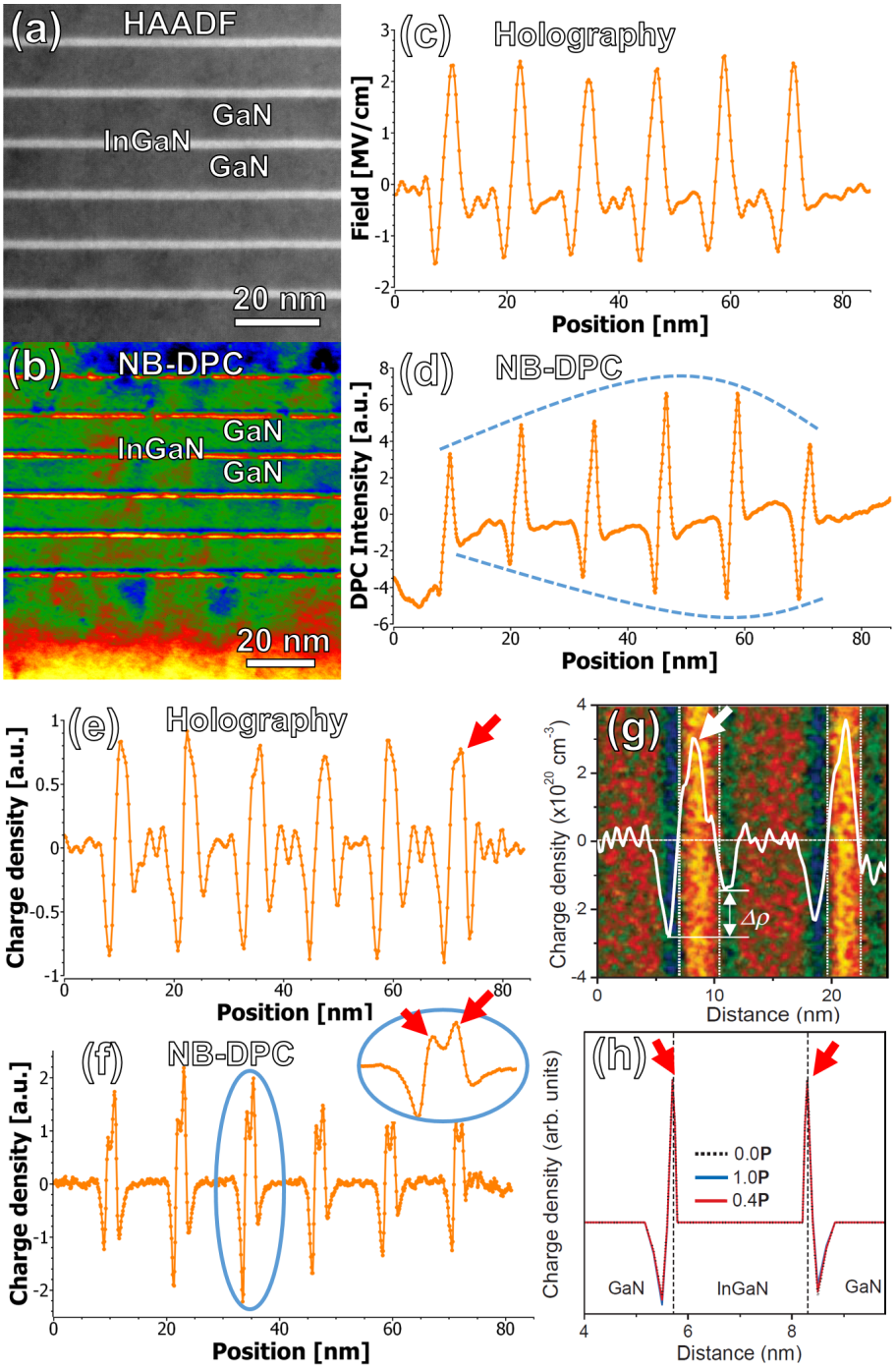

Figure 3.27: Comparison of NB-DPC and holography for an InGaN/GaN structure depicted in HAADF image (a). The DPC intensity perpendicular to the layers is given in (b) and a line profile for the whole width of the image in (d). When compared to the field determined from off-axis holography shown in (c) it becomes clear that diffraction contrast compromises the DPC. The charge density from holography is depicted in (e) and from DPC in (f) with a profile from in-line holography from Song et al. [111] in (g) and simulation results from the article in (h). NB-DPC is the only technique that resolves the double-peak structure of charge densities in the GaN layer.

(by calculating the derivative of the phase) given in (c) it can be seen that the bending also has an influence on the NB-DPC intensity within the layer stack (blue lines as a guide to the eye). When going back to the channeling maps shown in Fig. 3.22 from Shibata et al. [107] it becomes clear that for an aperture size of about 2 mrad and local crystal tilts on the same order of magnitude, dynamic diffraction effects cannot be avoided.

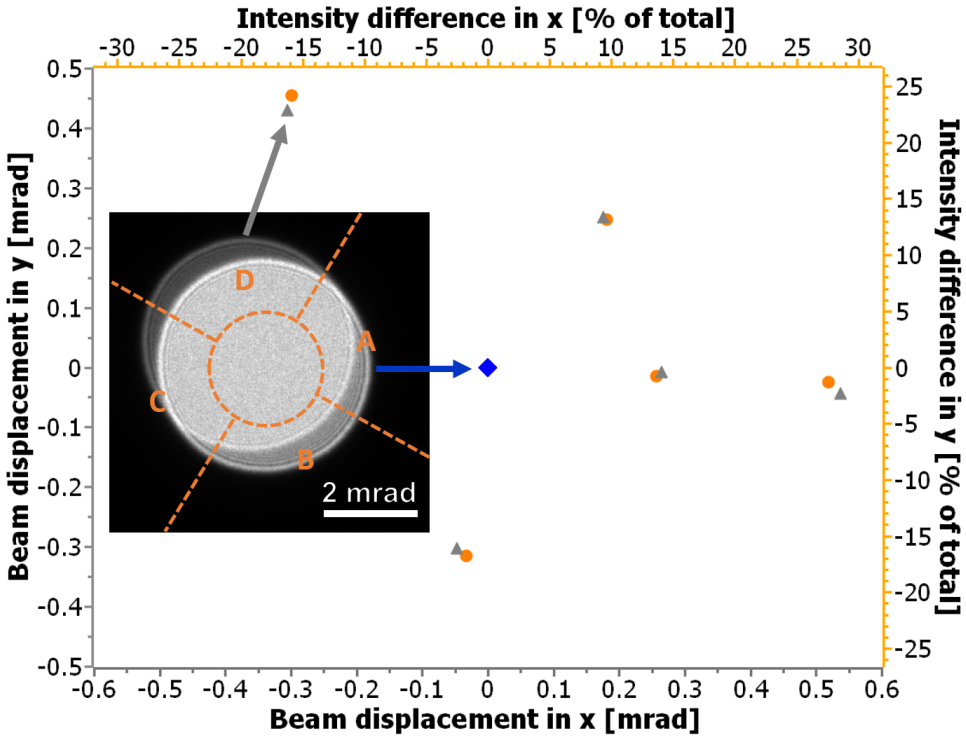

Figure 3.28: Check of the linearity of DPC in NB-DPC mode: Measured beam shifts in mrad (gray) and corresponding intensity differences in percent of the total intensity (orange). An image of the beam disc for the origin (blue) and one shifted position, together with the alignment of the detector is depicted in the inset. The intensity difference vectors are rotated to be aligned with the camera axes.

When calculating the numerical derivative of the field to obtain the charge density, the superior spatial resolution of NB-DPC becomes evident. Charge carrier density profiles for off-axis holography (e) and NB-DPC (f) are compared to in-line holography results from Suong et al. [111] in (g) and simulations from the article in (h). The analysis and calculation from Suong et al. are performed for a nominally identical sample (2.5 nm $In_{0.15}Ga_{0.85}N$ layers with 10 nm GaN barriers). The two charge density peaks predicted within the GaN layer (arrows) can only be resolved in NB-DPC.

However, the artifacts in DPC signals from dynamic diffraction pose a problem for samples that exhibit local crystal tilts or when larger convergence angles are needed to improve the spatial resolution. A new method for electric field mapping that uses a

nano-beam but eliminates dynamic diffraction effects is introduced in Sec. 3.3.2.

A way to quantify DPC data has been demonstrated by Lohr et al. [108] using a plate capacitor sample holder to measure the signal change depending on the applied field and thus calibrating the setup. Although the system sounds simple, great care has to be taken to ensure that the geometry really causes a given field and faulty calibrations happened with this system [112].

The method utilized here to calibrate the setup is to shift the beam relative to the detector using the diffraction shift coils and acquiring DPC in vacuum before and after the displacement, and also the positions of the diffraction disc on a camera. The intensity difference can be related to the induced shifts by comparing it before and after the beam is displacement with the shift vector that can be obtained from cross-correlating the recorded camera images. The result of such an experiment is given in Fig. 3.28. The original center position is defined as zero and marked in blue. Different shifts are induced utilizing the diffraction shift coils and they are marked in gray. First, the intensity of all segments is normalized by dividing it by the sum of all segments. For each position, the intensity difference of diagonal segments, e.g. between segments A and C as ΔI_{AC}, is determined and the value of the center position $\Delta I_{AC,0}$ is subtracted. The rotation between the detector segments and the camera plane can be calculated using the shifts in the two camera axes relative to the center position $shift_x$ and $shift_y$

$$\omega = arctan\left[\frac{(\Delta I_{AC} - \Delta I_{AC,0}) * shift_y - (\Delta I_{BD} - \Delta I_{BD,0}) * shift_x}{(\Delta I_{AC} - \Delta I_{AC,0}) * shift_x - (\Delta I_{BD} - \Delta I_{BD,0}) * shift_y}\right] . \tag{3.35}$$

Afterwards, the intensity differences can be calculated in the detector coordinate system as

$$\begin{pmatrix} \Delta I_x \\ \Delta I_y \end{pmatrix} = \begin{pmatrix} cos(-\omega) & -sin(-\omega) \\ sin(-\omega) & cos(-\omega) \end{pmatrix} \begin{pmatrix} \Delta I_{AC} \\ \Delta I_{BD} \end{pmatrix} . \tag{3.36}$$

This was also used for the DPC data in this section to account for a rotation of the detector segments relative to the sample geometry. If the convergence angle has been measured beforehand, the disc size on the camera directly yields the absolute deflection angle. Knowing the deflection angle from the intensity change of the DPC allows to calculate the electric field by means of Eq. 3.32 if the sample thickness is known. For a given set of parameters (camera length, convergence angle, contrast/brightness settings) the intensity difference is then calibrated relative to the beam shift. In a real experiment

it is important to account for the diminished intensity of the direct beam by normalizing the intensity of the segments as described above.

3.3.2 Electric Fields from Nano-Beam Precession Diffraction

Recently, field mapping from recorded STEM diffraction on a pixelated detector has been demonstrated [113, 24]. As a camera offers much more information than the four segments of a DPC detector, the non-uniform distribution of intensity in the diffraction plane can be better accounted for.

Here, a new method is presented that was developed in the course of this thesis and has been filed as a patent [114]: precession diffraction field and strain mapping. In addition to the measurement of disc spacings from precession electron diffraction data, as explained in Sec. 3.1.3, the movement of the central disc is tracked with high precision. This is already greatly improved by the precession, which leads to more homogeneous disc contours and intensities and which is the reason why NPED strain mapping has a better precision than NBED. The second improvement is that instead of measuring the beam position by its center-of-mass (COM), template-matching is performed for each frame with the template being the diffraction disc from a reference image. It yields more robust results than using a COM based algorithm.

This approach is valid because instead of using a high-resolution compatible beam that probes the microscopic field from the nuclei, leading to intensity distributions that are neither homogeneous nor contained in a disc (as shown by Müller et al. [24]), a probe about 1 nm in size is utilized. Thus, by irradiating several atomic planes the diffraction pattern resembles the structure of the crystal and only mesoscopic fields are measured. The influence of these should be reasonably described by the semi-classical theory explained above. The problem that dynamic scattering poses in the form of contours obscuring the geometry of the disc is counteracted by the precession. Kinematic diffraction has basically no influence because the method is based on finding shapes and is independent of relative intensities (as long as the SNR of the direct beam disc is sufficient). Even incoherent scattering does not distort the measurement (it may only reduce the precision but not the accuracy), because template-matching is used and not COM. This incoherent background is peaked at the center of the Laue zone and therefore moves when the crystal orientation changes. COM methods should produce severe artifacts when the crystal is not flat due to this effect. Thus, the tracking of the direct beam disc by means of template matching should be a valid approach and typical challenges encountered in experimental diffraction patterns should not change the outcome.

Another advantage of using template matching is a more robust behavior in the vicinities of interfaces; if the beam is mainly in one material but tails of the beam are in the other one, contrasts can arise in the diffraction pattern around the edges of the beam disc. These contrasts do not lead to a shift, as would be the case for center of mass based methods.
The robustness of the precession based method and the quality of the sub-pixel position determination allow for camera lengths that are small enough to capture diffraction discs together with the direct beam while being sensitive enough to the rather faint beam deflections induced by fields. The simultaneous mapping of strain and fields offers a unique way of characterizing piezoelectric materials in which the two are linked.

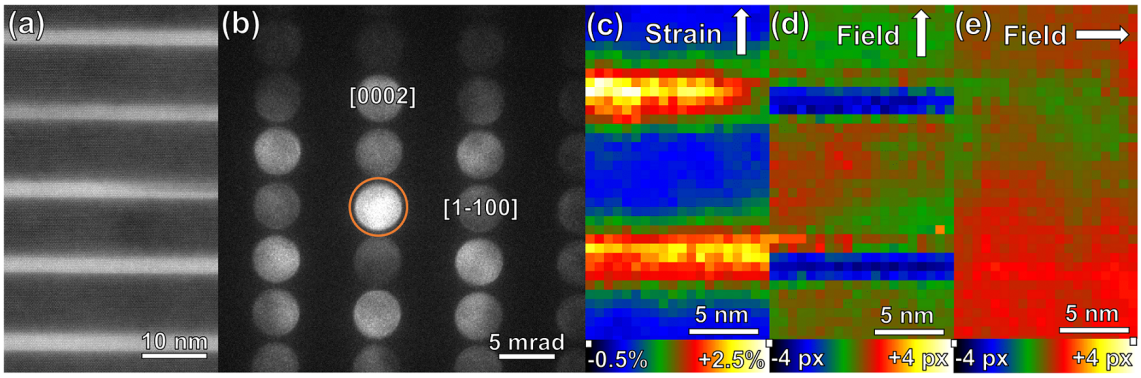

Figure 3.29: Example of the simultaneous field and strain mapping by NPED. A HR-HAADF overview image of the InGaN/GaN sample under scrutiny is shown in (a) and an indexed diffraction pattern of the NPED series in (b). The orange circle marks the central disc and indicates the area used for the template matching. The obtained strain component in growth direction across two QWs is mapped in (c) and the field related shifts of the central beam disc in horizontal and vertical directions are shown in (d) and (e), respectively.

A demonstration of the method is depicted in Fig. 3.29, where it is applied to an InGaN/GaN superlattice. HR-HAADF of the material stack in $[11\bar{2}0]$ ZA depicting the 2.5 nm $In_{0.15}Ga_{0.85}N$ QWs sandwiched in between 10 nm GaN layers is shown in (a). The sample is similar to the one showed in Sec. 3.3.1 but the layers are less homogeneous. One diffraction pattern from the NPED series is given in (b) with the orange circle marking the region around the central disc that is used as the template. The strain obtained from the distance of diffraction discs is depicted in (c) and the shift of the central diffraction disc perpendicular and parallel to the layers in (d) and (e), respectively. A relatively constant shift in growth direction of around 2.5 px is found inside the InGaN layers compared to the GaN barriers while the parallel shift shows only minor variations. Taking into account the sample thickness (CBED measurement showed 104 nm in the vicinity) the shift translates into a field value of around 3.9 MV/cm. The

standard deviation of field values in the GaN regions yields a precision of around 0.2 MV/cm.
An in-depth analysis of a material by means of this technique is described in Sec. 4.5.
Quantifying the shift signal is trivial, as the beam disc diameter corresponds to the convergence angle. But even if α is not measured, a calibration can be obtained from the diffraction pattern of a reference region, which makes the method very convenient. Then, the signal can be quantified according to Eq. 3.32 if the sample thickness is known.

Due to the precision of the beam tracking, artificial ramps in the beam deflection can be observed even if the pivot points are decently aligned, especially for larger FOVs. A way to remove this effect is to repeat the NPED acquisition in vacuum and to subtract the vacuum disc positions from the ones obtained for the specimen.

4 | Applications in Materials Science

The goal of the development of novel (S)TEM techniques should be to provide new tools for the exploration of matter, and therefore this chapter is meant to demonstrate the capabilities of the techniques discussed before. To demonstrate the wide scope of these techniques, the characterization of strain, electric fields, chemistry and (3D) structure of materials covering photovoltaics, topological insulators, optoelectronic devices and transistors is demonstrated.

Synthesis or growth of the materials that are explored was not part of this thesis and each section starts with a paragraph naming and acknowledging the collaborators responsible for the design and creation of the material systems as well as sample preparation and other types of characterization if applicable.

4.1 Atomic Resolution Interface Chemistry in ZnTe/CdSe from Strain

The sample discussed in this section was grown by Régis André at CNRS/CEA Grenoble. A suitable thin-foil was prepared via small-angle cleavage by Bastien Bonef, who also performed the atom probe tomography (APT) characterization that is later on compared to the results obtained from strain analysis. The analysis presented in this section was also published in Journal of Microscopy [115] and Fig. 4.2 (a) was chosen as the cover image of the according issue.

ZnTe/CdSe super lattices exhibit a type-II band alignment that should allow for an effective spatial separation of generated charge carriers, making them an interesting system for photovoltaic applications [116]. The variation of the layer thicknesses and the number of periods can be used to tune the absorption of the system [117]. Due to the small lattice mismatch of ZnTe and CdSe (a=610.3pm and a=607.8pm, respectively)

high quality epitaxial layers can be grown. However, the chemistry at the interfaces is of utmost importance to optimize the absorption of the photovoltaic cell [117].

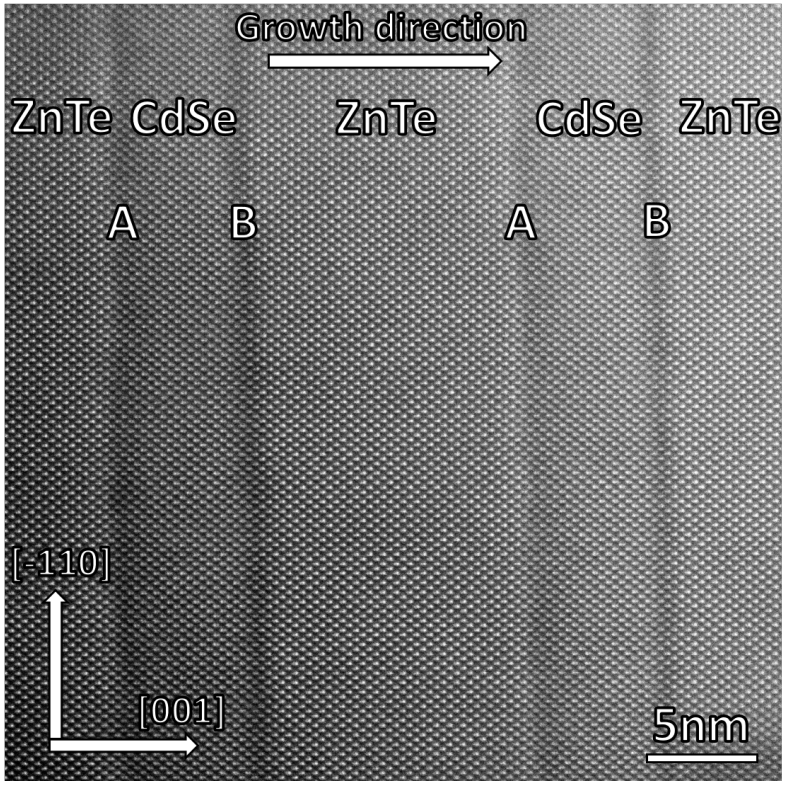

Figure 4.1: HAADF image of the ZnTe/CdSe superlattice.The excellent sample quality from cleavage (performed by Bastien Bonef) allows for decent high-resolution imaging over a rather large field of view. The interfaces from ZnTe to CdSe (in growth direction) are denoted 'A' and from CdSe to ZnTe 'B'.

The ZnTe/CdSe stack was grown by MBE on ZnTe (001) substrate with nominal thicknesses of 11nm for ZnTe and 8nm for CdSe. An excess of Zn was provided for the ZnTe layers and a Cd excess for the CdSe to prevent the formation of unfavorable ZnSe species at the interfaces that had been detected in previous studies without any precaution during the growth [118].

The goal of the study was to establish a complementary method to the APT investigations to determine the interface chemistry from a second technique of this somewhat beam-sensitive material at rather low dose of electrons. When looking at the possible interface configurations aside from the ZnTe and CdSe species it becomes obvious that the two other configurations, namely ZnSe and CdTe exhibit a significant lattice mismatch as listed in Tab. 4.1. Therefore, the presence of ZnSe or CdTe would both

introduce rather large changes of the lattice spacing while the sign is different for these two, rendering an analysis of the lattice parameter suitable to determine the chemistry.

Material	Uniaxial	Biaxial
CdSe	-0.6 %	-0.9 %
ZnSe	-12.2 %	-16.7 %
CdTe	+9.9 %	+13.3 %

Table 4.1: Calculated lattice distance in growth direction of CdSe and possible interface species ZnSe and CdTe relative to ZnTe (substrate) for uniaxial and biaxial strain cases. Lattice parameters and elastic constants taken from [119, 120, 121].

Fig. 4.1 depicts the ZnTe/CdSe superlattice imaged by HR-HAADF with the letters A and B denoting the two present types of interfaces, namely from ZnTe to CdSe in growth direction and vice versa, respectively. Previous preparation attempts exhibited anisotropic removal of material at the interfaces, leading to jumps in sample thickness and thus hindering the high-resolution imaging of a whole region around an interface. Using a cleaving approach allowed for clear imaging of a large area, as depicted in Fig. 4.1.

The change of atom types occupying the group-II and group-VI sublattice positions is clearly visible by the changing intensities within the dumbbell. But instead of using the intensities, the positions will be used to determine the chemistry.

To facilitate the determination of atom positions, stacks of images were acquired and aligned as explained in 3.1.1. Fig. 4.2 (a) shows such an image created from 15 individual images depicting a region containing interface type A and B. The SNR of the ZnTe region is 6.5. No dip in intensity is visible in between the two atoms of the dumbbell due to the difference in atomic number. Determining the atom positions by TeMA and choosing a whole dumbbell as a template leads to an artificial strain of several percent at the interfaces due to the strain and the change of intensities within the dumbbell (cf. Sec. 3.1.1). Thus, a fitting-based method is used here; after obtaining estimates of the dumbbell positions from TeMA, they were subsequently used as a starting parameters to fit two two-dimensional Gaussian functions with an additional term to account for asymmetries to the dumbbells (15 free parameters). The dumbbell position is furthermore defined as the center in between the origins of the two Gaussians. A map of the the local lattice variation perpendicular to the interfaces is obtained by calculating the component in growth direction of the (111) neighbor distances relative to the ZnTe value, and it is depicted in Fig. 4.2 (b). The error of the measurement is relatively high due to the SNR of only 6.5 and the use of fitting instead of TeMA: 4.8pm, corresponding to 1.4 %. However, due to the large strains, the result is sufficient: the

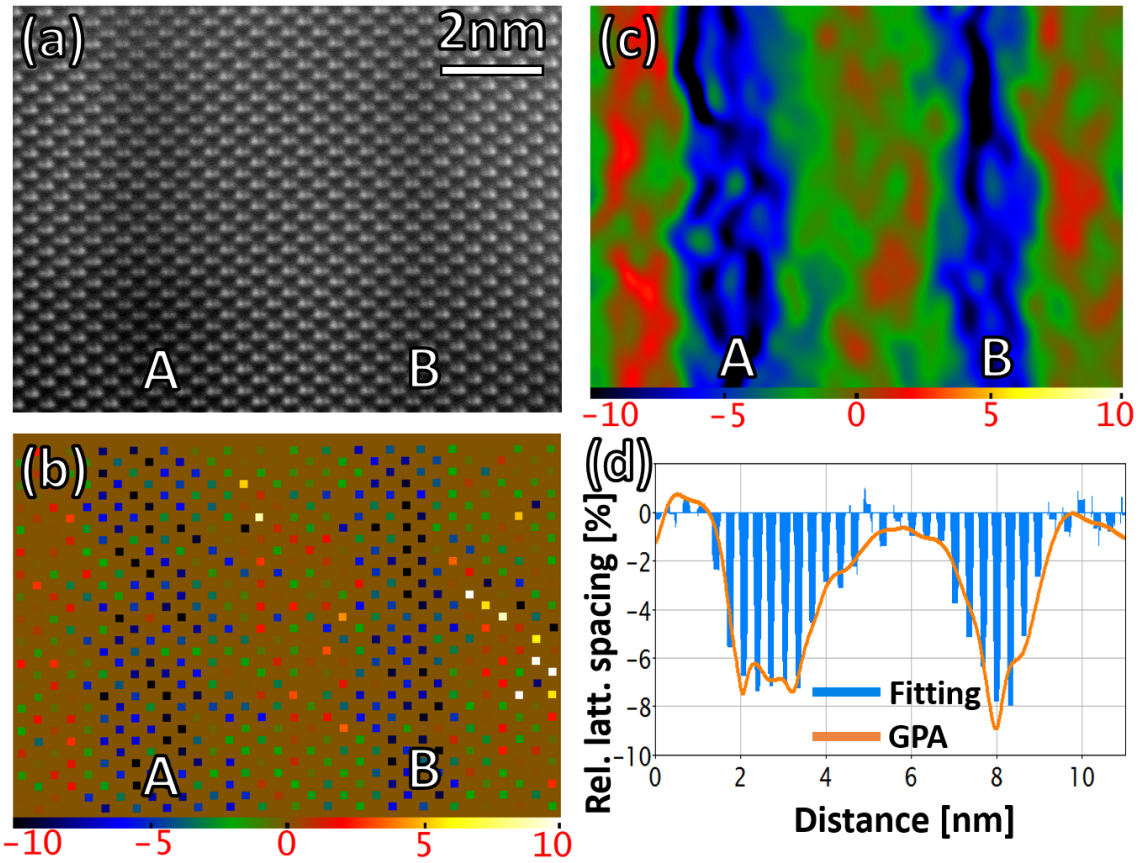

Figure 4.2: (a) HAADF image obtained from aligned stack. (b) Map of local lattice parameter in growth direction relative to ZnTe value (scale in percent). (c) GPA map as a reference using the (004) spot so to avoid artifacts as described by [81]. (d) Comparison of line profiles averaged over tho whole height of the maps for the two methods.

lattice parameter at the interface is obviously substantially smaller (by about 8%) than the ZnTe layers, giving clear evidence of a substantial amount of ZnSe bondings at both interfaces.

To check the result from fitting the atom positions against a well-established method, GPA was performed on the same data. As mentioned in Sec. 4.2 it is important to choose reciprocal lattice vectors that satisfy the $\mathbf{G} \cdot \mathbf{r}_{subl} = \nu$ criterion, as has been pointed out by Peters et al. [81].

A strain map from GPA that was obtained utilizing the (220) and (004) planes, and therefore respecting this rule, is shown in Fig. 4.2 (c). A comparison of the two methods in the form of a profile across the interfaces, integrated over the whole height of the image shows a very good agreement of the two techniques. However, while the map from fitting has atomic resolution, this is not possible for GPA due to the limitation imposed by the size of the mask applied to reciprocal space. It should be noted that the outcome of this comparison hinges on the high SNR of an image and the negligible influence of

scanning artifacts due to the registration of a stack of images. For single, noisy images the fitting performs badly while GPA is very robust (also owed to the spatial averaging in real space due to the mask in Fourier space).

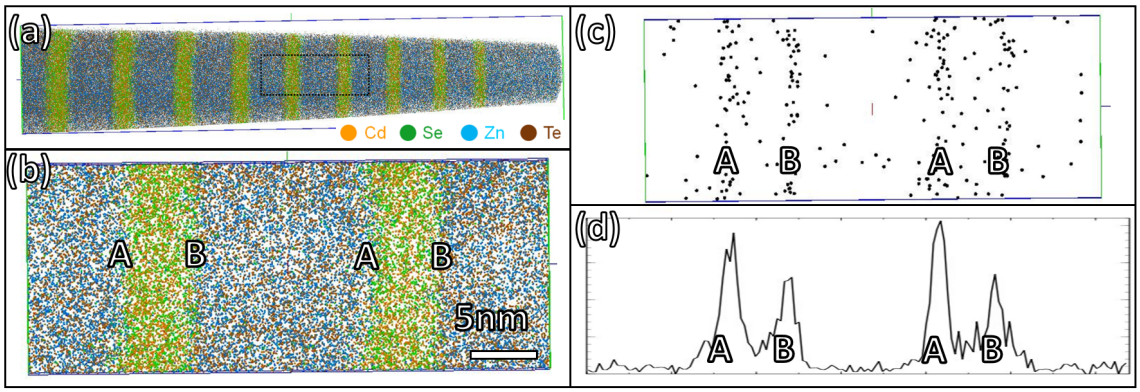

Figure 4.3: (a) Overview of the atom probe tomogram depicting the whole reconstructed needle. (b) Zoom to an area depicting two pairs of A and B interfaces, comparable to Fig. 4.1. (c) Positions of ZnSe species found in the mass spectrum. (d) Profile of ZnSe species integrated over the whole height. Images courtesy of Bastien Bonef.

To validate the obtained results, APT results on the same sample obtained by Bastien Bonef are depicted in Fig. 4.3. An overview of the analyzed needle is given in (a) and a zoom to a region corresponding in width to Fig. 4.1 is shown in (b). Apart from ions of Cd, Te, Zn and Se also ionized ZnSe was found in the mass spectrum (n.b.: no CdTe species could be detected) and the positions are mapped in (c). A profile of ZnSe species across the layers reveals peaks at both interface types A and B and is qualitatively well in agreement with the results from the strain analysis.

The waviness of the interfaces (cf. 4.1) and the resulting blur in the projection through the sample (determined to be about 80nm thick by means of quantitative HAADF contrast analysis) hinder a truly quantitative analysis. It is also not determined by means of simulation if the strain state of the sample is closer to the uniaxial or biaxial strain case. But nevertheless, it can be concluded that the lattice contraction of about 8% at the interfaces mean that they are mostly or even entirely ZnSe covered, which is a sufficient information to conclude that the growth precautions taken to avoid this type of interfaces were futile.

4.2 Mapping Strain in SiGe Transistors by 2D Scanning Moiré Fringes

In this section, a scanning moiré pattern is utilized to determine the strain in a SiGe/Si transistor. A limiting parameter for the clock frequency of processors is the mobility of charge carriers. To improve the performance, the host crystal can be strained to flatten the bands and therefore increase the mobility. Here, the strain of a device based on SiGe source and drain that compress the Si channel in between is characterized according to the method explained in Sec. 3.1.2. The device is from STMicroelectronics company and the sample was prepared by Armand Béché (CEA-INAC Grenoble at that time) during his PhD thesis using FIB. More information about the sample and preparation can found in his PhD manuscript [122].

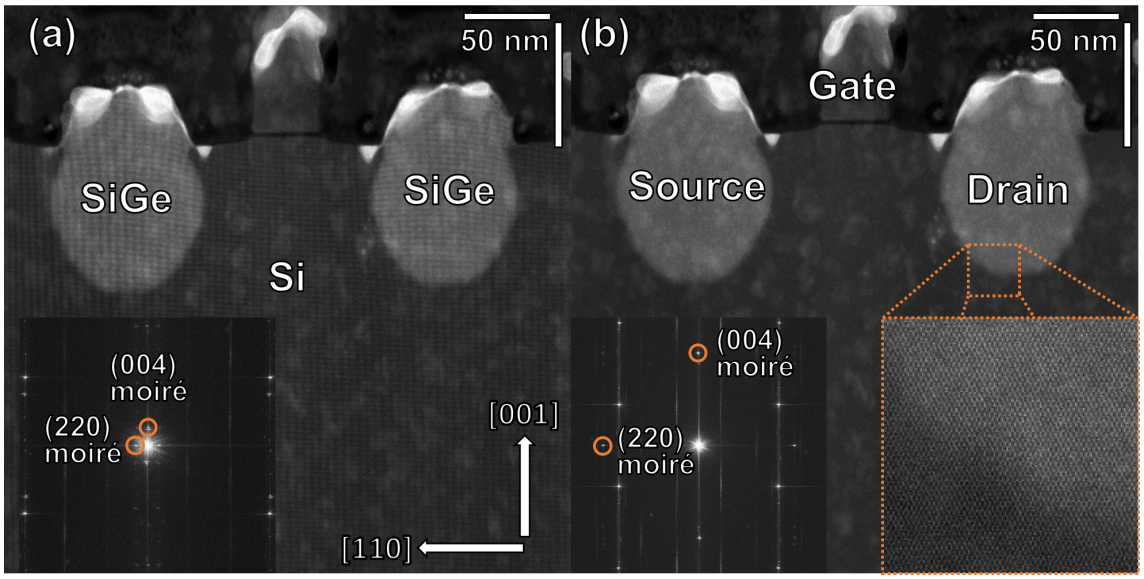

Figure 4.4: Two two-dimensional moiré fringe patterns of a SiGe/Si transistor in [110] ZA. By changing the scanning to a rectangular grid of $\sqrt{2}$:1 aspect ratio a moiré of the (004) and (220) planes is obtained simultaneously. In image (a) the sampling frequency is much closer to the lattice frequency than in (b), producing a larger moiré spacing that allows for a qualitative visual investigation of the strain.

The device is depicted in Fig. 4.4, showing moirés with $d_s > d_l$. In (a) d_s is relatively close to d_l, giving rise to a moiré with large spacing that already provides qualitative insight into the strain distribution. The moiré that is used in the subsequent analysis is depicted in (b). It should be noted that the horizontal and vertical axis have different scaling due to the tweaking of the scan pattern to permit the two-dimensional moiré pattern. Image (b) consists of 2600^2 px with a sampling of 0.1243 nm and 0.0872 nm leading to a field of view of 226 by 323 nm^2.

The nominal Ge content of the SiGe drain and source is 20 %, thus a strain of 1.4 % in growth direction is expected from the lattice parameters and elastic constants of Si and Ge for biaxial strain. GPA is used in Fig. 4.5 to extract the necessary parameters from the moiré. Utilizing the (004) and (220) moiré reflections of the FT of image (a), depicted in (b), allows to map the geometric phase of the two spots as depicted in (c) and (f), respectively. Scanning errors along the horizontal direction (flags) are subsequently corrected in the phase maps by comparison with a reference region. From each phase map the moiré spacing d_m and corresponding angle β are extracted (see (d), (e) and (g), (h)). The moiré fringes amplify the lattice deviations by roughly 2.5 in this case. The maps are down-sampled to 155^2 px to reduce noise, thus reducing the sampling to 2.09 nm in horizontal and 1.46 nm in vertical direction.

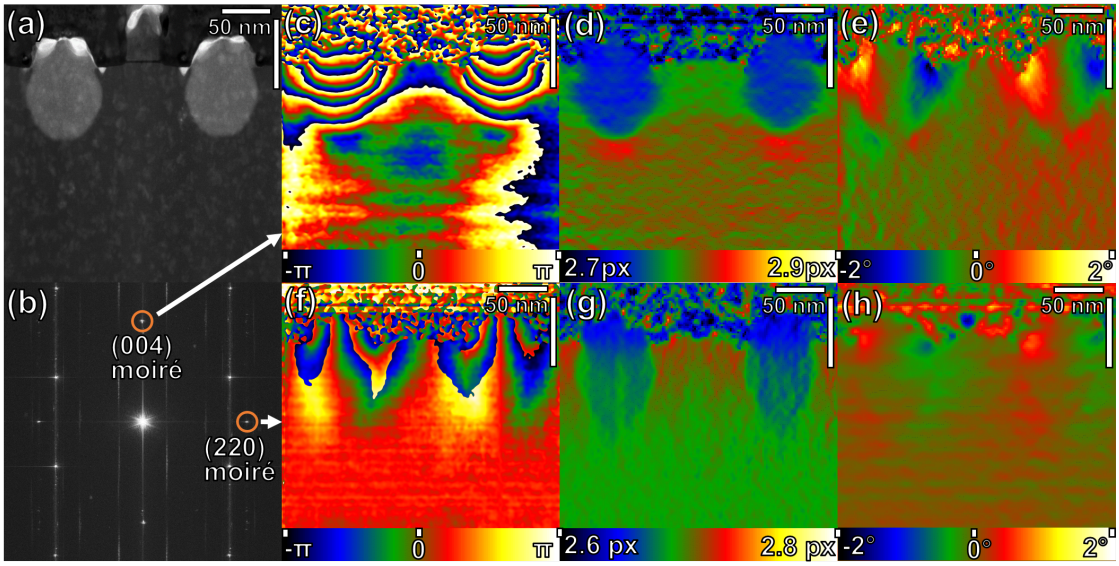

Figure 4.5: GPA of a two-dimensional moiré pattern of a SiGe transistor in [110] ZA (a): the phase maps for the (004) and (220) spots of the FT in (b) are depcited in (c) and (f), respectively. The moiré spacing and angle are extracted from the phase maps and shown in (d) and (e) for (004) and in (g) and (h) for (220).

Next, a MATLAB script is used to calculate the accessible components of the strain tensor, according to the formulae that were obtained in Sec. 3.1.2. The result is shown in Fig. 4.6; the vertical and horizontal strain components as well as the shear and rotation are given in (d), (b), (c) and (d), respectively. The strain is calculated relative to the lattice distance at the bottom of the images. Image (b) shows how the SiGe source and drain exhibit a larger in-plane lattice distance that squeezes the Si channel in between by about 0.4 %. The part of the source and drain that protrudes from the surface expands even more, as it is not limited by the Si channel. In the vertical direction it can be seen that the Si beneath the source and drain is squeezed and that the Si channel has

a positive strain of around 0.3 % due to the compression in the horizontal direction. By measuring the standard deviation of strain in the reference regions of the images, a strain precision of around $6{\cdot}10^{-4}$ is found.

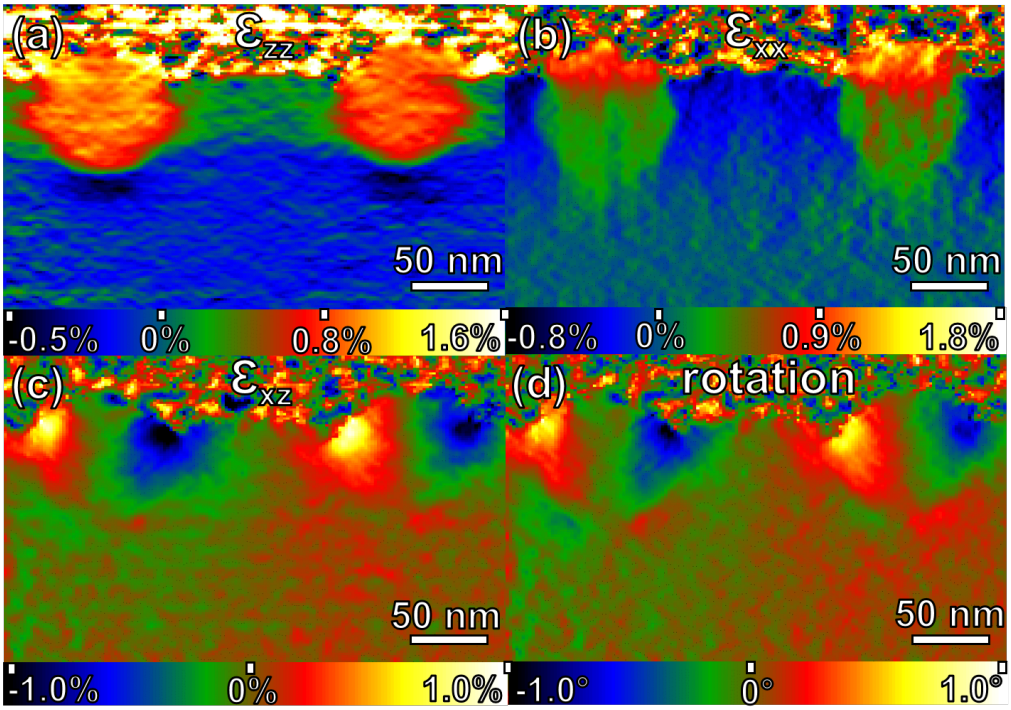

Figure 4.6: Strain components calculated from the two-dimensional moiré pattern shown in Fig. 4.4 (b): the vertical strain component is shown in (a), the horizontal in (b) and shear and rotation in (c) and (d), respectively. The images are stretched to obtain the same sampling in both directions.

4.3 Strain Gradients in Topological Insulator HgTe/CdTe

The goal of the following analysis is to measure with high spatial and strain resolution the strain state across interfaces of the topological insulator (TI) HgTe/CdTe to determine if the strain values are sufficient to open a bulk bandgap in HgTe and the gradients sharp enough compared to the extend of surface states to guarantee the functionality of the TI.

The samples were grown by Candice Thomas and Pierre Ballet from CEA-LETI Grenoble using MBE. FIB preparation of a thin lamella was performed by Nicolas Mollard from CEA-INAC Grenoble. Finite element simulations to account for strain relaxation

from thinning were performed via Comsol Multiphysics and based on linear elasticity theory. These simulations were executed with the help of Nicolas Bernier from CEA-LETI Grenoble.
Two samples are investigated with different HgTe layer thickness; 8 nm and 15 nm. Depending on separation of the surfaces, the material is either a 2D TI or a 3D TI, with either spin-polarized edge or surface states, respectively. The discussion in this section is focused on surface states, although the first sample with 8 nm layer thickness is strictly speaking a 2D TI (more information can be found in [123]). This sample is chosen because it is especially challenging for growth and characterization. Afterwards, the 15 nm HgTe layer sample is analyzed, which is clearly a 3D TI, and magneto-transport results obtained by Candice Thomas are shown for this sample.
A microscopy based first author article and a transport based co-authored article concerning this material system have been submitted for publication.

Topological insulators are a rather new class of materials that offers intriguing properties originating from their chiral and massless Dirac fermions [124, 125]. The 2016 Nobel prize awarded to D. J. Thouless, F. D. M. Haldane, and J. M. Kosterlitz "for theoretical discoveries of topological phase transitions and topological phases of matter" [126] underlines the importance of topological insulators. Among them, the HgTe/CdTe system is one of the most promising ones due to its high electronic mobility and low bulk conductivity [127]. Systems like HgTe/CdTe, that exhibits insulating bulk due to a strain bandgap, show signatures in magneto-transport that indicate topological insulator behavior [128, 127], thus underlining the potential for practical applications. HgTe itself is a semimetal, but by growing it epitaxially on CdTe the deviation in lattice parameter of less than 0.4 % opens a bandgap in bulk of 22 meV according to theory [128].
The topological surfaces of 3D TI should be equivalent, except for a difference in potential because of the distance to the top gate [129], however this assumption is based on perfect interfaces. Yet, the structural and compositional equivalence is rarely feasible during the growth process. Therefore, it is important to assess the strain at the interface level because the band alignment at HgTe/CdTe interfaces is very sensitive to the strain (and chemical) gradients. The investigated material system consists of a HgTe layer that is sandwiched in between two $Hg_{0.3}Cd_{0.7}Te$ layers of 30nm thickness. There are two main reasons for the $Hg_{0.3}Cd_{0.7}Te$ barriers instead of just growing HgTe on top of CdTe. The top layer protects the HgTe from desorption of Hg and the $Hg_{0.3}Cd_{0.7}Te$ can be grown at the same, lower growth temperature of HgTe (compared to CdTe), thus leading to more homogeneous interfaces of the HgTe.

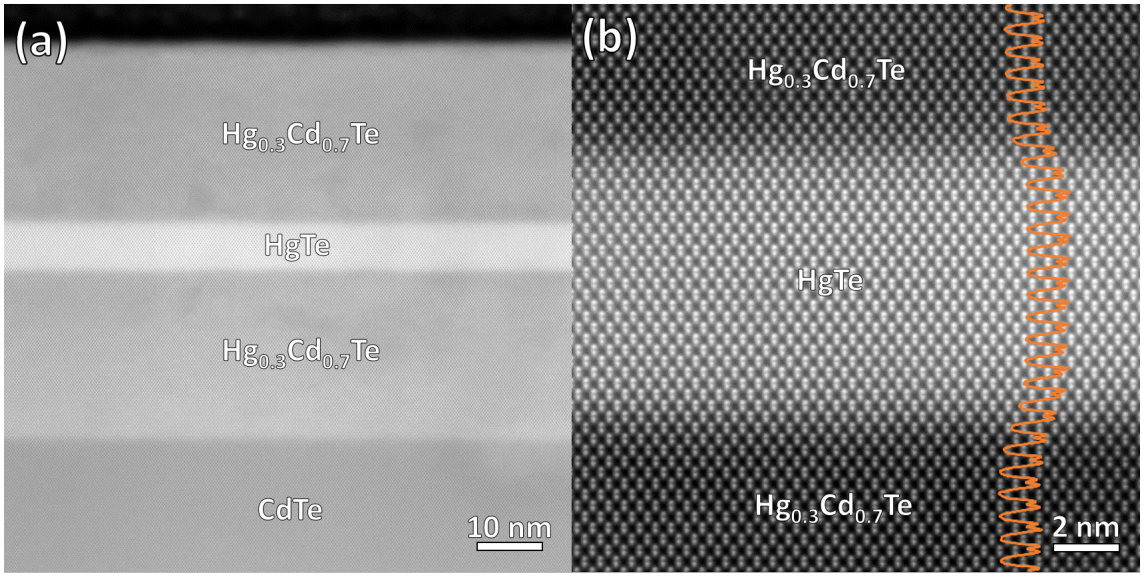

Figure 4.7: (a) HR-HAADF image (obtained from aligned stack) of the HgCdTe/HgTe/HgCdTe sandwich and the top part of the CdTe buffer, demonstrating the high quality of the sample. (b) Zoom of the HgTe layer with superimposed profile along a line of atom columns across the interfaces (orange). The change in atomic species on the sublattice positions is visible in the dumbbell contrast.

The material is very brittle, which hindered the preparation by tripod polishing. FIB milling is complicated as the material ablates rapidly making it difficult to avoid surface damage of the lamellae. It degrades slowly under ambient conditions and was therefore stored under nitrogen atmosphere and observed within a few days of preparation. Hydrogen-argon plasma for cleaning purposes leads to severe etching, but oxygen-argon plasma does not deteriorate the material. Beam sensitivity is not pronounced but a rather strong dechanneling necessitates thin FIB lamellae (around 50nm) for a clear distinction between the dumbbell atoms in [110] zone axis.

Fig. 4.7 (a) shows an HR-HAADF image from a registered series depicting the 8nm HgTe sandwiched between the two $Hg_{0.3}Cd_{0.7}Te$ layers and the top part of the CdTe buffer (and a bit of vacuum at the top part of the image). No extended defects can be observed and the sample is rather homogeneous, except for a few stain-like areas owed to the difficult preparation. A higher magnification image of the HgTe layer is shown in (b) together with a profile along one line of atom columns. The interfaces are relatively sharp and the dumbbell contrast qualitatively matches the average atomic numbers of group-II and group-IV positions (Hg = 80, Cd = 48, Te = 52, $Hg_{0.3}Cd_{0.7}$ = 57.6).

The interface width is determined according to the method described in section 3.1.3 by fitting the derivative of the image. FWMH values of the HgTe interfaces of 1.6 nm

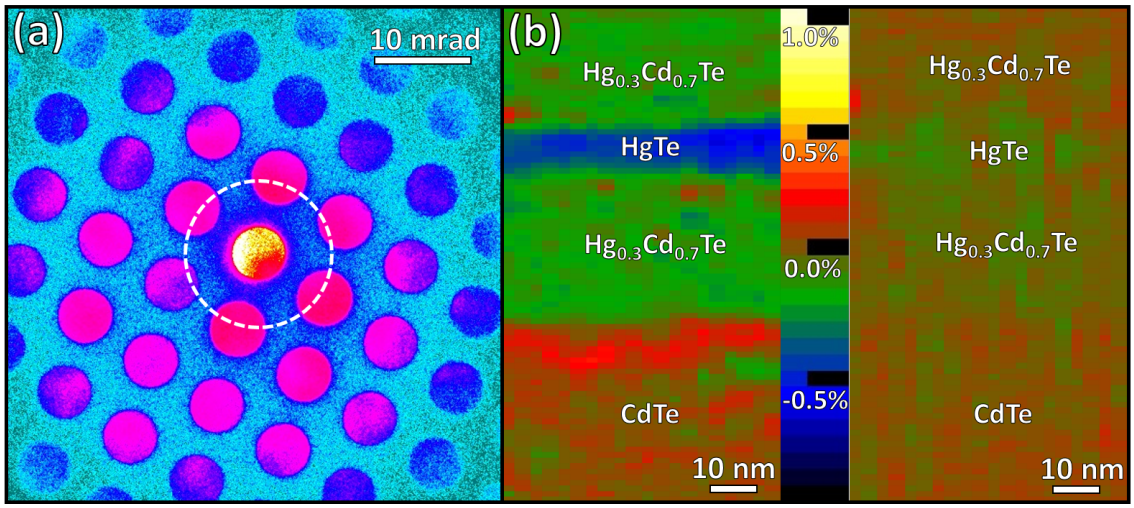

Figure 4.8: (a) Exemplary diffraction pattern of $Hg_{0.3}Cd_{0.7}Te$ from NPED series of the material stack. Maps of the variation of lattice parameters relative to the CdTe buffer are shown in (b) with the growth direction and in-plane direction on the left-hand and right-hand side, respectively. The color scale depicts the variation in percent.

for the interface towards $Hg_{0.3}Cd_{0.7}Te$ in growth direction and 1.3 nm for the bottom interface is measured. The slightly broader top interface probably stems from the higher roughness of the HgTe surface compared to the $Hg_{0.3}Cd_{0.7}Te$ surface [123].

Fig. 4.8 (a) shows a typical diffractogram from an NPED series of the material (color-coded on logarithmic scale) with the white circle indicating the utilized precession angle of 0.35°. In (b) maps of the lattice variation are shown for the growth direction (left-hand side) and the in-plane direction (right-hand side). Shear and rotation maps are omitted due to the lack of such effects in the case of defect free epitaxy. More explanations concerning strain and elastic constants can be found in App. B. The growth direction component shows a clear difference between the layers with a certain amount of fluctuations parallel to the interfaces. The in-plane component indicates a small amount of strain relief of the HgTe (difference of lattice parameter is -0.07 %) due to the thinning of the sample.

To assess the influence of the beam size on the measured strain gradient, VHAADF images are constructed and the width of the interfaces obtained from fitting the derivative compared to the values from HR-HAADF, as described in section 3.1.3. The upper interface yields a value of 2.6 nm and the lower one of 2.0 nm. Comparing these values to the intensity gradient of the HR-HAADF image provides us the average width of the beam within the sample, which is around 1.8 nm with an error bar (from the difference of the two interface widths in both cases) of around 0.15 nm.

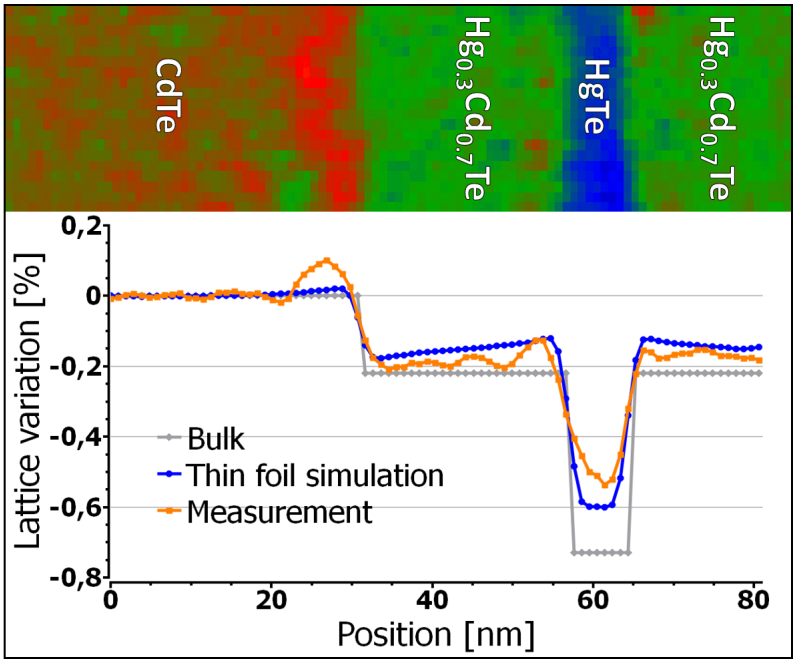

Figure 4.9: Lattice variation as map (top) and line profiles (bottom) of the experimental value (orange), the ideal bulk structure with perfect interfaces (gray) and the relaxed ideal structure for the experimental thickness value and the beam size taken into account (blue).

Extracting a meaningful strain gradient necessitates the separation of strain relaxation from thinning the specimen from the measured strain profile. The experimentally obtained thickness value of around 50 nm (PACBED) was used to perform finite element simulations for the given sample geometry to determine the strain relaxation. Additional input parameters are the given layer thicknesses from HAADF (sharp interfaces are assumed) as well as the lattice parameters for bulk and the elastic constants, taken from Cottam et al. [130] for CdTe and from Greenough et al. [131] for HgTe. A Hg content of 30 % was assumed for the HgCdTe barriers and the values interpolated according to Vegard's law. Repeating the calculations for a thickness value of 100 nm had relatively little effect on the outcome.

Subsequently, the simulated strain profile was broadened by the measured beam width. Fig. 4.9 shows the experimental map on top with the growth direction pointing to the right and below the profiles for the perfect bulk structure in gray, the experiment one in orange and the simulation result broadened by the beam size in blue. Simulated and experimental profiles agree well with even the faint slopes of strain in the barriers (from relaxation of strain due to thinning) being reproduced. One difference is the larger lattice parameter at the top of the CdTe buffer. While the simulation also predicts a positive value, the experimental result is too large. The origin of this might be related to the growth interruption that is necessary to cool down before continuing the growth

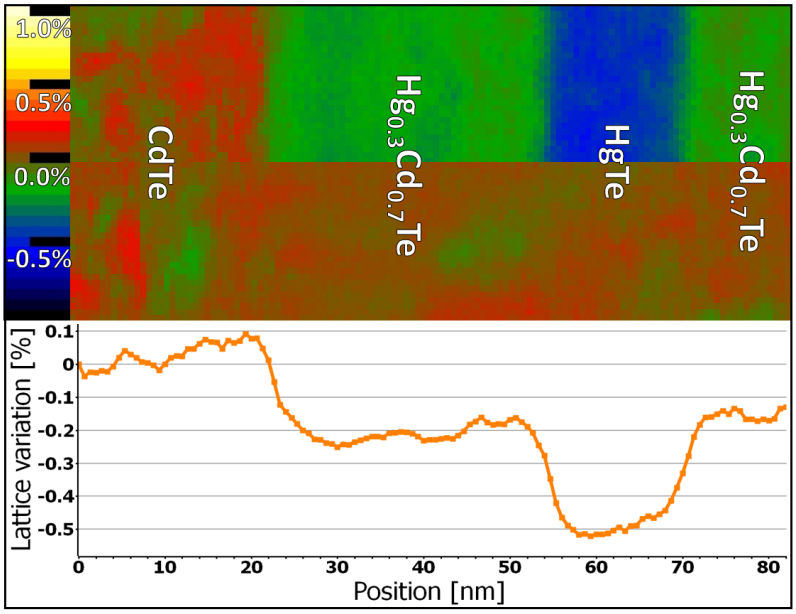

Figure 4.10: Lattice variation for sample with 15 nm HgTe layer and 30nm $Hg_{0.3}Cd_{0.7}Te$ barriers. The growth direction component is depicted in the top part and the profile in the bottom part corresponds to the average, integrated over the whole height. The lattice variation in direction parallel to the interfaces is shown in the center.

of the layers at a lower temperature. Anyways, as this part of the sample plays no role for the TI behavior and the absolute difference is smaller than 0.1 % it is not critical. The second deviation is the absolute value of strain in barriers and HgTe layer. The small difference for the barriers (around 0.05 %) may be due to a slightly different composition of the HgCdTe, but this has no influence on the TI properties. The fact that the HgTe layer exhibits a value 0.05 % larger than the predicted -0.5 % might stem from residual Cd in the HgTe. However, the amount of 5 % Cd that would cause this effect is too small to close the band gap of the HgTe (the bulk gap vanishes only at 17 % Cd according to Hansen et al. [132]). The additional width of the experimental strain gradient at the HgTe interfaces compared to the broadened simulation stems now from the imperfections of the interfaces that have been assumed to be sharp in the simulation. For the upper interface a value of 2.8 nm is found for the strain gradient and for the lower interface 3.5 nm, while the finite element simulation broadened by the 1.8 nm beam size yields 2.4 nm for both interfaces. When comparing the strain gradient to the chemistry gradient obtained from HR-HAADF and taking the 1.8 nm beam size of the NPED into account, there is a difference of the FWHMs for the upper interface of about 0.4 nm, while it is 1.3 nm for the lower interface. The fact that the strain is not as abrupt as the chemistry gradient seems reasonable, however the much larger width of the lower interface is not clear. It could be an artifact from sample preparation; when

comparing the lower interface strain gradient and the gradient at the CdTe/HgCdTe interface in Fig. 4.9 a similar behavior is observed. In both cases a positive bump in the strain profile on the left-hand side of the interfaces can be seen. Due to the fact that during FIB preparation the impinging Ga ions came from the right-hand side and because in both cases a gradient from a softer to a harder material in beam direction is given, this might cause a modification of the observed strain gradient. The effect is more pronounced for the CdTe/HgCdTe interface because the difference in hardness is larger. Nevertheless, in both cases, even with a possible broadening from preparation, the values are smaller than the surface state extension of around 5 nm [123], therefore conserving the TI properties of the material.

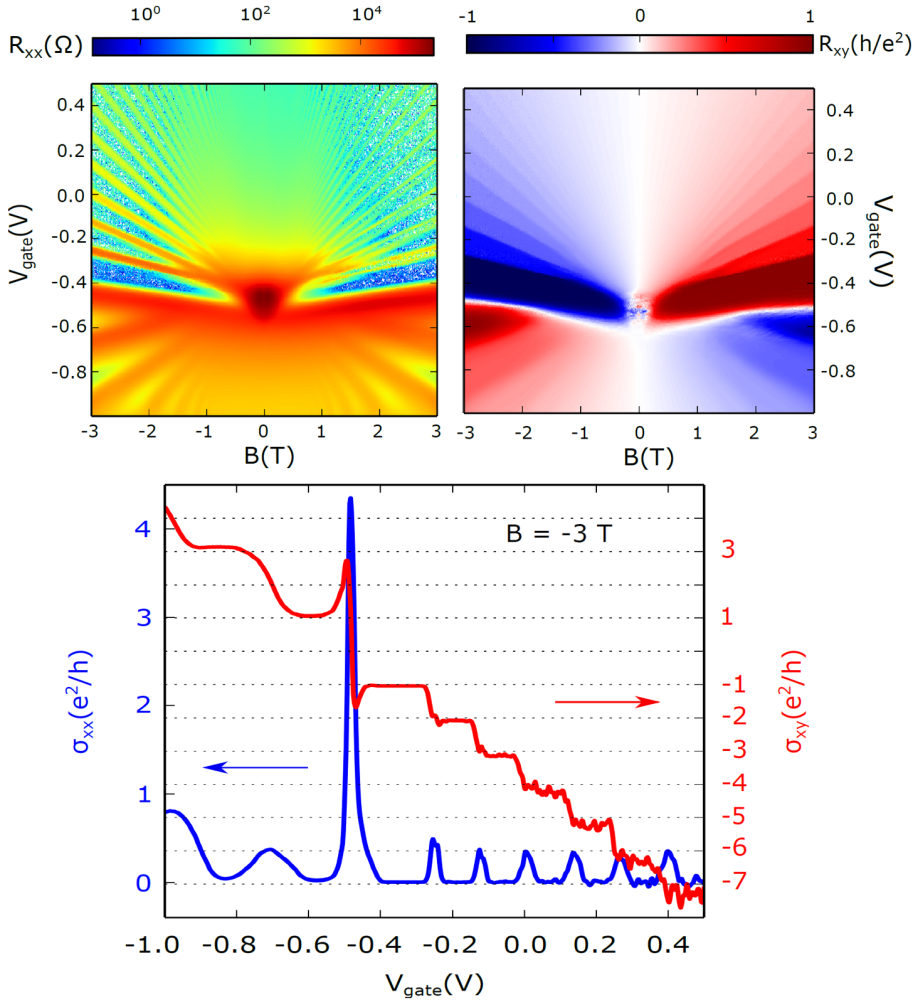

Figure 4.11: Magneto-transport measurements of the same sample depicted in Fig. 4.10: Longitudinal resistance R_{xx} (top left) and Hall resistance R_{xy} (top right) as a function of magnetic field B and top gate voltage V_{gate} at 100 mK. Line profiles for -3 T are compared below (here conductance is depicted) and show well defined Hall plateaus that coincide with peaks in longitudinal conductance. Images courtesy of Candice Thomas.

A similar analysis is depicted in Fig. 4.10 for a sample consisting of a 15 nm HgTe layer with 30nm $Hg_{0.3}Cd_{0.7}Te$ barriers. The resulting strain is quite similar, although the 15nm HgTe layer makes it easier to characterize. The width of the strain gradient at the HgTe interfaces (including beam width, chemical gradient and strain relaxation) is about 4.0 nm leading to a very similar result as discussed above for the 8nm HgTe sample. The fact that the sample properties are well within the limits that allow for TI properties is demonstrated by the excellent magneto-transport characteristics obtained for this sample by Candice Thomas and depicted in Fig. 4.11. Longitudinal and Hall resistances in dependence of gate voltage V_{gate} and magnetic field B were measured in a dilution fridge at 100 mK. The Hall resistance in (b) shows very clear plateaus that coincide with the vanishing of the longitudinal resistance depicted in (a). More general information and details of the measurements can be found in [123].

4.4 Quantification of In Fluctuations in InGaAs Quantum Well Fin

The integration of III-V semiconductors on Si is highly desirable as it allows to combine the mature and efficient Si technology with the properties of III-V materials. This can be exploited in the form of optoelectronic devices due to the direct bandgap that can be realized in III-V semiconductors or for transistors that benefit from their high charge carrier mobility. However, combining Si with III-V semiconductors is nontrivial. The lattice mismatch between the materials as well as the growth of polar material on nonpolar substrate gives rise to defects. Different ways exist to handle this problem, the one used here is aspect ratio trapping (ART). The III-V material is grown by selective epitaxy in trenches in a SiO_2 mask and the defects that arise at the interface between Si and III-V are stopped at the side walls. So if the aspect ratio between the III-V thickness and the width of the trench is large enough, almost all defects are gathered at the walls, thus the name. The desired III-V layer structure can then be grown in high quality on top of this buffer.

In this section, an InGaAs quantum well fin (QWF) is analyzed which is grown in between AlAs layers on top of a GaAs buffer, as depicted in Fig. 4.12 (a). The question is how homogeneous the In distribution within the InGaAs QWF is. The targeted In concentration is 30 % and x-ray diffraction (XRD) measurements showed about 28 % In. The sample was grown at LTM in CNRS Grenoble by metal-organic chemical vapor deposition (MOCVD) on 300 mm Si (001) wafers. FIB preparation was done by Joyce Roque from CEA-LETI Grenoble. In previous TEM studies of In containing ternary com-

pound semiconductors it was shown that prolonged intense electron irradiation can lead to In clustering [133]. The authors found that the local In concentration starts to deviate after applying a dose of around 100k e/Å^2. Therefore, the quantification of contrasts in HAADF (in contrast to spectroscopy), in combination with a swift measurement were deemed suitable to analyze the QWF. The dose of the measurement shown here is 20k e/Å^2 and the exposure beforehand for centering and focusing again approximately the same.

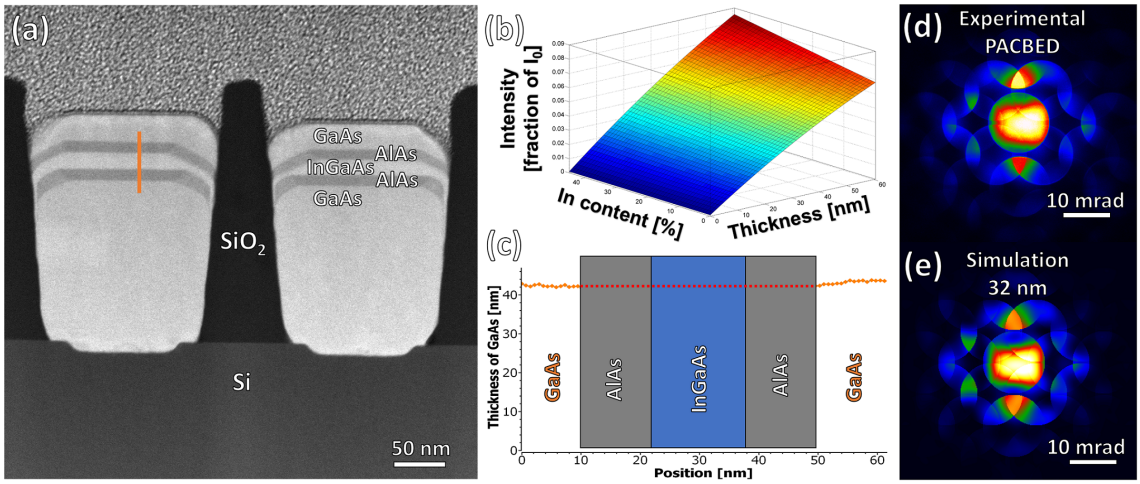

Figure 4.12: (a) HAADF image of the InGaAs QWF structure embedded in AlAs. (b) Intensity-thickness-concentration diagram for InGaAs from FP simulations. (c) Profile depicting the GaAs thickness on both sides of the stack, corresponding to the orange line in (a). (d) experimental PACBED pattern of the GaAs barrier and (e) simulation.

To quantify the HAADF signal, the procedure described in Sec. 3.2.1 is used. The measurements are performed at 200 kV with 24 mrad convergence angle. Results from FP simulations of InGaAs are depicted in Fig. 4.12 (b) in the form of an intensity-thickness-concentration plot. The simulations were performed using calculated Debye-Waller factors for InAs and GaAs from Schowalter et al. [134] and interpolating for different InGaAs compositions using Vegard's law. The detector sensitivity is taken into account by multiplying the simulation result with the detector sensitivity and considering the cut-off angle (77-191 mrad angle range for the experiment).

First, the thickness of the GaAs barriers is evaluated. As the composition is known (pure GaAs) the intensity yields directly the thickness. A profile of thickness values for GaAs on both sides of the layer stack, according to the orange line in (a), is depicted in (c). The thickness on both sides of the stack is 42 nm with only small fluctuations below 1 nm. To check the result, PACBED is performed on the GaAs and the pattern is depicted in (d). A comparison with simulations for different thicknesses showed the best

agreement for 32 nm, which is depicted in (e). PACBED measured only the crystalline thickness, while amorphous layers contribute also to the scattering signal detected in HAADF, which explains why the thickness from HAADF is larger. If we assume the scattering from amorphous layers to be the same as from the crystal, the difference would account for 5 nm thick layers of amorphous material on both sides of the FIB lamella. As the scattering from the amorphous is probably stronger due to dechanneling, the layer is likely to be even thinner. The values seem reasonable for a FIB preparation with a final polishing performed at beam energy of 2 kV.

Next, the In concentration in the InGaAs QWF can be determined using the obtained thickness. The average concentration that is extracted is around 14 %, which is significantly lower than the targeted 30 % and the value of 28 % from XRD. The reason is that a perfect crystal was assumed in the simulations in which the atoms are situated at the crystallographic positions. This a bad approximation for InGaAs, where the difference in ionic radii of the atoms leads to so called static atomic displacements (SADs). These SADs mean that the atoms are displaced relative to the crystallographic sites, which leads to a type of Huang scattering if the SADs are large, and as a result electrons are scattered to intermediate angles (around 40-50 mrad), thus reducing the HAADF intensity [53]. Grillo et al. [135] have shown for InGaAs that not taking into account the SADs for similar specimen thickness and 24 % In content led to an underestimation of the In content by almost half of the real concentration. This seems to agree well with the found value of 14 % In compared to the 28 % from XRD. The quantification of In concentrations in InGaAs from HAADF contrast using SADs was validated by Mehrtens et al. [136] by comparing the results to other techniques.

As the goal of this analysis is to determine the distribution of In and not the total concentration, new FP simulations on relaxed crystal structures are omitted and instead the concentration from XRD is used as an input parameter. The intensity-concentration relationship is kept fixed for 0 % In and the slope is scaled using the relationship of intensities with and without SADs from Grillo et al. [135] so that the average intensity value in the InGaAs QWF corresponds to the 28 % In from XRD.

An HR-HAADF image of the InGaAs layer in between AlAs barriers and GaAs is depicted in Fig. 4.13 (a). To investigate composition fluctuations with atomic resolution, a Voronoi tesselation is applied. The dumbbell positions are retrieved by means of TeMA (as described in Sec. 3.1.1) and subsequently the intensity within a Voronoi cell, which is defined by all the points which are closest to a given position, is averaged. The resulting intensity maps for an InGaAs region and a GaAs region, as variations from the mean intensity value (of course background corrected), are shown in (b) and (c), respectively. The InGaAs region exhibits lines of different contrast running along (111) planes. It is

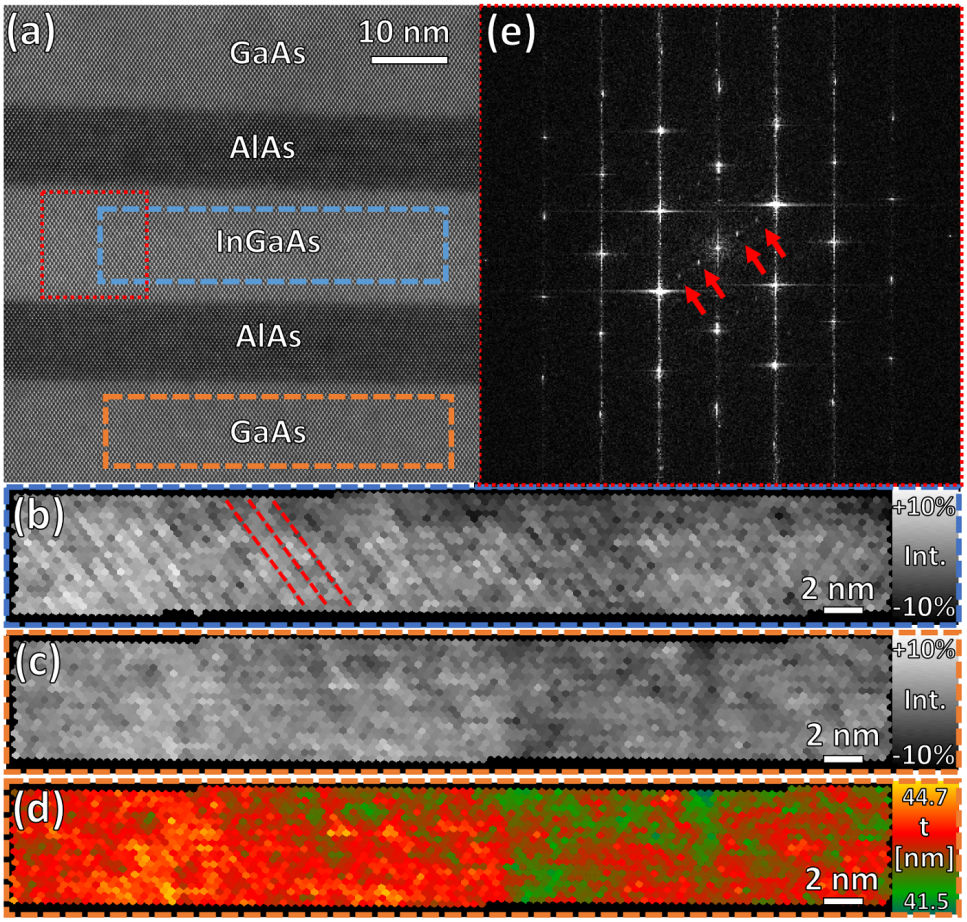

Figure 4.13: HR-HAADF image of the layer stack (a) and Voronoi tesselations of the two indicated regions in InGaAs (b) and GaAs (c). CuPt type ordering can be observed (red lines as a guide to the eye). A thickness map created from the intensities shown in (c) is given in (d) and shows that the intensity differences in GaAs correspond only to very small thickness variations. The observed ordering in (b) is every third plane, which can also be seen in the FT of the region marked red in (a) which is depicted in (e).

clearly PtCu ordering, which can occur in III-V semiconductors, especially when grown by MOCVD [137] and which reduces the bandgap [138].

To describe the In fluctuations correctly, it is necessary to compare the variations in intensity of the InGaAs to the ones found in GaAs. As the GaAs does not fluctuate in chemistry, the intensity variations in (c) must stem from surface roughness. A thickness map constructed from (c) is shown in (d). There is a variation in thickness between the left-hand side and the right-hand side of about 1.3 nm and a very local roughness of below 0.4 nm (root mean square value). Taking this variation from sample roughness into account, the In fluctuations can be determined. The standard deviation of In concentration in the whole region is around 3.0 % In. In the region at the very right, where no ordering can be observed, the variation is 1.3 % In. Very locally, at the lines of

strong ordering, the deviation in In concentration between adjacent (111) planes can be above 10 % In. It should be noted that instead of alternating planes, every third plane seems to be In deficient in (b). This is validated by a FT of the area marked in red in (a), given in (e). Two extra spots can be seen in between the center and the (111) spot. To the authors knowledge, this is atypical for CuPt type ordering where the ordering is normally between adjacent planes and only one extra diffraction spot is observed in between (000) and (111).

4.5 Strain and Piezoelectric Fields in a-plane AlN/GaN

In the field of compound semiconductors, III-nitrides offer a wide range of possibilities for applications. A fundamental problem for optoelectronic applications is the polarization of wurtzite-type crystals. The polarization can have two components; the spontaneous polarization that is intrinsic to the material and the piezoelectric polarization from external deformations. This feature that exists due to the lack of inversion symmetry of the crystal can lead to sheet charges at interfaces where the polarization changes. At free surfaces the charges are normally neutralized e.g. by gas atoms from the environment. However, at buried interfaces these sheet charges are stable and as a result electric fields arise in between, similar to the case of a plate capacitor. These fields cause the quantum-confined Stark effect which can severely influence emission characteristics of a device.
As the polarization vector in wurtzite crystals points in [0001] direction (or antiparallel), a way to avoid problems related to polarization gradients is to grow the wurtzite crystal not on a c-plane but perpendicular. In these cases no fields are meant to be present in the sample if the interfaces between layers are perpendicular to [0001]. Two non-polar planes are used to grow in such a way; the m-plane and the a-plane. In this section, an a-plane grown AlN/GaN superlattice is observed by means of NPED E-field and strain mapping. The sample was grown by plasma-assisted MBE on SiC $(11\bar{2}0)$ substrate in the group of Bruno Daudin (CEA-INAC Grenoble) and was FIB prepared by David Cooper (CEA-LETI Grenoble).

A HAADF overview image of the layer stack in [0001] ZA can be seen in Fig. 4.14 (a). NPED for simultaneous strain and field mapping is performed on an 80x80 nm^2 area containing several layers. 50x50 images of 512^2 px each are obtained using a beam current of 76 pA, 0.3 degree precession angle, 1 kHz precession frequency, a convergence

angle of 2.3 mrad and 100 ms exposure time of the CMOS camera. The VHAADF of the mapped region is depicted in (b) (cf. Sec. 3.1.3 for several virtual images of this sample). The bright part at the top of the image is an intensity fluctuation. While being a nuisance for the virtual image, it is educational to observe that it has no influence at all on the measurements performed on this data set, because they are independent of the total intensity of each frame.

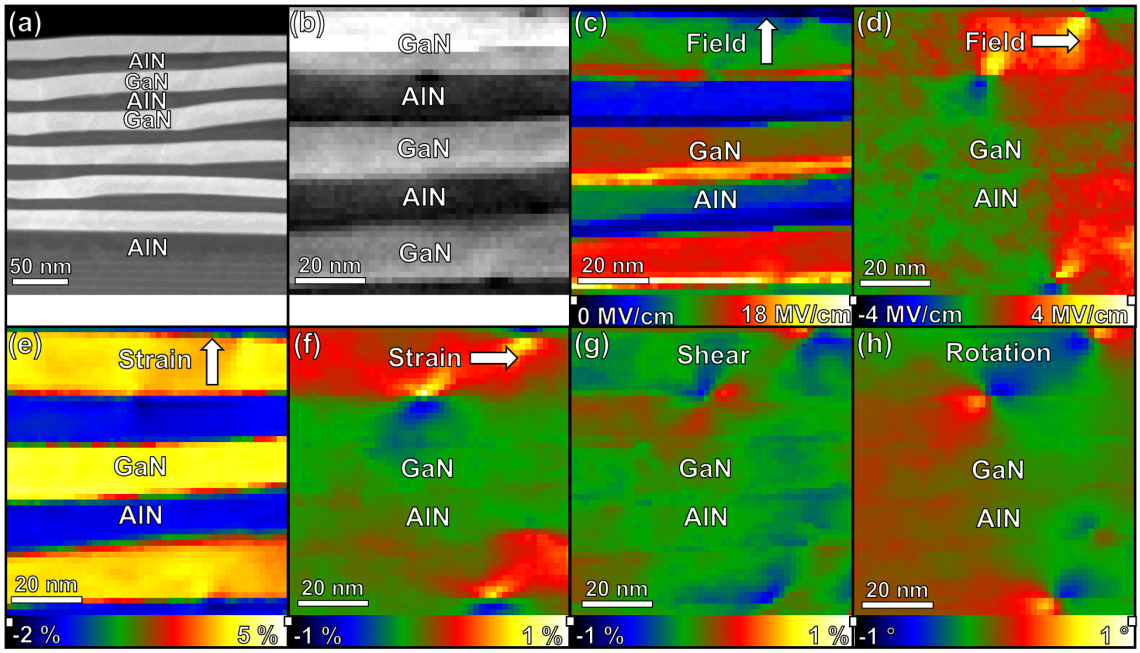

Figure 4.14: Simultaneous electric field and strain measurements from NPED on an a-plane AlN/GaN MQW sample in [0001] ZA. An overview HAADF image of the layer stack is shown in (a). The VHAADF exhibiting an HAADF like contrast is shown in (b). The bright region on top is an artifact from intensity fluctuation. It should be noted how the intensity variation has no influence on the measurements. Maps (c) and (d) depict the field in vertical and horizontal direction, respectively. The strain perpendicular and parallel to the layers are given in (e) and (f), the shear in (g) and the rotation in (h). The strain is relative to the AlN buffer. Dislocations and their influence on strain and field can be observed.

The strain in growth direction is mapped in (e), the component parallel to the layers in (f) and shear and rotation in (g) and (h), respectively. Via another measurement that is not shown here, the strain in (e) is related to the buffer value. The measurements clearly reveal strain fields from dislocations that run along the c-axis (in projection direction). At the bottom of (f) it can e.g. be seen how a dislocation at the bottom most GaN layer leads to a relaxation of strain within this layer to the right-hand side of the defect. The effect is also visible in (e), although less good due to the larger overall strain present in this area.

Even more interestingly, fields can be seen in the material in general and also correlated with the defects, as depicted in (c) and (d). The field strength is calculated using the sample thickness of 140 nm as determined by CBED measurement. Rather strong fields above 10 MV/cm seem to be present in growth direction and lower fields parallel to the interfaces. It is interesting to observe how e.g. the strain field of the dislocation at the bottom, that is discussed above, is correlated with the change in electric field as seen in (d) and also in (c) (although with less contrast). The piezoelectric polarization of a material equals the strain in the material times the piezoelectric constants. A gradient of the polarization gives rise to charges that cause the beam deflection. Therefore, this correlation of strain and field is anticipated.

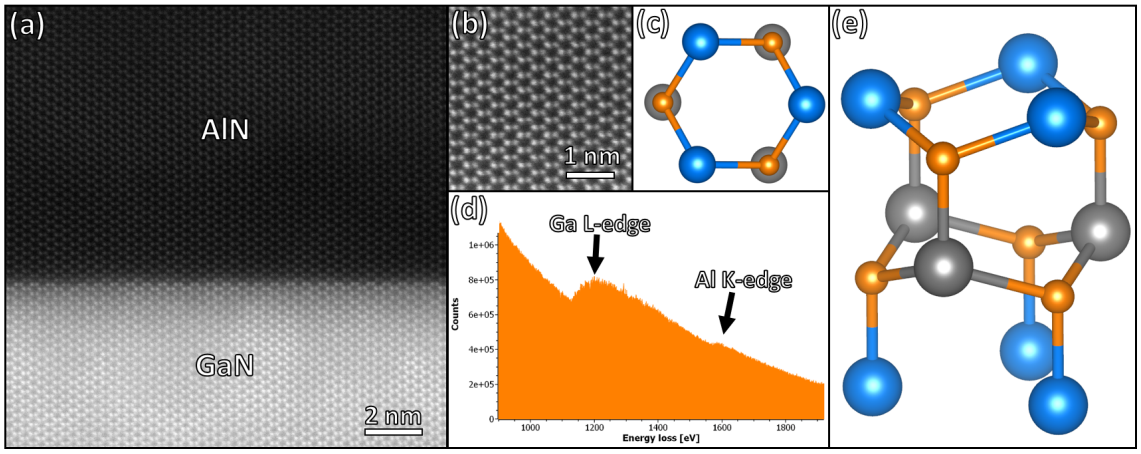

Figure 4.15: In the AlN and GaN layers depicted in (a) in [0001] ZA, an ordering is observed, which can be better seen in the zoom to the nominal GaN layer depicted in (b). It seems consistent with an ordering of Al and Ga as sketched in (c). EELS data (d) reveals that indeed Al is present in the GaN layer. The reduction in symmetry of the crystal gives rise to a polarization in the c-plane if the crystal is deformed within this plane. When observing the model from another angle, it is obvious that it implies that alternating c-planes exhibit differences in occupation.

To understand these results, a model of the structure based on HR-HAADF and electron energy loss spectroscopy observations is shown in Fig. 4.15. In the HAADF image shown in (a), which depicts an interface region between AlN and GaN, unexpected contrasts differences of atom columns within the honeycomb structure of the [0001] ZA are visible. In a magnified area that is given in (b), the symmetry reduction of the structure becomes obvious. Normally, all columns of GaN or AlN should have the same contrast in [0001] ZA. To validate that the difference in HAADF intensity of the columns is really linked to the chemistry, EELS is performed on the GaN layer away from the interface. The spectrum shown in (d) exhibits, besides the Ga L-edges (L_3 at 1115 eV and L_2 at 1142 eV), the Al K-edge (1560 eV) proving that the nominal GaN is in fact AlGaN. Therefore,

the model depicted in (c) with Ga-rich (blue) and Al-rich (gray) sublattices seems to be realistic. When observed from the side it becomes clear that this model implies different occupancies of Al and Ga on alternating c-planes. This is not far-fetched and has in fact been observed in different wurtzite III-nitrides in the framework of this thesis and in literature.

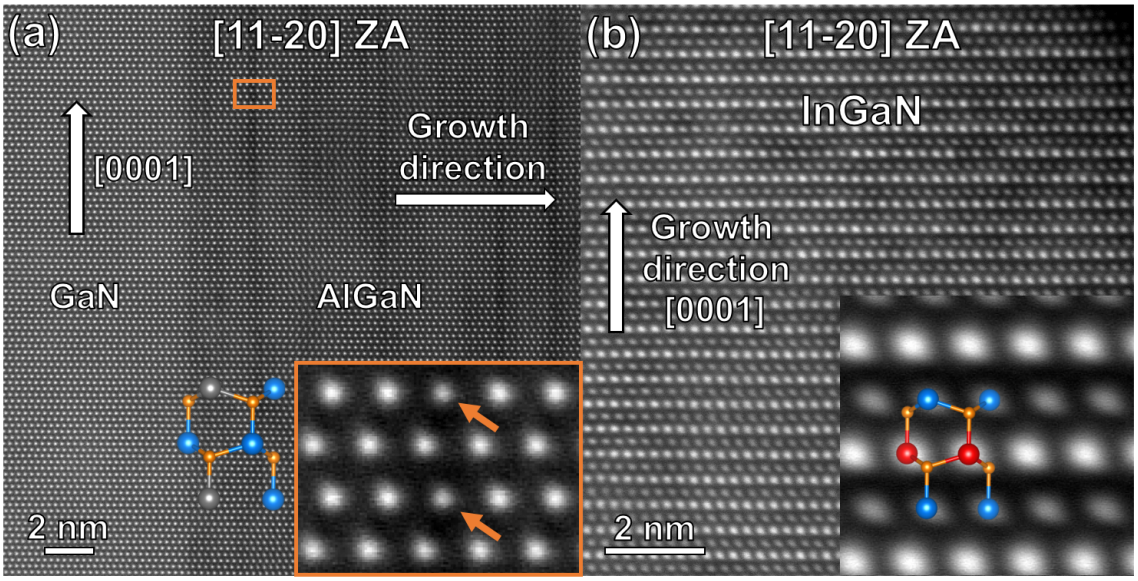

Figure 4.16: Ordering of elements on alternating c-planes observed in AlGaN and InGaN: Rows of atom columns running in [0001] direction that exhibit higher Al content in AlN are shown in (a) and a very regular ordering of whole c-planes observed in InGaN (b). Both examples imply a similar ordering as observed in the AlN/GaN sample in [0001] ZA.

Fig. 4.16 (a) shows an m-plane AlGaN/GaN sample used for THz generation via inter-subband transitions. Dark lines in c-direction indicate Al enrichment that is compatible with the model as shown in the inset. The HR-HAADF image depicted in (b) shows a very clear ordering observed in InGaN NWs. The findings are part of two journal articles [139, 140]. Ordering in InGaN was already described in the literature by Woo et al. in 2015 [141]. All these orderings lead to a deviation from the symmetry normally observed in [0001] ZA, similar to what is shown in Fig. 4.15.

Therefore, the field measurements shown in Fig. 4.14 seem to have a comprehensible origin in the reduction of crystal symmetry. In combination with the deformation of the materials, a polarization field should exist and its gradient leads to the measured electric fields. The fields qualitatively match the observed crystal deformations, however the situation here is complex because the local composition (ordering) is also changing, meaning that the piezoelectric constants are changing. More data and analysis is needed to quantitatively understand the ordering and its polarization field in a-plane (and possibly in m-plane) wurtzite type III-nitrides. Nevertheless, the synchronous strain and field

mapping at nanometer resolution by means of NPED proves to be an extremely powerful technique, especially for the characterization of piezoelectric materials.

4.6 Inversion Domain Structures in GaN Nanowires

The growth of the GaN NWs that are observed in this section, as well as the μPL measurements, was done by Thomas Auzelle in the group of Bruno Daudin at CEA-INAC Grenoble. PIPS sample preparation was performed by Catherine Bougerol from CEA-INAC / Institut Néel in Grenoble. Plane view tripod samples were prepared by Nicolas Mollard (CEA-INAC Grenoble) and by the author with help from Nicolas Mante from CEA-LETI Grenoble. The micro-wires (μWs) were grown in the group of Joël Eymery (CEA-INAC Grenoble). They were prepared by FIB milling by David Cooper from CEA-LETI Grenoble. The results presented in this section have also been the basis for several publications [142, 143, 144, 140, 145] and an image has been chosen as the cover of Journal of Materials Research focus issue 'Aberration Corrected Transmission Electron Microscopy' (vol. 32 no. 5), which can be found in the back matter of the thesis.

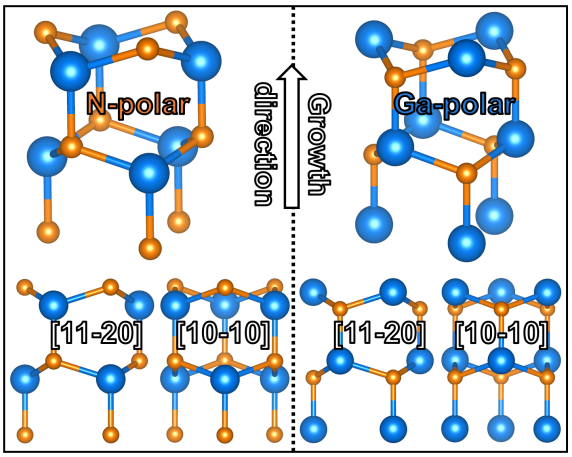

Figure 4.17: Definition of Ga-polarity and N-polarity of GaN crystal, as seen from different ZA.

GaN is an important material of the semiconductor industry and basically all LEDs for white light illumination purposes are based on GaN. Yet, the material is still not perfectly understood and the goal of this analysis is to address a few of the open questions, especially concerning polarity and inversion domains.
NWs are being used for two reasons. Firstly, because they are a promising material for application as they can be grown free of dislocations due to their ability to relieve strain through surface relaxation [146, 147]. Secondly, they are a model system that can be

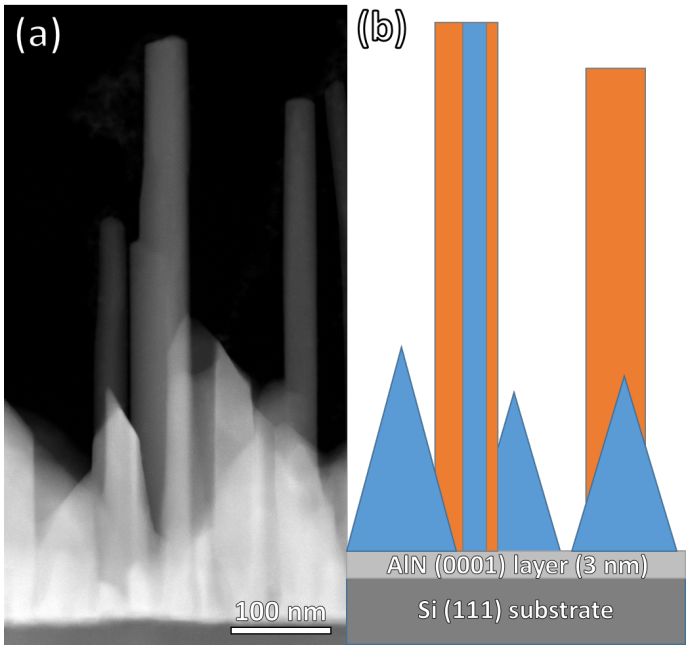

Figure 4.18: Overview HAADF image of the GaN NW samples (a) and schematic drawing (b) explaining the general morphology and structure: GaN pyramids and NWs grow on the (non-wetting) thin AlN layer on Si (111) substrate. Pyramids are Ga-polar (blue) while NWs are either only N-polar (orange) or have a Ga-polar core and a N-polar shell. The polarities are established in the course of this section.

used to study general properties that are harder to observe in bulk. This is demonstrated via correlative measurements that link IDBs to µPL features.

The polarity (cf. 4.17) is an important property of GaN, due to its lack of inversion-symmetry. It determines the atomic species present at stable facets and therefore has an influence on growth, e.g. for dopant incorporation. Additionally, it defines the direction of the spontaneous and any piezoelectric polarization of the material (cf. Sec. 4.5).

There are many studies of the polarity of GaN NWs, but even for the same substrate (in the following case a thin AlN(0001) layer on Si(111), as shown in Fig. 4.18), and similar growth conditions different polarities have been reported using different techniques that do not offer atomic resolution (mostly CBED) [148, 149, 150, 151]. Either N-polar NWs, Ga-polar NWs or both types were reported in these systems. To clarify the situation, HR-ABF is performed.

Two different types of NWs can be observed in the samples, one of which exhibits an area of different contrast within the wire that is running parallel to the sidewalls while the other kind is uniform (see Fig. 4.19). It is established below that the contrast originates from an ID within the NW. This contrast can be observed best in ABF, in HAADF it is

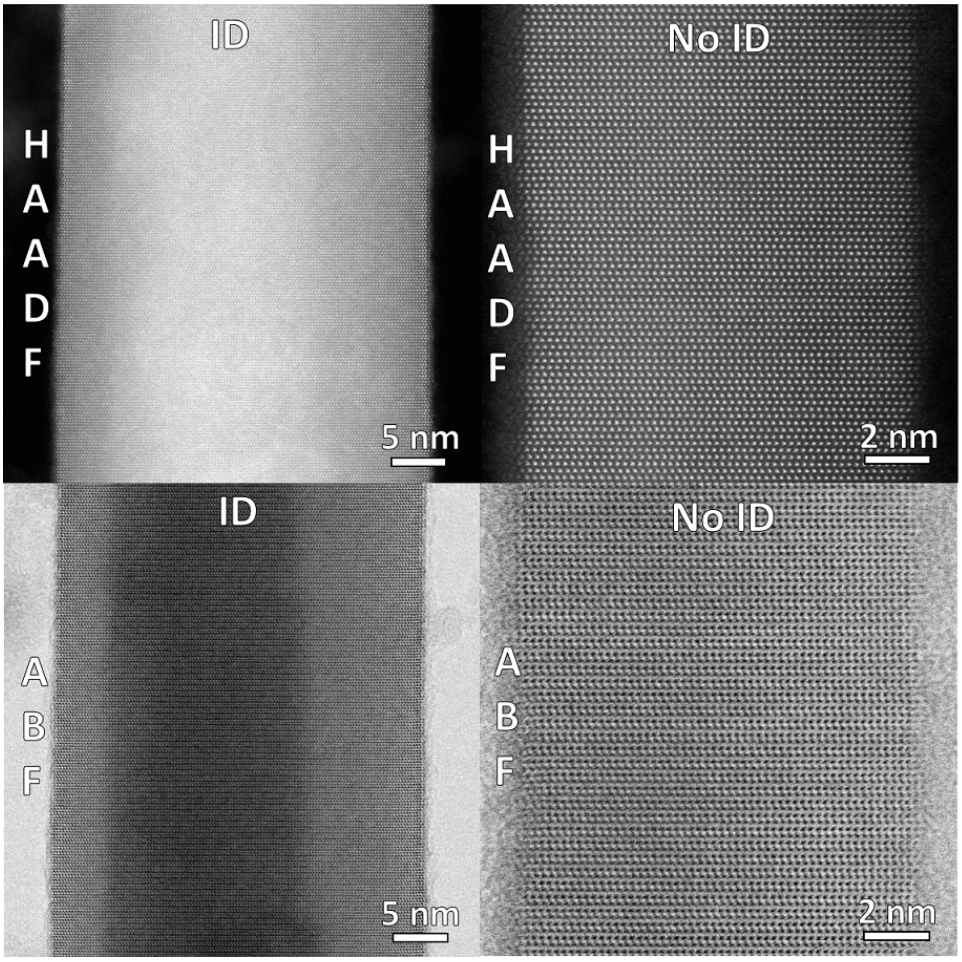

Figure 4.19: Comparison of the two types of NWs (with and without ID) as observed in HAADF and ABF. The visibility is clearly better for ABF due to its partly coherent nature.

rather faint. The reason for this is that the only additional HAADF contrast stems from dechanneling at the boundaries between the domains while the partly coherent nature of ABF leads to a stronger contrast from interference.

As the contrast appears always within the NW (never touching the edges), it must stem from a structure engulfed by the host crystal. This complicates the situation, because the structure can only be observed in projection with the shell structure, except for in plane-view geometry.

One example of a NW prepared in plane-view geometry and imaged by HR-HAADF (along the [0001] ZA) is given in Fig. 4.20. All the NWs observed exhibited the same uniform lattice as depicted, without a different structure anywhere within the NW. As the ratio of occurrence of the two different types in the samples is around 1:1 and about a dozen NWs were observed, this means that the two structures seem to be identical

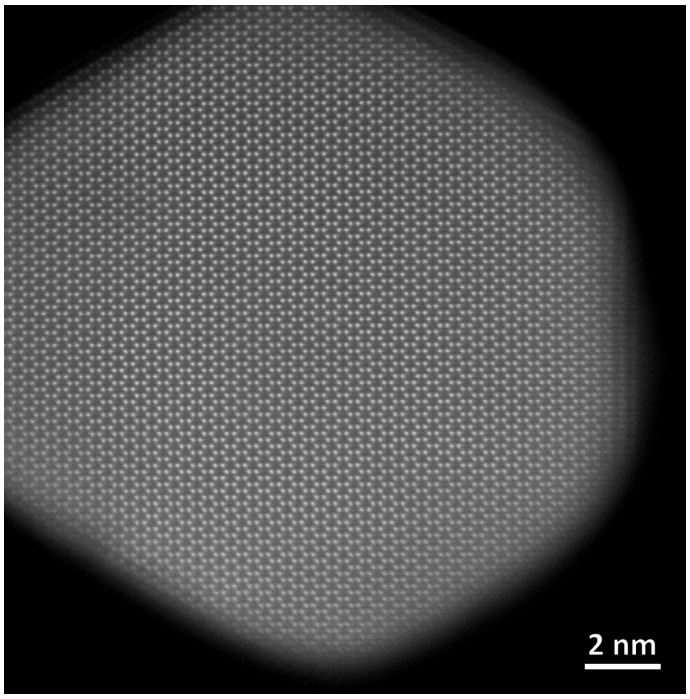

Figure 4.20: Representative plane-view HR-HAADF image of a GaN NW. No change of structure can be observed within the wire, meaning that the projected structure in [0001] ZA is equivalent to the shell.

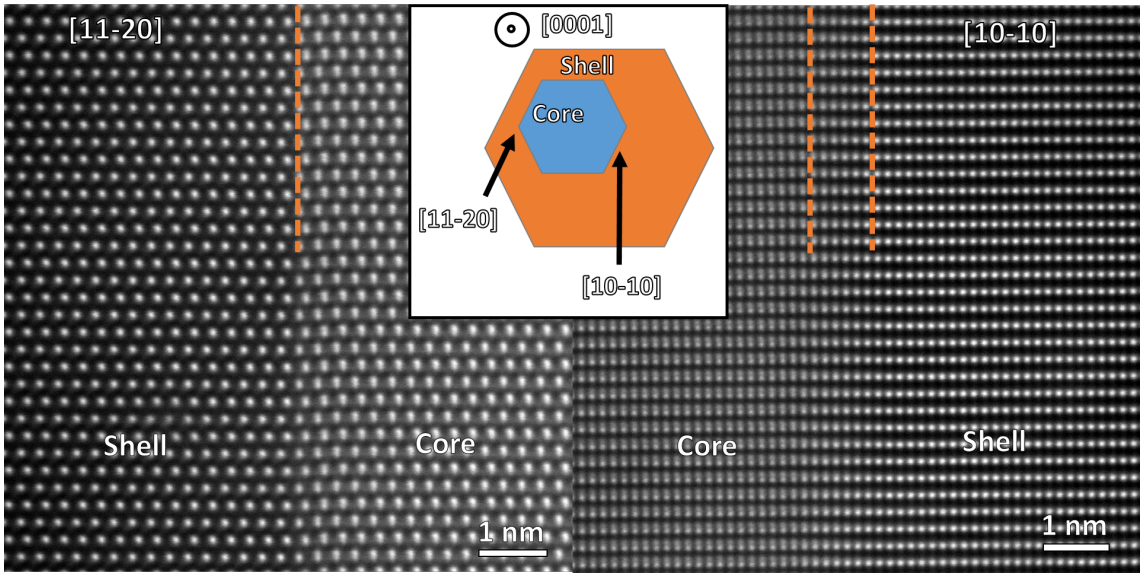

Figure 4.21: Core-shell inversion domain structure observed in $[11\bar{2}0]$ ZA on the left-hand side and in $[10\bar{1}0]$ ZA on the right-hand side. The sketch in the center shows a core-shell configuration in plane-view with the two observation zone axes indicated. The sharpness of the domain in the two projections is different (indicated by the orange dotted lines) due to the shape of the core.

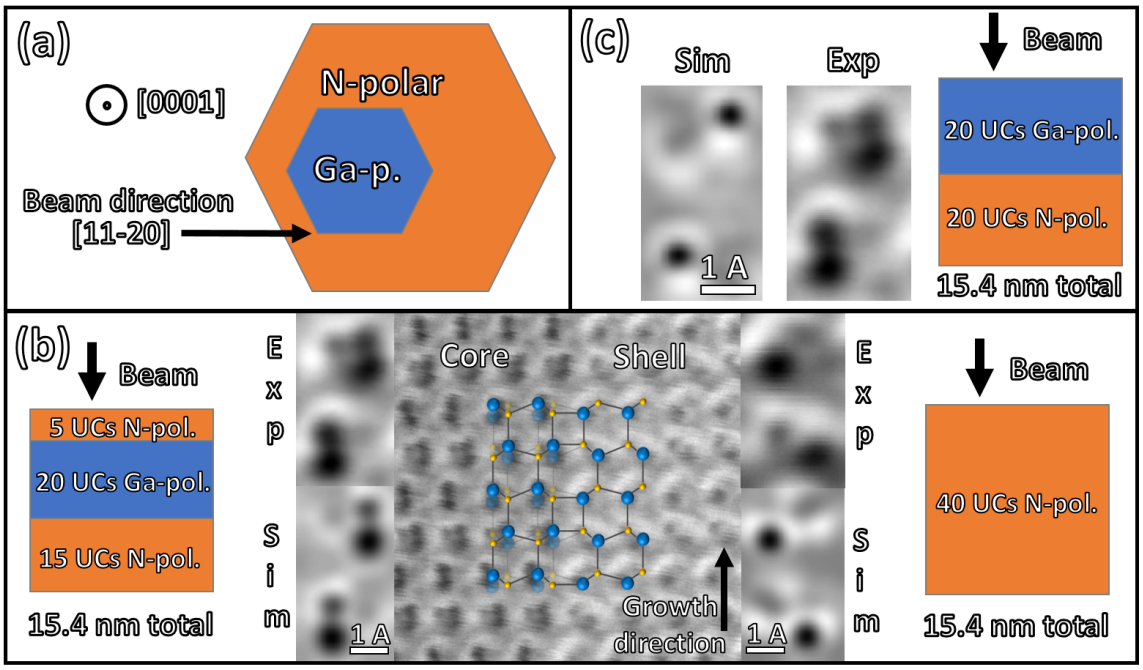

Figure 4.22: (a) Plane-view sketch of the observation geometry and according simulation; the edge of an ID in a NW is imaged in $[11\bar{2}0]$ ZA at 300 kV with a convergence angle of 20.9 mrad and detecting from 7.1 mrad to 17.6 mrad. (b) Experimental ABF image with superimposed ball and stick model of the projected configuration in the center. To the left and right the experimental data (template-matched) and simulation results for the given configuration of core-shell-core and only N-polar domain is shown, respectively. (c) Alternative simulation missing the top N-polar shell (yet same total thickness) yielding very different contrast.

when observed in [0001] zone axis. The result is in agreement with domains of different polarity and yields information about the type of boundary between the domains.

When observed in $[11\bar{2}0]$ and $[10\bar{1}0]$ zone axes by means of HAADF (see Fig. 4.21), the structure looks indeed like a superposition of the two domains, leading to dumbbells from the Ga columns of the two polarities.

For a definitive proof of the core-shell ID structure, ABF is performed at the border between core and shell in $[11\bar{2}0]$ projection and compared to simulation. A sketch of the experiment is shown in Fig. 4.22 (a). The obtained ABF image is depicted in the center of (b) with averaged cut-outs (by TeMA) of the two sides and according simulation results for the structures depicted next to them. The parameters of the experiment are a beam energy of 300 kV, a convergence angle of 20.9 mrad and a detection from 7.1 mrad to 17.6 mrad. The calculations are absorptive potential based simulations using Kirkland's TEMSIM code. They were iteratively performed to obtain a close match to the experimental data with the starting parameters being the width of the NW as total thickness and the width of the core as initial core thickness. After 25 simulations a

good agreement between simulation and experiment was obtained. The sensitivity of ABF is demonstrated in (c) where the same thickness of material but only a two domain stack is simulated. The result is strikingly different, validating the possibility to obtain three-dimensional information of complicated structures containing light elements from single ABF images.

With the knowledge that the structure present within the NWs is an ID, it is possible to determine the polarity of core and shell more easily by evaluating the position of the dumbbell in the core region with respect to the lattice of the shell. It turns out that the shell is always N-polar while the core is Ga-polar.

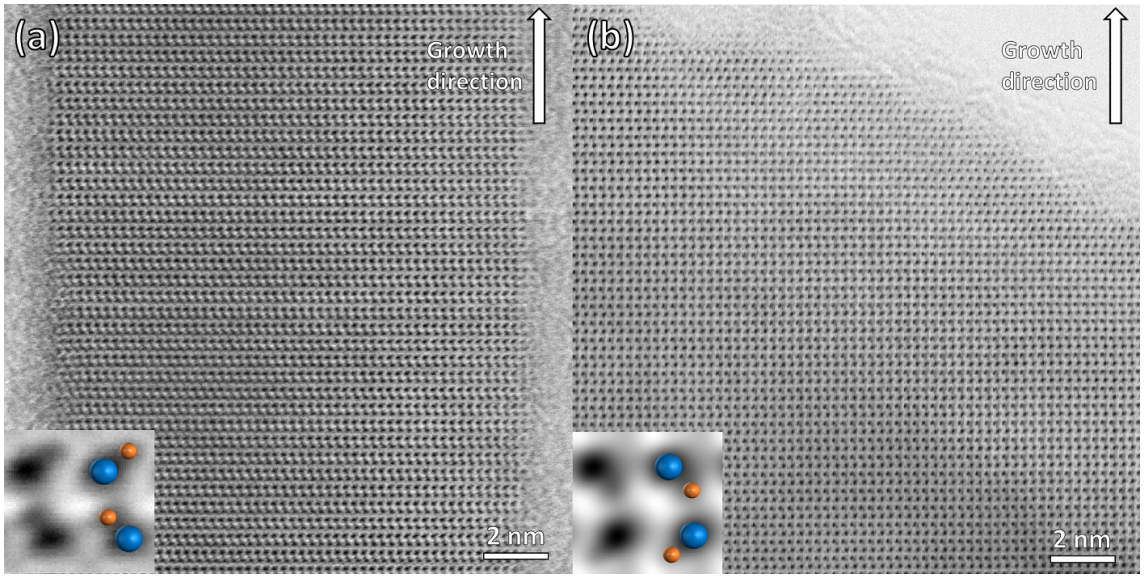

Figure 4.23: Polarity determination by ABF of NW without ID (a) and for a pyramid structure (b). The insets are averages from template-matching. The N-polarity of the NW without ID and the Ga-polarity of the pyramid structure depicted here is representative for the samples.

Fig. 4.23 (a) depicts a NW without core and the polarity for this type is always, as depicted, N. A pyramid depicted in (b) is also representative of the samples in general and exhibits Ga-polarity. Hence, the general picture of morphologies and resulting polarities is as given in Fig. 4.18 (b). It can be concluded that Ga-polar material has the tendency to grow in the shape of pyramids while the N-polar GaN is growing vertically under the given growth conditions. The encapsulation of Ga-polar GaN by N-polar material "drags" it vertically, leading to the core-shell ID structure. How the Ga-polar material is engulfed in the first place during nucleation is not clear.
A further validation of the stability of the core-shell structure is given in Fig. 4.24. HAADF and ABF images of an unusual NW with several contrasts are depicted in (a)

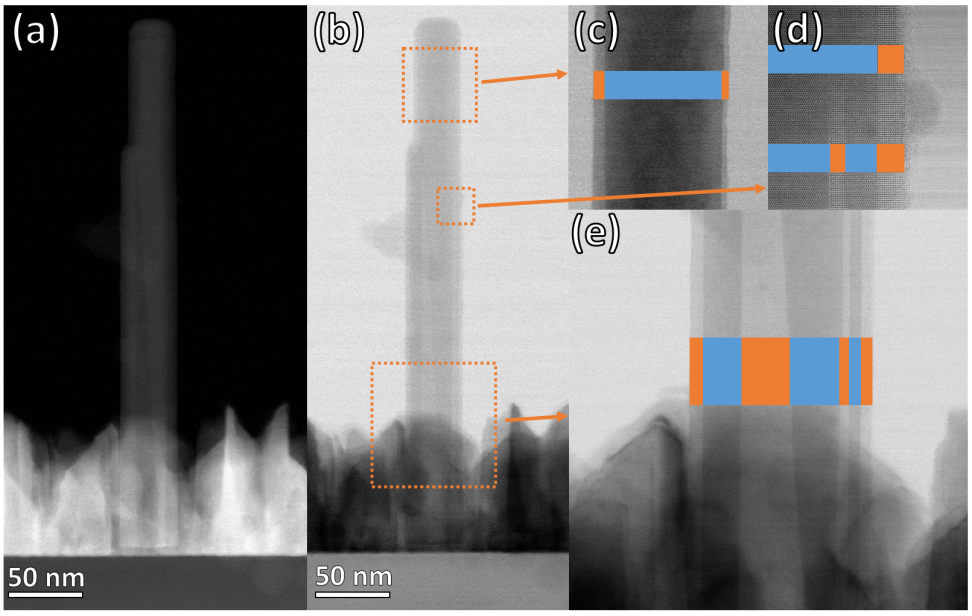

Figure 4.24: HAADF (a) and ABF (b) images of a peculiar NW that has multiple polarities at the beginning. (N.B.: The socket of the NW is better observed in the HAADF while the ABF makes it easier to see the domains.) The polarities are displayed in blue (Ga) and orange (N). A zoom to the lower part is given in (e) where the N/Ga/N/Ga/N/Ga/N polarity configuration can be seen. The N-polar domains within the NW close while growing (d) and finally the typical N/Ga/N configuration is obtained at the top (C).

and (b), respectively. An ABF close-up of the base, shown in (e), reveals the multiple cores. The N-polar sections within the NW terminate slowly when following the growth direction. The end-point of a N-polar insertion is shown in (d) and the top part of the NW exhibits the typical core-shell structure with N-polar regions at the edges and a Ga-polar core. Obviously, the exception proves the rule.

The only ubiquitous type of extended defects found in NWs are SFs, because the large surface-to-bulk ratio prevents other defects by means of strain relaxation. The interaction of such a defect with the core-shell ID structure is depicted in Fig. 4.25: a SF starting in the core effects a misalignment of plane stacking between the core and shell, as the sequence is changed to A-B-C while the shell continues A-B-A. This can be seen as a horizontal line of blurry contrast in the core region. The next layer is aligned again as the shell continues A-B-A-B and the core with A-B-C-B, thus both have the B stacking and the contrast of this layer is clear again. Afterwards, the shell introduces a SF and goes to A-B-A-B-C, thus avoiding the misalignment that would happen again at this point again and instead leading to an aligned sequence for the rest of the NW.

Correlative STEM/μPL measurements are performed to understand the influence of IDs on the luminescence of GaN. For this purpose, NWs are dispersed on a thin (around 50 nm) amorphous silicon nitride membrane with markers and an overview image obtained in

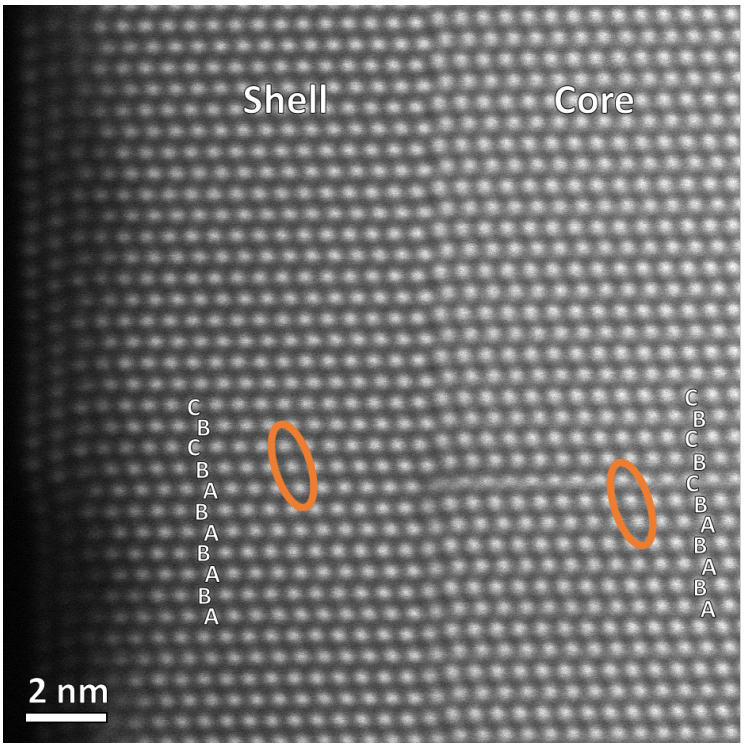

Figure 4.25: A stacking fault in the core (orange ellipse on the right) changes the plane order so that a superposition of the different sequences in core and shell produces a line of blurry contrast in the region to the right. Three layers afterwards, the shell incorporates a SF (orange ellipse on the left-hand side) to avoid another misalignment.

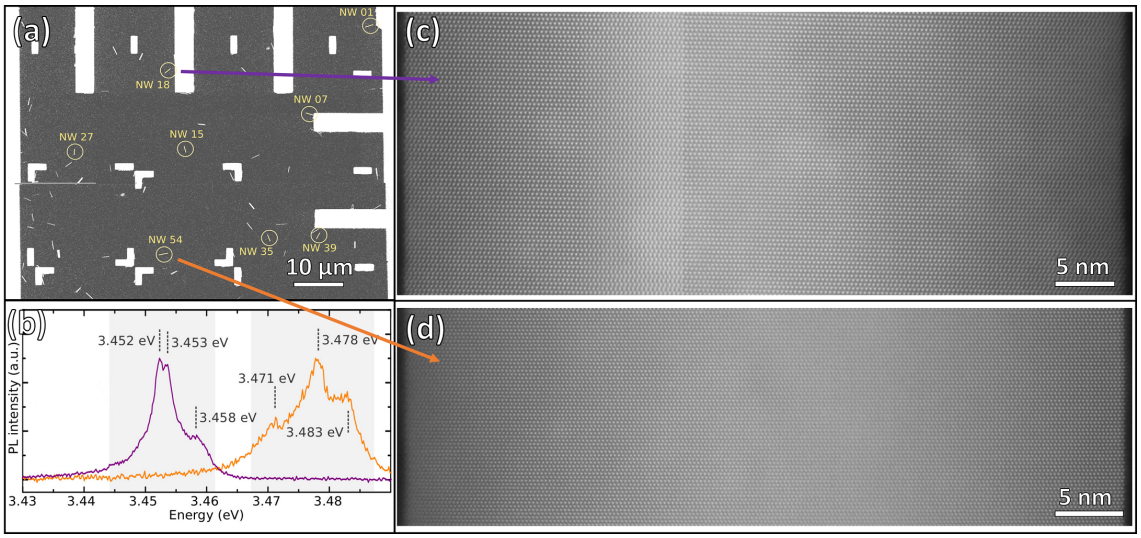

Figure 4.26: Correlative STEM and µPL measurements of individual NWs: in (a) the silicon nitride membrane with markers and dispersed NWs (SEM image) is shown, (c) and (d) depict the HAADF characterization and (b) the corresponding µPL measurements of the marked NWs. Exclusive 3.45 eV luminescence is demonstrated for the NW containing the ID, while the luminescence of the defect free NW is from the 3.47 eV bandgap.

a scanning electron microscope (SEM), as depicted in Fig. 4.26 (a). Next, μPL spectra are obtained of individual NWs (cf. (c)) and their position is marked. Subsequently, the NW positions are retrieved in the STEM and the structure is investigated by mean of HR-HAADF to determine if a ID is present, as shown for two examples in (b).
The result is that NWs without IDs exhibit PL emission at the typical 3.47 eV (NW marked in orange in Fig. 4.26), while NWs with IDs luminesce exclusively at 3.45 eV (purple). Two conclusions can be deduced: IDs are the origin of 3.45 eV emission, which is also observed in bulk, and the lack of 3.47 eV emission for NWs exhibiting IDs means that the ID is effectively trapping all the carriers generated within the NW. This allows to determine a lower boundary of the trapping distance of the ID: the maximum width of the NWs, here around 80 nm. The exclusive emission from either 3.45 eV or 3.47 eV for the two types facilitates a statistical analysis of the occurrence of both types only by SEM and μPL: bundles of NWs are imaged in SEM and the number of NWs is counted. Subsequently, the PL spectrum of the whole bundle is analyzed and grouped into "only 3.45 eV", "only 3.47 eV" or "mixed". The probability of the occurrences follows a binomial law which allows for the determination of the probability for an ID in a NW. The probability is determined to be around 50 % for the investigated sample. More information ca be found in the article [142].

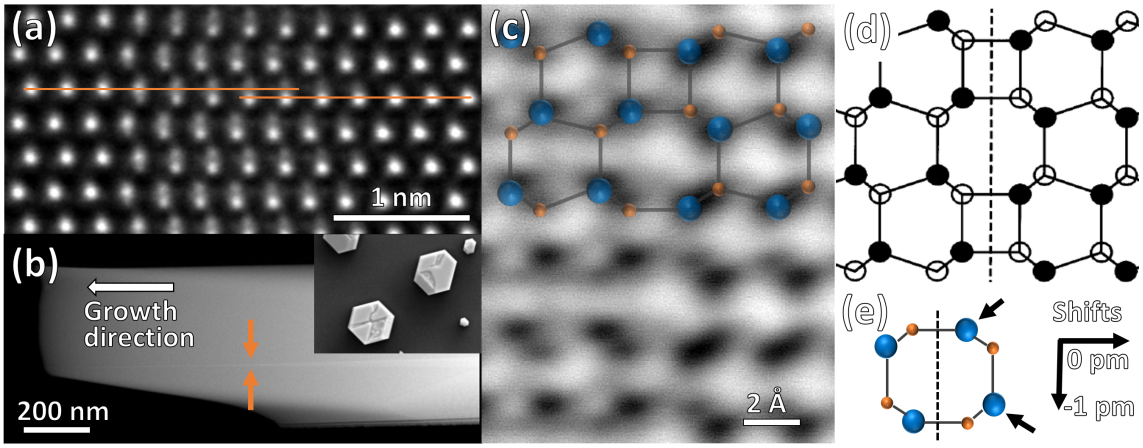

Figure 4.27: The seemingly wider spacing of Ga atom columns of superposed GaN domains in projection is demonstrated in (a) (cf. Sec. 3.1.1. A FIB prepared GaN μW with IDB is shown in (b). The inset depicts the KOH etched wires, thus revealing the domains. An ABF image obtained from a clean IDB is given in (c) and compared to the IDB* model from Northrup et al. [152] in (d). The shifts of the marked Ga positions that are predicted from the model are shown in (e).

A next step in understanding GaN IDBs is to measure the structure of the defect quantitatively. One fundamental problem in doing so for core-shell type IDBs is pointed out in Sec. 3.1.1: positions of atom columns that are truncated within the crystal can strongly

differ from intensity maxima in the corresponding HAADF image. This effect can be observed in Fig. 4.27 (a) where a kinking IDB is imaged, exactly as sketched and simulated in Fig. 3.10. Even by the naked eye it is clear that in the region of overlapping domains, where the dumbbells appear, the two Ga columns seem to push each other apart, protruding over the orange lines that connect the columns within each domain. Therefore, a 'clean' inversion domain boundary without superposition is needed. To facilitate this, slightly KOH etched μWs were provided by Joël Eymery and FIB-prepared by David Cooper. A resulting NW, exhibiting an IDB, is shown in (b) with the growth direction pointing to the left. The advantage of this method is that due to the selective etching, the IDs are revealed in SEM (cf. inset of (b)) and the NWs can be chosen, orientated and milled to reliably obtain a targeted preparation of an IDB.
To evaluate the structure of IDBs qualitatively, a ball-and-stick model of the IDB* model of Northrup et al. [152], as shown in (d), is superposed to an experimental ABF image (c). The IDB* model corresponds to a cut of a perfect GaN crystal along a $[10\bar{1}0]$ plane with subsequent shift of c/2 along the c-axis. This model was also used for the simulations shown in Fig 4.22 and agrees also with the plane-view images that show no additional columns (cf. Fig. 4.20). Quantitatively, Northrup et al. found only a small deviation of the relaxed model (by means of local density approximation calculations) compared to the input structure described above. The close Ga-planes from both sides are contracted by only about 1 pm (cf. (d)). Recently, Labat et al. performed coherent Bragg imaging on GaN μWs and found an 8 pm shift of the close Ga-planes [153].
To investigate the shift of IDs at atomic resolution, the positions of Ga columns across an IDB are measured from registered images series (Zorro) via TeMA and the result is shown in Fig. 4.28 (a). When crossing the IDB from reference position 'R', a shift of +7.0 pm is found and a stretch of 9.9 pm with an error of 1.5 pm. It should be noted that the shift is not perfectly abrupt because the IDB is not straight and the column marked as '2' is a superposition of the two domains (although only a small fraction of the N-polar domain is in projection).
Another way to determine a shift between the two domains is depicted in (b). Here, the lattice of both sides of a kinking IDB is determined with TeMA as described in Sec. 3.1.1. Afterwards, the two lattices are translated to the center by multiples of the measured lattice parameters and the deviation of their origins is measured. The result has a high precision due to the use of dozens of positions, but the accuracy from superposing the two lattices has not been determined. A shift of +7.9pm and a no stretch within the measurement accuracy is found.
Density functional theory calculations performed by Frédéric Lançon et al. [154] (manuscript in preparation) found the result from Northrup et al. as a local energetic minimum with

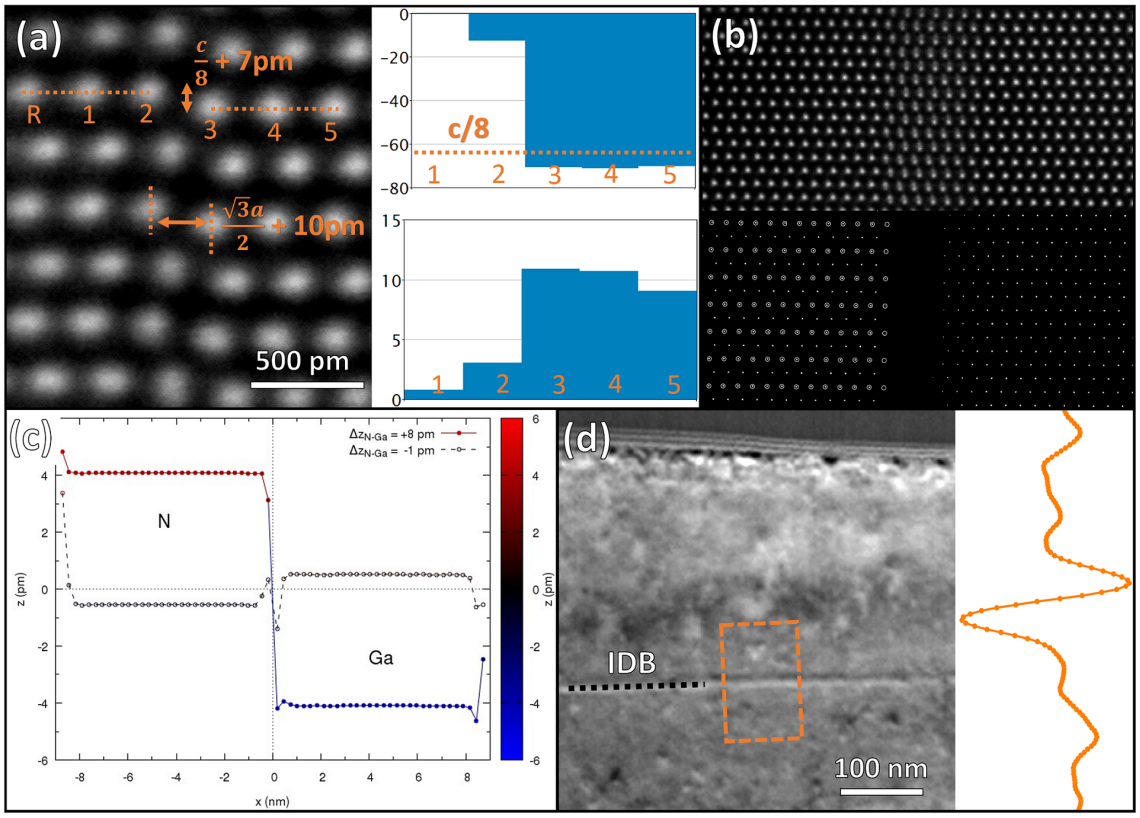

Figure 4.28: (a) Quantitative structure of IDB from atom positions: +7 pm shift and 10 pm stretch are found. (b) Using TeMA to determine the lattices of both sides of an IDB for comparison. (c) DFT simulations from Lançon et al. (unpublished), finding a +8 pm shift. (d) Qualitative DPC measurements showing a field at the IDB.

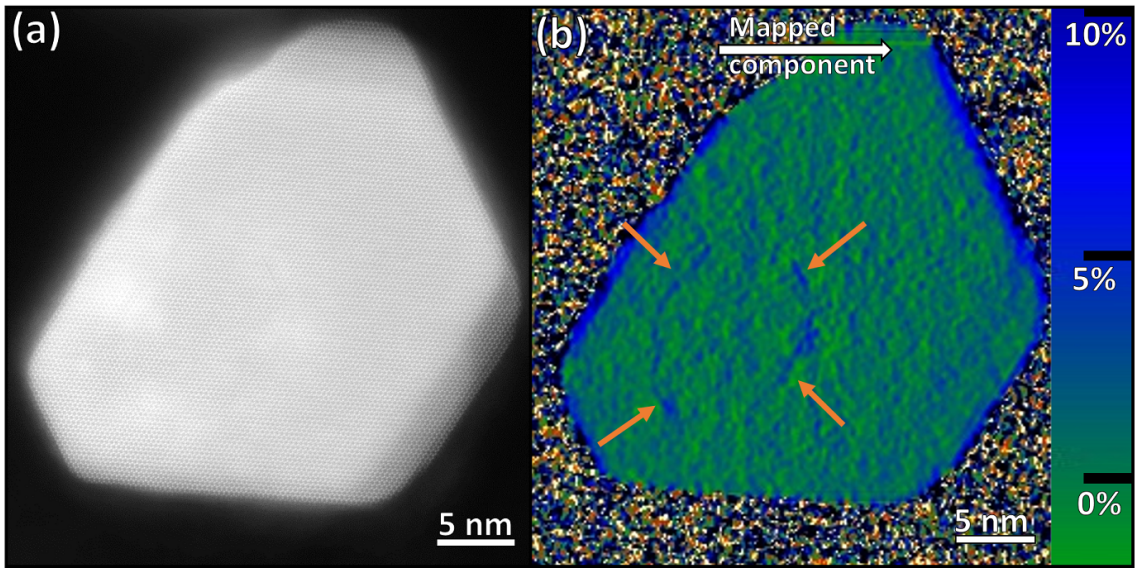

Figure 4.29: Plan-view HR-HAADF image of a GaN NW in (a) and corresponding GPA map in (b) with the mapped component indicated by the arrow, demonstrating strain at the IDB. The hexagonal outline of the ID can be seen in the map and also faintly in (a).

the most stable solution being an +8 pm shift of the Ga-planes (cf. (c)). In addition to solutions with almost no stretch, a +10 pm stretch was also found for different starting conditions.
A further experimental confirmation of a stretch is depicted in Fig. 4.29. GPA of a NW in plan-view geometry reveals a core of roughly hexagonal shape with positive strain at the interfaces. Although around twenty NWs were investigated in plane-view, strain contours at the core were only found twice (with a probability for an ID in the NW of around 0.5). Therefore, it might be possible that several IDB structures exist in the material and even in the same sample. However, the shift in c-direction of around 8 pm seems to be common.
As an outlook of what should be a logical next step of the characterization of IDBs in GaN, a qualitative DPC experiment is shown in (d). Due to the sample quality, the thickness gradient and the presence of a kink, a quantification is not attempted. Nevertheless, an electric fields seems to be present at the IDB. This is not very surprising, as the effectiveness of charge carrier trapping of the defect was demonstrated above. However, a quantification of the fields and comparison to simulations should prove useful for the understanding of GaN.

5 | Conclusion and Outlook

In the framework of this thesis, different quantitative scanning transmission electron microscopy techniques have been improved or developed and afterwards applied to a variety of materials science problems. Two patent applications, a number of peer-reviewed journal articles and two journal covers underline the success of this enterprise.

The techniques are grouped into methods to determine strain, to quantify contrasts and to map (electric) fields.

In the first category, strain measurements by means of high-resolution imaging, by scanning moiré fringes and by nano-beam precession diffraction were developed.

For high-resolution strain measurements, the combination of a new rigid-registration algorithm for image series together with a template-matching based code has been proven to be able to measure atom positions with one picometer precision. The unreliability of atom positions determined from intensity maxima in high-angle annular dark field images for the case of truncated atom columns was established by means of electron scattering simulations.

The scanning moiré fringe technique for strain measurements was extended to two dimensions for arbitrary crystals and zone axis by means of tweaking the scanning pattern of the probe to lead to a square moiré pattern. This technique is a kind of compressed sensing and can map strain very precisely over a large field of view.

Nano-beam precession diffraction was improved by accurately taking the beam width into account for strain maps. This was facilitated by comparing the size of an interface from HAADF with the width obtained from virtual images that are created from the NPED data.

In the domain of contrast quantification it was demonstrated how to measure the beam current and the detective quantum efficiency of a scintillator based annular detector without special knowledge about it. Contrast quantification for annular bright field was assessed experimentally and by means of simulations. The partly coherent nature of

this imaging mode poses some problems but the quantification of compositions for light elements should be possible for certain systems.

Differential phase contrast was compared to (off-axis) electron holography to understand the differences and similarities of these techniques concerning the mapping of electric fields. By performing both on the same in-situ biased p-n junction, a direct comparison of the sensitivities of these techniques could be established. A method to quantify the DPC signal was proposed.

Nano-beam precession diffraction field mapping was introduced. This new technique, for which a patent was filed, allows to quantify (electric) fields and strain at the same time. By combining precession and template-matching, a very robust technique to measure fields is established that avoids many problems that can arise in other methods.

The developed techniques were applied to several material systems. The interface chemistry of ZnTe/CdSe based solar cell structures was inferred by means of high-resolution strain measurements and validated by atom probe tomography results.

Faint strain gradients in topological insulator HgTe/CdTe were assessed by means of nano-beam precession diffraction and compared to calculations of the extension of the wave function of surface states in the material. The influence of the beam size was taken into account and the relaxation of strain was included utilizing finite element simulations.

Strain in a SiGe transistor in [110] zone-axis was measured by scannin moiré fringes. The large field of view of the method and the relatively high strain precision allowed to map the deformations in this device.

Nano-beam precession diffraction was applied to a-plane AlN/GaN. Piezoelectric fields stemming from an intermixing and ordering of Al and Ga were demonstrated. The influence of individual dislocations on strain and fields is observed in the acquired maps.

Core-shell type inversion domain structures in GaN were discovered and evidenced for the first time. The relationship between inversion domains and optical properties was established by means of correlative experiments. The exact atomic structure was evaluated and compared to old and new ab-initio simulations. Electric fields were found at inversion domain boundaries.

The results obtained lead to a plethora of potential future applications and possible improvements or combinations with other techniques. Adding precession to DPC, which is also described in the first patent that was filed, might overcome problems related to dynamical scattering while keeping the method fast and relatively simple.

It should prove interesting to use NPED to map magnetic fields and to compare it to established techniques. Adding even more functionality to NPED is being investigated and also part of the second patent application.
Measuring strain from high-resolution HAADF images could be a way to determine the local Li content in Li_2MnO_3 layered oxides. As the Li layers are depleted, the O layers are facing each other and repel, therefore increasing the spacing of Mn layers substantially, which could be assessed by HR-HAADF based strain measurement at low dose, compared to spectroscopy. This would finally allow to determine Li content even for typical particle sizes from real batteries where quantification of ABF contrast has been shown to be problematic.
For the case of inversion domains in GaN the preliminary field measurements should be continued and compared to simulations of the according structure. This should prove invaluable for the understanding of charge carrier recombination in GaN where this defect is common, even for nano-wires, and effective in trapping charge carriers and recombining them radiatively, as demonstrated.

A | Statistics of Multi-Stage Detector Processes

For a statistic process in which e.g. an incoming electron is converted into Λ photons, the number of photons Γ and its variances for N electrons can be expressed, according to Mandel [155], as

$$\begin{aligned} \overline{\Gamma} &= \overline{\Lambda}\,\overline{N} \\ \overline{\Delta\Gamma^2} &= \overline{\Lambda}^2\,\overline{\Delta^2 N} + \overline{N}\,\overline{\Delta^2\Lambda}\ . \end{aligned} \tag{A.1}$$

The bar denotes the mean and Δ the deviation from the mean. These expressions are independent of the probability distributions of N and Λ (a derivation is given in Mandel's original article [155]).

Browne and Ward used this expression to describe the multi-stage process of a Poisson distributed beam impinging on a scintillator based STEM detector [30] and this is sketched here.

For the case of typical beam energies in STEM hundreds of photons are created per incident electron leading to the approximation that

$$\overline{\Delta^2\Lambda} \ll \overline{\Lambda^2} \quad \rightarrow \quad \overline{\Gamma} \approx \overline{N}\,\overline{\Lambda}\ . \tag{A.2}$$

Taking into account that only a fraction η of the photons make it to the photomultiplier, the mean number of photons arriving at the photo-cathode is

$$\Pi = \overline{N}\,\overline{\Lambda}\,\overline{\eta}\ , \tag{A.3}$$

and its variance

$$\overline{\Delta^2\Pi} = \overline{\eta}^2\overline{\Delta^2\Lambda} + \overline{\Lambda}\,\overline{\Delta^2\eta} = \overline{N}\,\overline{\Lambda}(\overline{\eta}^2\,\overline{\Lambda} + \overline{\Delta^2\eta}\,. \tag{A.4}$$

As individual photons either make it to the photo-cathode or not, they follow a binomial distribution with $\overline{\Delta^2\eta} = \overline{\eta}(1-\overline{\eta})$ and thus

$$\overline{\Delta^2\Pi} = \overline{N}\,\overline{\Lambda}\,\overline{\eta}(\overline{\eta}\,\overline{\Lambda} + 1 - \overline{\overline{\eta}})\,. \tag{A.5}$$

Next, the conversion of photons into electrons at the photo-cathode needs to be considered. Due to its energy a photon can at most generate one photo-electron. Therefore, the process is again described by a binomial distribution. For the conversion probability ς and thus Ξ photo-electrons being generated by Π photons, the mean and variance are

$$\begin{aligned}\overline{\Pi} &= \overline{\Pi}\,\overline{\varsigma} = \overline{N}\,\overline{\Lambda}\,\overline{\eta}\,\overline{\varsigma}\\ \overline{\Delta^2\Xi} &= \overline{\varsigma}\,\overline{\Delta^2\Pi} + \overline{\Pi}\,\overline{\Delta^2\varsigma}\\ &= \overline{\varsigma}^2\overline{N}\,\overline{\lambda}\,\overline{\eta}(\overline{\eta}\,\overline{\Lambda} + 1 - \overline{\eta}) + \overline{N}\,\overline{\Lambda}\,\overline{\eta}\,\overline{\varsigma}(1-\overline{\varsigma})\,.\end{aligned} \tag{A.6}$$

The factor $\overline{\Lambda}\,\overline{\eta}\,\overline{\varsigma}$ describes the mean number of generated photo-electrons per incident beam electron on the detector and is replaced by $\overline{n}$. With this we can write

$$\overline{\Delta^2\Xi} = \overline{n}\,\overline{N}(\overline{n} + 1 - \overline{\eta}\,\overline{\varsigma})\,. \tag{A.7}$$

As the conversion factor of the photo-cathode $\overline{\varsigma}$ is around 0.2 [30] and the probability of a generated photon to reach the photo-cathode $\overline{\eta}$ is very small, the term $\overline{\eta}\,\overline{\varsigma}$ is negligible compared to $\overline{n}+1$ and therefore SNR_{out} can be approximated as

$$SNR_{out} = \frac{\overline{\Xi}}{\sqrt{\overline{\Delta^2\Xi}}} = \frac{\overline{n}\,\overline{N}}{\sqrt{\overline{n}\,\overline{N}(\overline{n}+1)}} = \sqrt{N}\sqrt{\frac{\overline{n}}{\overline{n}+1}}\,. \tag{A.8}$$

B | Strain Theory for (S)TEM

In (S)TEM only the projected strain can be determined (at least from a single measurement), which means that not all components of the strain tensor are readily accessible. For a set of two measured linearly independent reciprocal lattice vectors $\mathbf{G}_1$ and $\mathbf{G}_2$ the distortion matrix $\underline{\mathbf{D}}$ can be calculated relative to reference vectors $\mathbf{G}_{1,ref}$ and $\mathbf{G}_{2,ref}$. The matrices $\underline{\mathbf{G}} = [\mathbf{G}_1, \mathbf{G}_2]$ and $\underline{\mathbf{G}}_{ref} = [\mathbf{G}_{1,ref}, \mathbf{G}_{2,ref}]$ are connected with $\underline{\mathbf{D}}$ as

$$\underline{\mathbf{D}} = (\underline{\mathbf{G}}^T)^{-1}\, \underline{\mathbf{G}}_{ref}^T - \mathbb{1} \ , \tag{B.1}$$

where T denotes the transpose and $\mathbb{1}$ is the identity matrix. The strain and rotation matrices $\underline{\varepsilon}$ and $\underline{\mathbf{\Omega}}$ for this two-dimensional case can be calculated from $\underline{\mathbf{D}}$ as

$$\underline{\varepsilon} = \frac{1}{2}(\underline{\mathbf{D}} + \underline{\mathbf{D}}^T) \quad , \quad \underline{\mathbf{\Omega}} = \frac{1}{2}(\underline{\mathbf{D}} - \underline{\mathbf{D}}^T) \ . \tag{B.2}$$

When assuming linear elasticity (for the case of small deformations), the three-dimensional strain tensor $\underline{\varepsilon}$ is related to the deformation $\underline{\sigma}$ via the elasticity tensor $\underline{\mathbf{C}}$ according to Hooke's law as

$$\sigma_{ij} = \sum_{kl} C_{ijkl}\varepsilon_{kl} \ , \tag{B.3}$$

where the indices i, j, k, l run over the three spatial dimension. The elasticity tensor is normally simplified by making use of symmetries and replacing pairs of indices by a single index according to:

$$\begin{array}{lll} 11 \rightarrow 1 & 12 \rightarrow 6 & 13 \rightarrow 5 \\ 21 \rightarrow 6 & 22 \rightarrow 2 & 23 \rightarrow 4 \\ 31 \rightarrow 5 & 32 \rightarrow 4 & 33 \rightarrow 3 \end{array} \tag{B.4}$$

Utilizing this simplification, Hooke's law can be written

$$\begin{pmatrix}\sigma_{11}\\ \sigma_{22}\\ \sigma_{33}\\ \sigma_{23}\\ \sigma_{13}\\ \sigma_{12}\end{pmatrix} = \begin{bmatrix}C_{11} & C_{12} & C_{13} & C_{14} & C_{15} & C_{16}\\ C_{12} & C_{22} & C_{23} & C_{24} & C_{25} & C_{26}\\ C_{13} & C_{23} & C_{33} & C_{34} & C_{35} & C_{36}\\ C_{14} & C_{24} & C_{34} & C_{44} & C_{45} & C_{46}\\ C_{15} & C_{25} & C_{35} & C_{45} & C_{55} & C_{56}\\ C_{16} & C_{26} & C_{36} & C_{46} & C_{56} & C_{66}\end{bmatrix} \begin{pmatrix}\varepsilon_{11}\\ \varepsilon_{22}\\ \varepsilon_{33}\\ 2\varepsilon_{23}\\ 2\varepsilon_{13}\\ 2\varepsilon_{12}\end{pmatrix} . \tag{B.5}$$

For cubic crystal systems, $\underline{\mathbf{C}}$ has only three independent components and the relationship simplifies to

$$\begin{pmatrix}\sigma_{11}\\ \sigma_{22}\\ \sigma_{33}\\ \sigma_{23}\\ \sigma_{13}\\ \sigma_{12}\end{pmatrix} = \begin{bmatrix}C_{11} & C_{12} & C_{12} & 0 & 0 & 0\\ C_{12} & C_{11} & C_{12} & 0 & 0 & 0\\ C_{12} & C_{12} & C_{11} & 0 & 0 & 0\\ 0 & 0 & 0 & C_{44} & 0 & 0\\ 0 & 0 & 0 & 0 & C_{44} & 0\\ 0 & 0 & 0 & 0 & 0 & C_{44}\end{bmatrix} \begin{pmatrix}\varepsilon_{11}\\ \varepsilon_{22}\\ \varepsilon_{33}\\ 2\varepsilon_{23}\\ 2\varepsilon_{13}\\ 2\varepsilon_{12}\end{pmatrix} . \tag{B.6}$$

In the case of an epitaxy in which a cubic material B with lattice parameter a_B is grown on top of a cubic substrate A with lattice parameter a_A, which are both infinitely extended in directions x and y and with a free surface perpendicular to z, the stresses can be assumed to be

$$\sigma_{zz} = \sigma_{yz} = \sigma_{xz} = \sigma_{xy} = 0 \ . \tag{B.7}$$

The first part is zero due to the free surface and the three others because no shears should exist. To simplify the discussion and obtain a useful expression for experimental strain measurements the magnitude of Lagrange strain $\underline{\varepsilon}$ and material strain $\underline{\varepsilon}'$ will be set equal later, which is a decent approximation for small strains:

$$\varepsilon_{xx}^{B} = \frac{a_A - a_B}{a_B} \approx -\varepsilon_{xx}'^{B} = -\frac{a_B - a_A}{a_A} \ . \tag{B.8}$$

With the assumptions from Eq. B.7 Hooke's law simplifies to

$$\begin{aligned}\sigma_{xx} &= C_{11}\varepsilon'_{xx} + C_{12}\varepsilon'_{yy} + C_{12}\varepsilon'_{zz}\\ \sigma_{yy} &= C_{12}\varepsilon'_{xx} + C_{11}\varepsilon'_{yy} + C_{12}\varepsilon'_{zz}\\ \sigma_{zz} &= C_{12}\varepsilon'_{xx} + C_{12}\varepsilon'_{yy} + C_{11}\varepsilon'_{zz} = 0 \ .\end{aligned} \tag{B.9}$$

(B.10)

From the third equation we can obtain a useful expression for the σ_{zz} strain component relative to an experimentally accessible substrate lattice parameter value a_A if we use the approximation of Eq. B.8:

$$\varepsilon_z^B = -\left(\frac{2C_{12}^B}{C_{11}^B} + 1\right)\frac{a_B - a_A}{a_A} \ . \tag{B.11}$$

This expression describes the biaxially strained case. When a sample is thinned for (S)TEM observation perpendicular to the epitaxy interface, strain is relieved. In the uniaxial case, when all strain in this direction is relieved, the strain in growth direction becomes

$$\varepsilon_z^B = -\left(\frac{C_{12}^B}{C_{11}^B} + 1\right)\frac{a_B - a_A}{a_A} \ . \tag{B.12}$$

The strain state of a TEM sample should normally be in between these two cases. The exact situation can be evaluated from finite element simulations using the sample thickness.

Acknowledgments

First and foremost I would like to thank Jean-Luc Rouvière. Not only because he supervised the thesis and part of it is heavily based on what he developed and achieved, but also because he provided me an enormous amount of freedom in my research. This led me away from my original topic and into a plethora of techniques and materials. He always trusted that I would be able to manage all of that and produce a good and coherent thesis in the end, for which I want to thank him sincerely.

I thank Quentin Ramasse and Andreas Rosenauer for accepting to write a report on the thesis and for being on the defense committee.

Edgar Rauch and Holger Klein is thanked for accepting to be on the defense committee.

special thanks to Jian-Min (Jim) Zuo. Spending several months in the same office with him while he stayed in Grenoble in the framework of the 'chair of excellence' program of the Nanosciences Foundation brought me in contact with TeMA and let me discuss it extensively with him, for which I am very grateful.

I want to thank David Cooper for all the great work that we performed together and the samples he prepared for me. His holography skills proved to be a great asset in the comparison of different techniques and his know-how in terms of sample preparation gave me the opportunity to perform in-situ biasing experiments while letting everything look so easy. Benjamin Bunny approves.

Special thanks to Robert McLeod for starting to develop an image registration code, that later became Zorro, and for interesting discussions on a daily basis. And of course for being a good drinking companion.

Nicolas Mollard is thanked for teaching me how to do tripod polishing and for preparing very high quality FIB lamellae for me, often for non-trivial materials (like HgTe/CdTe).

I want to thank especially Thomas Auzelle and Bruno Daudin, but also the rest of Bruno's group for a very good and efficient collaboration concerning GaN NWs.

Thanks go to Candice Thomas and Philippe Ballet for a very interesting and fruitful research cooperation concerning HgTe/CdTe.

I thank Bastien Bonef for the good collaboration concerning ZnTe/CdSe and the insight that he provided me and the discussion concerning atom probe tomography, together with Isabelle Mouton.
Thanks go to Bernier (Nicolas Bernier) for introducing me to COMSOL finite element simulations for HgTe and the collaboration concerning InGaAs QWFs.
Catherine Bougerol is thanked for the collaboration, for all the samples she provided me with and for doing the ESONN summer school practical together.
I would like to thank Joël Eymery for providing the KOH-etched GaN wires and for interesting discussions.
Frédéric Lançon is thanked for providing the DFT results concerning GaN IDB prior to publication and for the fruitful discussions.
Thanks go to Nicolas Mante for helping me with the tripod polishing and for the discussion we had concerning GaN.
Martien den Hertog is thanked for providing patterned Si_3N_4 membrane grids and for interesting discussions concerning many topics. I hope the initiated collaboration concerning piezoelectric fields in NWs continues.
I thank Vincent Delaye for tending the microscopes and for tolerating my tweaking of scanning patterns and other unusual activities.
Thanks go to Hanako Okuno for a lot of organization effort concerning LEMMA group but also my thesis in particular.
I would like to thank my office crew for a very enjoyable time. Despite the fluctuations of new people coming and others leaving it was always entertaining and never boring. Special thanks to Fabio Agnese for helping me with a lot of administrative tasks.
Thanks go to everyone from PFNC for a really good time and also to everyone that I might have forgotten to mention in particular.
And last but not least, I want to thank my family for continuous, unwavering support.

Bibliography

[1] C. A. Curcio, K. R. Sloan, R. E. Kalina, and A. E. Hendrickson, 'Human Photoreceptor Topography', *The Journal of Comparative Neurology*, **523**, 497 (1990).

[2] K. Koch, J. McLean, R. Segev, M. A. Freed, M. J. B. II, V. Balasubramanian, and P. Sterling, 'How Much the Eye Tells the Brain', *Current Biology*, **16**, 1428 (2006).

[3] E. Lifshin, *Characterization of materials*, no. 2, pt. 1 in Materials science and technology, VCH (1992).

[4] E. Ruska, *Über eine Berechnungsmethode des Kathodenstrahloszillographen auf Grund der experimentell gefundenen Abhängigkeit des Schreibfleckdurchmessers von der Stellung der Konzentrierspule.*, Student project thesis, Technische Hochschule Berlin (1929).

[5] E. Ruska, *Über ein magnetisches Objektiv für das Elektronenmikroskop.*, Ph.D. thesis, Technische Hochschule Berlin (1933).

[6] L. De Broglie, 'Recherche sur la théorie des quanta.', in: 'Annales de Physique', vol. 10, 22 (1925).

[7] E. Ruska, 'Nobel Lecture: The Development of the Electron Microscope and of Electron Microscopy', $nobelprize.org/nobel\_prizes/physics/laureates/1986/ruska-lecture.pdf$.

[8] O. Scherzer, 'Über einige Fehler von Elektronenlinsen', *Zeitschrift für Physik*, **101**, 593 (1936).

[9] D. Gabor, 'A New Microscopic Principle', *Nature*, **161**, 777 (1948).

[10] P. Batson and N. Dellby, 'Sub-angstrom resolution using aberration corrected optics', *Nature*, **418**, 270 (2002).

[11] D. Shechtman, I. Blech, D. Gratias, and J. W. Cahn, 'Metallic Phase with Long-Range Orientational Order and No Translational Symmetry', *Physical Review Letters*, **53**, 1951 (1984).

[12] R. S. Ruskin, Z. Yu, and N. Grigorieff, 'Quantitative characterization of electron detectors for transmission electron microscopy', *Journal of Structural Biology*, **184**, 385 (2013).

[13] A. Rosenauer, F. F. Krause, K. Müller, M. Schowalter, and T. Mehrtens, 'Conventional Transmission Electron Microscopy Imaging beyond the Diffraction and Information Limits', *Physical Review Letters*, **113**, 096101 (2014).

[14] S. D. Findlay, N. Shibata, H. Sawada, E. Okunishi, Y. Kondo, and Y. Ikuhara, 'Dynamics of annular bright field imaging in scanning transmission electron microscopy', *Ultramicroscopy*, **110**, 903 (2010).

[15] S. Findlay, T. Saito, N. Shibata, Y. Sato, J. Matsuda, K. Asano, E. Akiba, T. Hirayama, and Y. Ikuhara, 'Direct imaging of hydrogen within a crystalline environment', *Applied Physics Express*, **3**, 6 (2010).

[16] M. von Ardenne, 'Das Elektronen-Rastermikroskop', *Zeitschrift für Physik*, **109**, 553 (1938).

[17] A. V. Crewe, 'Scanning Electron Microscopes: Is High Resolution Possible?', *Science*, **154**, 729 (1966).

[18] A. V. Crewe, J. Wall, and J. Langmore, 'Visibility of Single Atoms', *Science*, **168**, 1338 (1970).

[19] M. Treacy, A. Howie, and S. Pennycook, 'Z-contrast of supported catalyst particles on the STEM. Electron Microscopy and Analysis 1979', in: 'Institute of Physics Confonference Series', 52, 261 (1980).

[20] S. J. Pennycook and D. E. Jesson, 'High-resolution incoherent imaging of crystals', *Physical Review Letters*, **64**, 938 (1990).

[21] P. D. Nellist, M. F. Chisholm, N. Dellby, O. L. Krivanek, M. F. Murfitt, Z. S. Szilagyi, A. R. Lupini, A. Borisevich, W. H. Sides, and S. J. Pennycook, 'Direct Sub-Angstrom Imaging of a Crystal Lattice', *Science*, **305**, 1741 (2004).

[22] D. B. Williams and C. B. Carter, *Transmission Electron Microscopy: A Textbook for Materials Science*, Springer-Verlag US (2009).

[23] L. Reimer and H. Kohl, *Transmission Electron Microscopy: Physics of Image Formation*, Springer, fifth ed. (2008).

[24] K. Müller, F. F. Krause, A. Béché, M. Schowalter, V. Galioit, S. Löffler, J. Verbeeck, J. Zweck, P. Schattschneider, and A. Rosenauer, 'Atomic electric fields revealed by a quantum mechanical approach to electron picodiffraction', *Nature Communications*, **5**, 5653 (2014).

[25] R. Vincent and P. A. Midgley, 'Double conical beam-rocking system for measurement of integrated electron diffraction intensities', *Ultramicroscopy*, **53**, 271 (1994).

[26] E. J. Kirkland, *Advanced Computing in Electron Microscopy*, Springer, second ed. (2010).

[27] A. Bleloch and Q. Ramasse, *Lens Aberrations: Diagnosis and Correction*, 55–87, in: 'Aberration–Corrected Analytical Transmission Electron Microscopy', John Wiley & Sons, Ltd (2011).

[28] S. Uhlemann and M. Haider, 'Residual wave aberrations in the first spherical aberration corrected transmission electron microscope', *Ultramicroscopy*, **72**, 109 (1998).

[29] J. Barthel, *Ultra-Precise Measurement of Optical Aberrations for Sub-Ångström Transmission Electron Microscopy*, Ph.D. thesis, Technische Hochschule Aachen (1997).

[30] M. T. Browne and J. F. L. Ward, 'Detectors for STEM, and the measurement of their detective quantum efficiency', *Ultramicroscopy*, **7**, 249 (1982).

[31] R. N. Clough, G. Moldovan, and A. I. Kirkland, 'Direct Detectors for Electron Microscopy', *Journal of Physics: Conference Series*, **522**, 012046 (2014).

[32] X. Li, P. Mooney, S. Zheng, C. R. Booth, M. B. Braunfeld, S. Gubbens, D. A. Agard, and Y. Cheng, 'Electron counting and beam-induced motion correction enable near-atomic-resolution single-particle cryo-EM.', *Nature methods*, **10**, 584 (2013).

[33] M. Linck, P. Hartel, S. Uhlemann, F. Kahl, H. Müller, J. Zach, M. Haider, M. Niestadt, M. Bischoff, J. Biskupek, Z. Lee, T. Lehnert, F. Börrnert, H. Rose, and U. Kaiser, 'Chromatic Aberration Correction for Atomic Resolution TEM Imaging from 20 to 80 kV', *Physical Review Letters*, **117**, 076101 (2016).

[34] R. Leary, Z. Saghi, P. A. Midgley, and D. J. Holland, 'Compressed sensing electron tomography', *Ultramicroscopy*, **131**, 70 (2013).

[35] M. L. Taheri, E. A. Stach, I. Arslan, P. Crozier, B. C. Kabius, T. LaGrange, A. M. Minor, S. Takeda, M. Tanase, J. B. Wagner, and R. Sharma, 'Current status and future directions for in situ transmission electron microscopy', *Ultramicroscopy*, **170**, 86 (2016).

[36] A. Rosenauer, K. Gries, K. Müller, A. Pretorius, M. Schowalter, A. Avramescu, K. Engl, and S. Lutgen, 'Measurement of specimen thickness and composition in $Al_xGa_{1-x}N$ / GaN using high-angle annular dark field images', *Ultramicroscopy*, **109**, 1171 (2009).

[37] C. Dwyer, C. Maunders, C. L. Zheng, M. Weyland, P. C. Tiemeijer, and J. Etheridge, 'Sub-0.1nm-resolution quantitative scanning transmission electron microscopy without adjustable parameters', *Applied Physics Letters*, **100**, 191915 (2012).

[38] A. Thust, 'High-resolution transmission electron microscopy on an absolute contrast scale', *Physical Review Letters*, **102**, 220801 (2009).

[39] J. M. Zuo and J. C. H. Spence, *Electron Microdiffraction*, Springer US (1992).

[40] C. J. Humphreys, 'The scattering of fast electrons by crystals', *Reports on Progress in Physics*, **42**, 1825 (1979).

[41] S. Pennycook and D. Jesson, 'High-resolution Z-contrast imaging of crystals', *Ultramicroscopy*, **37**, 14 (1991).

[42] A. Amali, P. Rez, and J. Cowley, 'High angle annular dark field imaging of stacking faults', *Micron*, **28**, 89 (1997).

[43] P. Nellist and S. Pennycook, 'Incoherent imaging using dynamically scattered coherent electrons', *Ultramicroscopy*, **78**, 111 (1999).

[44] L. Allen, S. Findlay, M. Oxley, and C. Rossouw, 'Lattice-resolution contrast from a focused coherent electron probe. Part I', *Ultramicroscopy*, **96**, 47 (2003).

[45] S. Findlay, L. Allen, M. Oxley, and C. Rossouw, 'Lattice-resolution contrast from a focused coherent electron probe. Part II', *Ultramicroscopy*, **96**, 65 (2003).

[46] P. Stadelmann, 'EMS - a software package for electron diffraction analysis and HREM image simulation in materials science', *Ultramicroscopy*, **21**, 131 (1987).

[47] J. M. LeBeau, S. D. Findlay, X. Wang, A. J. Jacobson, L. J. Allen, and S. Stemmer, 'High-angle scattering of fast electrons from crystals containing heavy elements: Simulation and experiment', *Physical Review B*, **79**, 214110 (2009).

[48] J. M. Lebeau, S. D. Findlay, L. J. Allen, and S. Stemmer, 'Position averaged convergent beam electron diffraction: theory and applications.', *Ultramicroscopy*, **110**, 118 (2010).

[49] J. M. Cowley and A. F. Moodie, 'The scattering of electrons by atoms and crystals. I. A new theoretical approach', *Acta Crystallographica*, **10**, 609 (1957).

[50] K. Ishizuka and N. Uyeda, 'A new theoretical and practical approach to the multislice method', *Acta Crystallographica Section A*, **33**, 740 (1977).

[51] D. A. Muller, B. Edwards, E. J. Kirkland, and J. Silcox, 'Simulation of thermal diffuse scattering including a detailed phonon dispersion curve', *Ultramicroscopy*, **86**, 371 (2001), international Symposium on Spectroscopy of Materials.

[52] A. Rosenauer and M. Schowalter, 'STEMSIM - A New Software Tool for Simulation of STEM HAADF Z-Contrast Imaging', 170–172 (2008).

[53] R. Fritz, *Quantitative Untersuchungen der Zusammensetzung von kubischen III/V-Verbindungshalbleitern mittels HAADF-STEM*, Ph.D. thesis, Philipps-Universität Marburg (2013).

[54] J. M. LeBeau, S. D. Findlay, L. J. Allen, and S. Stemmer, 'Quantitative Atomic Resolution Scanning Transmission Electron Microscopy', *Physical Review Letters*, **100**, 206101 (2008).

[55] D. V. Dyck and M. O. de Beeck, 'A simple intuitive theory for electron diffraction', *Ultramicroscopy*, **64**, 99 (1996).

[56] P. Geuens and D. Van Dyck, 'The S-state model: a work horse for HRTEM', *Ultramicroscopy*, **93**, 179 (2002).

[57] A. Rose, 'The sensitivity performance of the human eye on an absolute scale', *Journal of the Optical Society of America*, **38**, 196 (1948).

[58] J. C. H. Spence, *High-Resolution Electron Microscopy*, Oxford University Press, third ed. (2003).

[59] W. Moerner, 'Microscopy beyond the diffraction limit using actively controlled single molecules', *Journal of Microscopy*, **246**, 213 (2012).

[60] S. Findlay, N. Shibata, H. Sawada, E. Okunishi, Y. Kondo, and Y. Ikuhara, 'Dynamics of annular bright field imaging in scanning transmission electron microscopy', *Ultramicroscopy*, **110**, 903 (2010).

[61] R. Hovden, H. L. X., and D. A. Muller, 'Determining Resolution in an Aberration-Corrected Era: Why Your Probe is Larger Than You Thought', *Mirosc. Microanal.*, **16**, 152 (2010).

[62] J. L. Rouvière, A. Mouti, and P. Stadelmann, 'Measuring strain on HR-STEM images: application to threading dislocations in $Al_{0.8}$ $In_{0.2N}$', *Journal of Physics: Conference Series*, **326**, 012022 (2011).

[63] N. Braidy, Y. Le Bouar, S. Lazar, and C. Ricolleau, 'Correcting scanning instabilities from images of periodic structures', *Ultramicroscopy*, **118**, 67 (2012).

[64] J.-M. Zuo, A. B. Shah, H. Kim, Y. Meng, W. Gao, and J.-L. Rouviére, 'Lattice and strain analysis of atomic resolution Z-contrast images based on template matching.', *Ultramicroscopy*, **136**, 50 (2014).

[65] A. B. Yankovich, B. Berkels, W. Dahmen, P. Binev, S. I. Sanchez, S. A. Bradley, A. Li, I. Szlufarska, and P. M. Voyles, 'Picometre-precision analysis of scanning transmission electron microscopy images of platinum nanocatalysts', *Nature Communications*, **5**, 1 (2014).

[66] L. Jones, H. Yang, T. J. Pennycook, M. S. J. Marshall, S. Van Aert, N. D. Browning, M. R. Castell, and P. D. Nellist, 'Smart Align—a new tool for robust non-rigid registration of scanning microscope data', *Advanced Structural and Chemical Imaging*, **1**, 8 (2015).

[67] X. Sang and J. M. LeBeau, 'Revolving scanning transmission electron microscopy: Correcting sample drift distortion without prior knowledge', *Ultramicroscopy*, **138**, 28 (2014).

[68] R. A. McLeod, B. Haas, and H. Stahlberg, 'Zorro: multi-reference dose-fractionated image registration', in: 'European Microscopy Congress 2016: Proceedings', Wiley-VCH.

[69] R. A. McLeod, J. Kowal, P. Ringler, and H. Stahlberg, 'Robust image alignment for cryogenic transmission electron microscopy', *Journal of Structural Biology*, **197**, 279 (2017).

[70] D. Padfield, 'Masked Object Registration in the Fourier Domain', *IEEE Transactions on Image Processing*, **21**, 2706 (2012).

[71] D. J. Wales and J. P. K. Doye, 'Global Optimization by Basin-Hopping and the Lowest Energy Structures of Lennard-Jones Clusters Containing up to 110 Atoms', *The Journal of Physical Chemistry A*, **101**, 5111 (1997).

[72] J. Verbeeck, A. Béché, and W. Van den Broek, 'A holographic method to measure the source size broadening in STEM.', *Ultramicroscopy*, **120**, 35 (2012).

[73] D. Su and Y. Zhu, 'Scanning moiré fringe imaging by scanning transmission electron microscopy', *Ultramicroscopy*, **110**, 229 (2010).

[74] S. Kim, Y. Kondo, K. K. Lee, G. Byun, J. Jung Kim, S. Lee, and K. K. Lee, 'Quantitative measurement of strain field in strained-channel-transistor arrays by scanning moiré fringe imaging', *Applied Physics Letters*, **103**, 033523 (2013).

[75] S. Kim, S. Lee, Y. Kondo, K. Lee, G. Byun, S. Lee, and K. Lee, 'Strained hetero interfaces in Si/SiGe/SiGe/SiGe multi-layers studied by scanning moiré fringe imaging', *Journal of Applied Physics*, **114** (2013).

[76] S. Kim, S. Lee, Y. Oshima, Y. Kondo, E. Okunishi, N. Endo, J. Jung, G. Byun, S. Lee, and K. Lee, 'Scanning moiré fringe imaging for quantitative strain mapping in semiconductor devices', *Applied Physics Letters*, **102** (2013).

[77] M. Hytch, C. Gatel, A. Ishizuka, and K. Ishizuka, 'Mapping 2D strain components from STEM moiré fringes', in: 'European Microscopy Congress 2016: Proceedings', Wiley-VCH.

[78] M. Takeda and J. Suzuki, 'Crystallographic heterodyne phase detection for highly sensitive lattice-distortion measurements', *J. Opt. Soc. Am. A*, **13**, 1495 (1996).

[79] M. Hÿtch, E. Snoeck, and R. Kilaas, 'Quantitative measurement of displacement and strain fields from HREM micrographs', *Ultramicroscopy*, **74**, 131 (1998).

[80] J. Rouvière and E. Sarigiannidou, 'Theoretical discussions on the geometrical phase analysis', *Ultramicroscopy*, **106**, 1 (2005).

[81] J. J. P. Peters, R. Beanland, M. Alexe, J. W. Cockburn, D. G. Revin, S. Y. Zhang, and A. M. Sanchez, 'Artefacts in geometric phase analysis of compound materials', *Ultramicroscopy*, **157**, 9 (2015).

[82] E. F. Rauch and M. Véron, 'Automated crystal orientation and phase mapping in TEM', *Materials Characterization*, **98**, 1 (2014).

[83] B. Haas, K. I. Gries, T. Breuer, I. Haäusler, G. Witte, and K. Volz, 'Microstructural Characterization of Organic Heterostructures by (Transmission) Electron Microscopy', *Crystal Growth & Design*, **14**, 3010 (2014).

[84] K. Usuda, T. Numata, T. Irisawa, N. Hirashita, and S. Takagi, 'Strain characterization in SOI and strained-Si on SGOI MOSFET channel using nano-beam electron diffraction (NBD)', *Materials Science and Engineering B: Solid-State Materials for Advanced Technology*, **124-125**, 143 (2005).

[85] D. Cooper, N. Bernier, and J.-L. Rouvière, 'Combining 2 nm Spatial Resolution and 0.02% Precision for Deformation Mapping of Semiconductor Specimens in a Transmission Electron Microscope by Precession Electron Diffraction', *Nano Letters*, **15**, 5289 (2015).

[86] A. Béché, J. L. Rouvière, L. Clément, and J. M. Hartmann, 'Improved precision in strain measurement using nanobeam electron diffraction', *Applied Physics Letters*, **95**, 123114 (2009).

[87] J. M. LeBeau and S. Stemmer, 'Experimental quantification of annular dark-field images in scanning transmission electron microscopy', *Ultramicroscopy*, **108**, 1653 (2008).

[88] J. M. Lebeau, S. D. Findlay, L. J. Allen, and S. Stemmer, 'Quantitative atomic resolution scanning transmission electron microscopy', *Physical Review Letters*, **100**, 1 (2008).

[89] F. F. Krause, M. Schowalter, T. Grieb, K. Müller-Caspary, T. Mehrtens, and A. Rosenauer, 'Effects of instrument imperfections on quantitative scanning transmission electron microscopy', *Ultramicroscopy*, **161**, 146 (2016).

[90] T. Grieb, K. Müller, R. Fritz, M. Schowalter, N. Neugebohrn, N. Knaub, K. Volz, and A. Rosenauer, 'Determination of the chemical composition of GaNAs using STEM HAADF imaging and STEM strain state analysis', *Ultramicroscopy*, **117**, 15 (2012).

[91] H. Rose, 'Phase Contrast in Scanning Transmission Electron Microscopy', *Optik*, **39**, 416 (1974).

[92] E. Okunishi, I. Ishikawa, H. Sawada, F. Hosokawa, M. Hori, and Y. Kondo, 'Visualization of light elements at ultrahigh resolution by STEM annular bright field microscopy', *Microscopy and Microanalysis*, **15**, 164 (2009).

[93] S. D. Findlay, N. Shibata, H. Sawada, E. Okunishi, Y. Kondo, T. Yamamoto, and Y. Ikuhara, 'Robust atomic resolution imaging of light elements using scanning transmission electron microscopy', *Applied Physics Letters*, **95**, 10 (2009).

[94] R. Ishikawa, E. Okunishi, H. Sawada, Y. Kondo, F. Hosokawa, and E. Abe, 'Direct imaging of hydrogen-atom columns in a crystal by annular bright-field electron microscopy.', *Nature materials*, **10**, 278 (2011).

[95] M. Winter, J. O. Besenhard, M. E. Spahr, and P. Novák, 'Insertion electrode materials for rechargeable lithium batteries', *Advanced materials*, **10**, 725 (1998).

[96] J.-M. Tarascon and M. Armand, 'Issues and challenges facing rechargeable lithium batteries', *Nature*, **414**, 359 (2001).

[97] A. D. Robertson and P. G. Bruce, 'Mechanism of Electrochemical Activity in Li 2 MnO 3', *Chemistry of Materials*, **15**, 1984 (2003).

[98] D. Pasero, V. McLaren, S. de Souza, and a. R. West, 'Oxygen Nonstoichiometry in Li 2 MnO 3 : An Alternative Explanation for Its Anomalous Electrochemical Activity', *Chemistry of Materials*, **17**, 345 (2005).

[99] A. Boulineau, L. Croguennec, C. Delmas, and F. Weill, 'Reinvestigation of Li2MnO3 structure: electron diffraction and high resolution TEM', *Chemistry of Materials*, **21**, 4216 (2009).

[100] K. A. Jarvis, Z. Deng, L. F. Allard, A. Manthiram, and P. J. Ferreira, 'Understanding structural defects in lithium-rich layered oxide cathodes', *Journal of Materials Chemistry*, **22**, 11550 (2012).

[101] H. Lichte, P. Formanek, A. Lenk, M. Linck, C. Matzeck, M. Lehmann, and P. Simon, 'Electron holography: Applications to materials questions', *Annual Review of Materials Research*, **37**, 539 (2007).

[102] M. R. McCartney and D. J. Smith, 'Electron holography: Phase imaging with nanometer resolution', *Annual Review of Materials Research*, **37**, 729 (2007).

[103] C. Phatak, A. K. Petford-Long, and M. De Graef, 'Three-dimensional study of the vector potential of magnetic structures', *Physical Review Letters*, **104**, 1 (2010).

[104] N. H. Dekkers and H. de Lang, 'Differential Phase Contrast in a STEM', *Optik*, **41**, 452 (1974).

[105] M. Lohr, R. Schregle, M. Jetter, W. Clemens, T. Wunderer, F. Scholz, and J. Zweck, 'Differential phase contrast 2.0 - Opening new ' fields ' for an established technique', *Ultramicroscopy*, **117**, 7 (2012).

[106] N. Shibata, S. D. Findlay, Y. Kohno, H. Sawada, Y. Kondo, and Y. Ikuhara, 'Differential phase-contrast microscopy at atomic resolution', *Nature Physics*, **8**, 611 (2012).

[107] N. Shibata, S. D. Findlay, H. Sasaki, T. Matsumoto, H. Sawada, Y. Kohno, S. Otomo, R. Minato, and Y. Ikuhara, 'Imaging of built-in electric field at a p-n junction by scanning transmission electron microscopy', *Scientific Reports*, **5**, 1 (2015).

[108] M. Lohr, R. Schregle, M. Jetter, C. Wächter, K. Müller-Caspary, T. Mehrtens, A. Rosenauer, I. Pietzonka, M. Strassburg, and J. Zweck, 'Quantitative measurements of internal electric fields with differential phase contrast microscopy on InGaN/GaN quantum well structures', *Physica Status Solidi B*, **253**, 140 (2016).

[109] T. Grieb, F. F. Krause, C. Mahr, K. Müller-Caspary, D. Zillmann, M. Schowalter, and A. Rosenauer, 'Optimization of NBED simulations to accurately predict disc-detection measurements', in: 'European Microscopy Congress 2016: Proceedings', Wiley-VCH.

[110] D. Cooper, P. Rivallin, G. Guegan, C. Plantier, E. Robin, F. Guyot, and I. Constant, 'Field mapping of focused ion beam prepared semiconductor devices by off-axis and dark field electron holography', *Semiconductor Science and Technology*, **28**, 125013 (2013).

[111] K. Song, C. T. Koch, J. K. Lee, D. Y. Kim, J. K. Kim, A. Parvizi, W. Y. Jung, C. G. Park, H. J. Jeong, H. S. Kim, Y. Cao, T. Yang, L. Q. Chen, and S. H. Oh, 'Correlative High-Resolution Mapping of Strain and Charge Density in a Strained Piezoelectric Multilayer', *Advanced Materials Interfaces*, **2**, 1 (2015).

[112] B. Bauer, *Transmission Electron Microscopy on GaAs Nanowires - Spontaneous Polarization and MnAs Nanocrystals*, Ph.D. thesis, Universität Regensburg (2015).

[113] K. X. Nguyen, R. Hovden, M. W. Tate, P. Purohit, J. Heron, C. Chang, S. M. Gruner, and D. A. Muller, 'Lorentz-STEM imaging of Fields and Domains using

a High-Speed, High-Dynamic Range Pixel Array Detector at Atomic Resolution', *Microscopy and Microanalysis*, **21**, 2309 (2015).

[114] B. Haas, D. Cooper, and J.-L. Rouvière, 'Méthode de détermination de la réflexion d'un faisceau d'électrons resultant d'un champ électrique et/ou d'un champ magnétique', Patent pending (filed 14/09/2016).

[115] B. Bonef, B. Haas, J. L. Rouvière, R. André, C. Bougerol, A. Grenier, P. H. Jouneau, and J. M. Zuo, 'Interfacial chemistry in a ZnTe/CdSe superlattice studied by atom probe tomography and transmission electron microscopy strain measurements', *Journal of Microscopy*, **262**, 178 (2016).

[116] D. Mourad, J.-P. Richters, L. Gérard, R. André, J. Bleuse, and H. Mariette, 'Determination of valence-band offset at cubic CdSe/ZnTe type-II heterojunctions: A combined experimental and theoretical approach', *Physical Review B*, **86**, 195308 (2012).

[117] S. Boyer-Richard, C. Robert, L. Gérard, J.-P. Richters, R. André, J. Bleuse, H. Mariette, J. Even, and J.-M. Jancu, 'Atomistic simulations of the optical absorption of type-II CdSe/ZnTe superlattices', *Nanoscale Research Letters*, **7**, 543 (2012).

[118] B. Bonef, L. Gérard, J. Rouvière, A. Grenier, P. Jouneau, E. Bellet-Almaric, H. Mariette, R. André, and C. Bougerol, 'Atomic arrangement at ZnTe/CdSe interfaces determined by high resolution scanning transmission electron microscopy and atom probe tomography', *Applied Physics Letters*, **106**, 051904 (2015).

[119] H. J. McSkimin and D. G. Thomas, 'Elastic moduli of cadmium telluride', *Journal of Applied Physics*, **33**, 56 (1962).

[120] B. H. Lee, 'Elastic Constants of ZnTe and ZnSe between 77 - 300 K', *Journal of Applied Physics*, **41**, 2984 (1970).

[121] E. Deligoz, K. Colakoglu, and Y. Ciftci, 'Elastic, electronic, and lattice dynamical properties of CdS, CdSe, and CdTe', *Physica B: Condensed Matter*, **373**, 124 (2006).

[122] A. Béché, *Mesure de déformation à l'échelle nanométrique par microscopie électronique en transmission*, Ph.D. thesis, Université de Grenoble (2009).

[123] C. Thomas, *Strained HgTe/CdTe topological insulators, toward spintronic applications*, Ph.D. thesis, Univ. Grenoble Alpes (2016).

[124] L. Fu, C. Kane, and E. Mele, 'Topological Insulators in Three Dimensions', *Physical Review Letters*, **98**, 106803 (2007).

[125] D. Hsieh, Y. Xia, D. Qian, H. Wray, L. andDil, F. Meier, J. Osterwalder, L. Patthey, J. Checkelsky, N. Ong, H. Fedorov, A.V.and Lin, A. Bansil, D. Grauer, Y. Hor, R. Cava, and M. Hasan, 'A tunable topological insulator in the spin helical Dirac transport regime', *Nature*, **460**, 1101 (2009).

[126] The Royal Swedish Academy of Sciences, 'Press Release: The Nobel Prize in Physics 2016', $www.nobelprize.org/nobel_prizes/physics/laureates/2016/press.html$.

[127] D. A. Kozlov, Z. D. Kvon, E. B. Olshanetsky, N. N. Mikhailov, S. A. Dvoretsky, and D. Weiss, 'Transport Properties of a 3D Topological Insulator based on a Strained High-Mobility HgTe Film', *Physical Review Letters*, **112**, 196801 (2014).

[128] C. Brüne, C. X. Liu, E. G. Novik, E. M. Hankiewicz, H. Buhmann, Y. L. Chen, X. L. Qi, Z. X. Shen, S. C. Zhang, and L. W. Molenkamp, 'Quantum Hall Effect from the Topological Surface States of Strained Bulk HgTe', *Physical Review Letters*, **106**, 126803 (2011).

[129] S. Zhang, H. Lu, and S. Shen, 'Edge states and integer quantum Hall effect in topological insulatorthin films', *Scientific Reports*, **5**, 13277 (2015).

[130] R. Cottam and G. Saunders, 'The elastic behavior of mercury telluride', *J. Phys. Chem. Solids,*, **36**, 187 (1975).

[131] R. Greenough and S. Palmer, 'The elastic constants and thermal expansion of single-crystal CdTe', *J. Phys. D: Appl. Phys.*, **6**, 587 (1973).

[132] G. Hansen, J. Schmit, and T. Casselman, 'Energy gap versus alloy composition and temperature in $Hg_{1-x}Cd_xTe$', *J. Appl. Phys.*, **53**, 7099 (1982).

[133] T. Li, E. Hahn, D. Gerthsen, A. Rosenauer, A. Strittmatter, L. Reissmann, and D. Bimberg, 'Indium redistribution in an InGaN quantum well induced by electron-beam irradiation in a transmission electron microscope', *Applied Physics Letters*, **86**, 241911 (2005).

[134] M. Schowalter, a. Rosenauer, J. T. Titantah, and D. Lamoen, 'Temperature-dependent Debye-Waller factors for semiconductors with the wurtzite-type structure', *Acta Crystallographica Section A: Foundations of Crystallography*, **65**, 227 (2009).

[135] V. Grillo, E. Carlino, and F. Glas, 'Influence of the static atomic displacement on atomic resolution Z-contrast imaging', *Physical Review B - Condensed Matter and Materials Physics*, **77**, 1 (2008).

[136] T. Mehrtens, K. Müller, M. Schowalter, D. Hu, D. M. Schaadt, and A. Rosenauer, 'Measurement of indium concentration profiles and segregation efficiencies from high-angle annular dark field-scanning transmission electron microscopy images', *Ultramicroscopy*, **131**, 1 (2013).

[137] M. A. Steiner, L. Bhusal, J. F. Geisz, A. G. Norman, M. J. Romero, W. J. Olavarria, Y. Zhang, and A. Mascarenhas, 'CuPt ordering in high bandgap $Ga_xIn_{1-x}P$ alloys on relaxed GaAsP step grades', *Journal of Applied Physics*, **106**, 063525 (2009).

[138] S.-H. Wei and A. Zunger, 'Fingerprints of CuPt ordering in III-V semiconductor alloys: Valence-band splittings, band-gap reduction, and x-ray structure factors', *Physical Review B*, **57**, 8983 (1998).

[139] C. B. Lim, A. Ajay, C. Bougerol, B. Haas, J. Schörmann, M. Beeler, J. Lähnemann, M. Eickhoff, and E. Monroy, 'Nonpolar m-plane GaN/AlGaN heterostructures with intersubband transitions in the 5-10 THz band', *Nanotechnology*, **26**, 435201 (2015).

[140] X. Zhang, H. Lourenço-Martins, S. Meuret, M. Kociak, B. Haas, J.-L. Rouvière, P.-H. Jouneau, C. Bougerol, T. Auzelle, D. Jalabert, X. Biquard, B. Gayral, and B. Daudin, 'InGaN nanowires with high InN molar fraction: growth, structural and optical properties', *Nanotechnology*, **27**, 195704 (2016).

[141] S. Y. Woo, M. Bugnet, H. P. T. Nguyen, Z. Mi, and G. A. Botton, 'Atomic Ordering in InGaN Alloys within Nanowire Heterostructures', *Nano Letters*, **15**, 6413 (2015).

[142] T. Auzelle, B. Haas, M. Den Hertog, J.-l. Rouvière, B. Daudin, and B. Gayral, 'Attribution of the 3.45 eV GaN nanowires luminescence to inversion domain boundaries', *Applied Physics Letters*, **107**, 051904 (2015).

[143] T. Auzelle, B. Haas, A. Minj, C. Bougerol, J.-L. Rouvière, A. Cros, J. Colchero, and B. Daudin, 'The influence of AlN buffer over the polarity and the nucleation of self-organized GaN nanowires', *Journal of Applied Physics*, **117**, 245303 (2015).

[144] X. Zhang, B. Haas, J.-L. Rouvière, E. Robin, and B. Daudin, 'Growth mechanism of InGaN nano-umbrellas', *Nanotechnology*, **27**, 455603 (2016).

[145] B. Haas, R. A. McLeod, T. Auzelle, B. Daudin, J. Eymery, F. Lançon, J.-M. Zuo, and J.-L. Rouvière, 'Picometre-precision atomic structure of inversion domain boundaries in GaN', in: 'European Microscopy Congress 2016: Proceedings', Wiley-VCH.

[146] E. Ertekin, P. A. Greaney, D. Chrzan, and T. D. Sands, 'Equilibrium limits of coherency in strained nanowire heterostructures', *Journal of Applied Physics*, **97**, 114325 (2005).

[147] F. Glas, 'Critical dimensions for the plastic relaxation of strained axial heterostructures in free-standing nanowires', *Physical Review B*, **74**, 121302 (2006).

[148] L. Largeau, E. Galopin, N. Gogneau, L. Travers, F. Glas, and J.-C. Harmand, 'N-Polar GaN Nanowires Seeded by Al Droplets on Si(111)', *Crystal Growth & Design*, **12**, 2724 (2012).

[149] M. D. Brubaker, I. Levin, A. V. Davydov, D. M. Rourke, N. A. Sanford, V. M. Bright, and K. A. Bertness, 'Effect of AlN buffer layer properties on the morphology and polarity of GaN nanowires grown by molecular beam epitaxy', *Journal of Applied Physics*, **110**, 053506 (2011).

[150] X. Kong, J. Ristić, M. A. Sanchez-Garcia, E. Calleja, and A. Trampert, 'Polarity determination by electron energy-loss spectroscopy: application to ultra-small III-nitride semiconductor nanocolumns', *Nanotechnology*, **22**, 415701 (2011).

[151] B. Alloing, S. Vézian, O. Tottereau, P. Vennéguès, E. Beraudo, and J. Zuniga-Pérez, 'On the polarity of GaN micro- and nanowires epitaxially grown on sapphire (0001) and Si(111) substrates by metal organic vapor phase epitaxy and ammonia-molecular beam epitaxy', *Applied Physics Letters*, **98**, 011914 (2011).

[152] J. E. Northrup, J. Neugebauer, and L. Romano, 'Inversion domain and stacking mismatch boundaries in GaN', *Physical Review Letters*, **77**, 103 (1996).

[153] S. Labat, M.-I. Richard, M. Dupraz, M. Gailhanou, G. Beutier, M. Verdier, F. Mastropietro, T. W. Cornelius, T. U. Schülli, J. Eymery, et al., 'Inversion Domain Boundaries in GaN Wires Revealed by Coherent Bragg Imaging', *ACS nano*, **9**, 9210 (2015).

[154] F. Lançon, L. Genovese, and J. Eymery, 'Revisiting inversion domain boundaries in GaN at the picometer scale', *in preparation*.

[155] L. Mandel, 'Image fluctuations in cascade intensifiers', *British Journal of Applied Physics*, **10**, 233 (1959).

List of Figures

List of Tables

Scientific Output

Journal Articles

1) B. Bonef, B. Haas, J. L. Rouvière, R. André, C. Bougerol, Ad. Grenier, P. H. Jouneau, and J. M. Zuo, 'Interfacial chemistry in a ZnTe/CdSe superlattice studied by atom probe tomography and transmission electron microscopy strain measurements', *Journal of Microscopy*, **262**, 178 (2016).

2) T. Auzelle, B. Haas, A. Minj, C. Bougerol, J. L. Rouvière, A. Cros, J. Colchero, and B. Daudin, 'The influence of AlN buffer over the polarity and the nucleation of self-organized GaN nanowires', *Journal of Applied Physics*, **117**, 245303 (2015).

3) T. Auzelle, B. Haas, M. Den Hertog, J. L. Rouvière, B. Daudin, and B. Gayral, 'Attribution of the 3.45 eV GaN nanowires luminescence to inversion domain boundaries', *Applied Physics Letters*, **107**, 051904 (2015).

4) X. Zhang, H. Lourenço-Martins, S. Meuret, M. Kociak, B. Haas, J. L. Rouvière, P. H. Jouneau, C. Bougerol, T. Auzelle, D. Jalabert, X. Biquard, B. Gayral, and B. Daudin, 'InGaN nanowires with high InN molar fraction: growth, structural and optical properties', *Nanotechnology*, **27**, 195704 (2016).

5) X. Zhang, B. Haas, J. L. Rouvière, E. Robin, and B. Daudin, 'Growth mechanism of InGaN nano-umbrellas', *Nanotechnology*, **27**, 455603 (2016).

6) C. B. Lim, A. Ajay, C. Bougerol, B. Haas, J. Schörmann, M. Beeler, J. Lähnemann, M. Eickhoff, E. Monroy, 'Nonpolar m-plane GaN/AlGaN heterostructures with intersubband transitions in the 5-10 THz band', *Nanotechnology*, **26**, 435201 (2015).

7) B. Bonef, M. Lopez-Haro, L. Amichi, M. Beeler, A. Grenier, E. Robin, P. H. Jouneau, N. Mollard, I. Mouton, B. Haas, E. Monroy and C. Bougerol, 'Composition Analysis of III-Nitrides at the Nanometer Scale: Comparison of Energy Dispersive X-ray Spectroscopy and Atom Probe Tomography', *Nanoscale Research Letters*, **11**, 461 (2016).

8) C. Thomas, O. Crauste, B. Haas, P. H. Jouneau, C. Bäuerle, L. P. Lévy, E. Orignac, D. Carpentier, P. Ballet, and T. Meunier, 'Revealing topological Dirac fermions at the

surface of strained HgTe via Quantum Hall transport spectroscopy', **submitted**

9) B. Haas, C. Thomas, P. H. Jouneau, N. Bernier, T. Meunier, P. Ballet, and J. L. Rouvière, 'High Precision Strain Mapping of Topological Insulator HgTe/HgCdTe', **submitted**

10) B. Haas and J. L. Rouvière, 'Strain mapping from two-dimensional scanning moiré patterns in [110] zone axis', **in preparation**

11) B. Haas, D. Cooper, and J. L. Rouvière, 'Direct comparison of differential phase contrast and off-axis electron holography', **in preparation**

12) B. Haas, D. Cooper, B. Daudin, and J. L. Rouvière, 'Simultaneous electric field and strain measurements of a-plane AlN/GaN', **in preparation**

Journal Covers

Patents

1) B. Haas, D. Cooper, and J. L. Rouvière, 'Méthode de détermination de la réflexion d'un faisceau d'électrons resultant d'un champ électrique et/ou d'un champ magnétique', **patent pending**, filed 14/09/2016

2) J. L. Rouvière, B. Haas, and N. Bernier, **in preparation**

Conference Talks

1) B. Haas, D. Cooper, and J. L. Rouvière, 'Direct comparison of differential phase contrast and off-axis electron holography for the measurement of electric potentials by the examination of reverse biased Si p-n junctions and III-V samples', *European Microscopy Congress 2016*, Lyon

2) B. Haas, R. A. McLeod, T. Auzelle, B. Daudin, J. Eymery, F. Lançon, J. M. Zuo, and J. L. Rouvière 'Picometre-precision atomic structure of inversion domain boundaries in GaN', *European Microscopy Congress 2016*, Lyon

3) B. Haas, T. Auzelle, X. Zhang, M. Den Hertog, B. Daudin, and J. L. Rouvière, 'Characterization of Core-Shell Inversion Domain Boundaries in Gallium Nitride Nanowires', *Microscopy of Semiconducting Materials 2015*, Cambridge

Summary

In this work, different scanning transmission electron microscopy (STEM) techniques have been developed and applied to several material systems. The creation of novel materials and devices has been a backbone of society's development and characterization methods are needed to investigate these materials in order to understand and improve them. With the advent of nanotechnology, electron microscopy has become an invaluable tool, as it is able to visualize the atomic structure of thin samples and produces a plethora of quantifiable signals.
In a first part, the numerous developments realized in this thesis are presented. Several STEM based techniques have been improved: scanning moiré fringes (SMF), nano-beam precession diffraction (NPED) and high-resolution STEM (HR-STEM). These developments allow for more accurate strain measurements, the quantitative mapping of electric fields and to realize accurate chemical profiles.
In a second part, the developed methods are applied to different material systems and compared to more classical techniques, like holography and differential phase contrast (DPC). In a II/VI solar cell structure the interface chemistry is determined from strain with atomic resolution. Very faint strain gradients that are vital for the topological insulator properties of HgTe are measured. Accurate two-dimensional strain maps are obtained of a SiGe transistor. Simultaneous strain and electric field maps of a-plane AlN/GaN reveal the influence of dislocations in the material. Core-shell type inversion domains are described for the first time in GaN nanowires. They were found in many samples grown by molecular beam epitaxy. Thanks to quantitative analysis the exact atomic structure of inversion domains in GaN is described and compared to simulations.

Résumé

Dans cette thèse, différentes techniques de microscopie électronique à transmission et à balayage (STEM : scanning transmission electron microscopy) ont été améliorées et appliquées à plusieurs structures essentiellement à base de semiconducteurs. La création de nouveaux matériaux et dispositifs a été à l'origine du développement des civilisations et des méthodes de caractérisation expérimentales sont nécessaires pour étudier les nouvelles structures afin de les comprendre et de les améliorer. Avec le développement des nanotechnologies, la microscopie électronique est devenu un outil indispensable du fait de sa grande résolution spatiale et de la pléthore d'information qu'elle permet d'obtenir.
Dans la premiére partie de cette thèse, les nombreux développements réalisés sont présentés. Plusieurs sous-techniques du STEM ont été améliorés : création de moirés obtenus par balayage (SMF : scanning moiré fringes), nano-diffraction électronique en mode précession (NPED : nano-beam precession diffraction) et haute résolution en STEM (HR-STEM). Ces développements permettent d'obtenir des cartographies quantitatives sur les déformations et les champs électriques et indirectement des informations chimiques.
Dans la deuxième partie, les techniques développés sont utilisés pour étudier différentes structures et les résultats sont comparés à ceux d'autres techniques comme l'holographie et le contraste de phase différentielle (DPC : differentail phase contrast). Dans une structure photovoltaïque à base de matériaux II-VI, une accumulation d'un matériau II a été détectée aux interfaces grâce aux mesures des déformations. Des champs de déformations tràs faibles capitaux pour le fonctionnement des isolants topologiques à base de HgTe ont été mesurés. Des cartographies de déformation très précises ont été obtenues dans des transistors SiGe. Dans des couches AlN/GaN des cartographies de déformation et de champs électriques ont pu être réalisés simultanément révélant l'importance des dislocations. Des domaines d'inversion coeur-coquille ont été mis en évidence pour la première fois. Ils ont été observés dans de nombreux fils de GaN élaborés par épitaxie par jet moléculaires. Les positions des atomes dans un domaine d'inversion ont pu être mesurés à quelques picomètres près et comparés à des calculs ab-initio.